A HIGH-RESOLUTION NUMERICAL MODEL INVESTIGATION INTO THE RESPONSE OF A CHANNELIZED SALT MARSH TO A STORM SURGE EVENT

BY

RYAN MIERAS, JAMES T. KIRBY AND FENGYAN SHI

RESEARCH REPORT NO. CACR-14-07
SPRING 2014

CENTER FOR APPLIED COASTAL RESEARCH

Ocean Engineering Laboratory
University of Delaware
Newark, Delaware 19716

ACKNOWLEDGMENT

This study was supported by NOAA Sea Grant Award No. NA10OAR4172284-12.

TABLE OF CONTENTS

LIST OF TABLES . . . . . **vi**
LIST OF FIGURES . . . . . **vii**
ABSTRACT . . . . . **xv**

Chapter

1 INTRODUCTION **1**

1.1 Motivation 3

2 FIELD STUDY **6**

2.1 Introduction 6
2.2 Description of Marsh 6
2.3 Site Selection 10
2.4 Field Methods 13

2.4.1 Measuring Pressure and Tidal Currents 13
2.4.2 Bathymetric Surveys 15

2.5 Data Analysis and Discussion 18

2.5.1 Lack of Vertical Control 20
2.5.2 Pressure and Velocities 22
2.5.3 Computing Discharge 25

3 NUMERICAL MODEL NEARCOM **31**

3.1 Background 31
3.2 Governing Equations of SHORECIRC 32
3.3 Specification of Boundary and Initial Conditions 37
3.4 Important SHORECIRC Parameters 38
3.5 Computational Environment 39

4 MODEL VALIDATION FOR A DELAWARE BAY SALT MARSH 41

4.1 Introduction . . . 41
4.2 Small Model Domain . . . 41

4.2.1 Creating the Model Grid . . . 41
4.2.2 Model Setup . . . 48
4.2.3 Results and Discussion . . . 52

4.3 Large Model Domain . . . 57

4.3.1 Model Setup . . . 58
4.3.2 Results and Discussion . . . 62

5 MODELING IDEALIZED MARSHES WITH DIFFERING TOPOGRAPHIES . . . 67

5.1 Introduction . . . 67
5.2 Scaling the Problem . . . 68
5.3 Introduction to Nonlinear Diffusion of Tidal Propagation . . . 69
5.4 Model Setup . . . 73
5.5 Results and Discussion . . . 78

5.5.1 Type A Marshes . . . 79
5.5.2 Type B Marshes . . . 83
5.5.3 Type C Marshes . . . 86
5.5.4 Type D Marshes . . . 89
5.5.5 Type D Marsh with Field Data as Boundary Condition . . . 92

5.6 Concluding Remarks . . . 93

6 CONCLUSIONS AND FUTURE WORK . . . 96

REFERENCES . . . 100

Appendix

MODEL COMPARISONS WITH EXACT SOLUTIONS TO THE NONLINEAR SHALLOW WATER WAVE EQUATIONS . . . 105

LIST OF TABLES

2.1 Total along-channel distance from Site A to each of the sites in the Brockonbridge Gut, as well as the representative percentage of the total distance. Along-channel in this case is defined as the total distance along the channel's centerline. 15

5.1 Descriptions of the configurations of the tidal flats in the four types of idealized marshes that were considered in the simulations. 73

5.2 Comprehensive description of simulation parameters for idealized marsh domains. The first letter in the Run ID denotes the marsh platform configuration type, as defined in Table 5.1. Variable definitions can be found in Figure 5.8. 78

5.3 Summary of $||k_0||L$ values for select runs. 78

LIST OF FIGURES

1.1 Potential risk for wetland loss in the Mid-Atlantic region due to different rates of Sea Level Rise (*Adopted from Titus et al., 2008*) . 4

1.2 Total Polychlorinated Biphenyls (PCBs) in select Delaware Bay marshes. Each panel represents a different marsh, labeled with acronyms at the bottom, from the lower to upper Delaware Bay moving left to right. The gray bar across the panels marks the time period when use of PCBs was banned. (*Adopted from Velinsky et al., 2011*) 5

2.1 Map of the geomorphic settings of coastal areas along Delaware Bay (*Adopted from Titus et al., 2008*) 7

2.2 Satellite image of Brockonbridge Marsh showing its location in Kent County and that it covers an area 5-10 km^2, with Delaware Bay in the upper right corner (*Imagery courtesy of Google Earth*) 8

2.3 Satellite image showing an example of the artificial, man-made ditches, called "mosquito ditches," in the upper Brockonbridge Marsh (*Imagery courtesy of Google Earth*) 9

2.4 (a) An example of *Spartina alterniflora* in Brockonbridge Marsh; (b) An example of *Spartina patens* present in higher elevations of the marsh, which are inundated less frequently. 10

2.5 Aerial photograph of Brockonbridge Marsh, taken from an airplane flying over Delaware Bay, along the coast of Delaware, after Hurricane Sandy in 2012 (*Photo courtesy of Art Trembanis, University of Delaware, Geology 2012*) 11

2.6 Layout of instrument locations in Brockonbridge Marsh. The black dot near the upper left corner marks the location of a USGS tidal and discharge gauge station, at the mouth of the Murderkill River. The location labeled Site G is the aforementioned small bridge in the discussion of site selection. (*Satellite imagery is from ESRI.*) 14

2.7 The extent of Brockonbridge Gut which was covered during each survey: (blue dots) survey conducted on July 26^{th}, 2013; (white dots) survey conducted on August 24^{th}, 2013. (*Satellite imagery is from ESRI.*) 16

2.8 Interpolated bathymetry of Brockonbridge Gut and its navigable branches, computed with the kriging technique. (a) The entire Brockonbridge Marsh up to the bridge; (b) Enlargement of domain near the mouth. The grid spacing is 1 meter. The maximum search radius was 3 meters, with a maximum of 10 nearest points used during interpolation. *Note: the satellite image was taken prior to the dates during which the bathymetric surveys were conducted, at which time the sand bank near the mouth was further north; however, the satellite imagery serves as a good frame of reference, and is thus included.* (*Satellite imagery is from ESRI.*) 17

2.9 Interpolated depth surface from bathymetric surveys, zoomed in to the mouth, seen in the upper portion of Figure 2.8b. The (red dots) denote the locations where depth was recorded during a previous cross-sectional survey. *Note: the satellite image was taken prior to the dates during which the cross-sectional survey was conducted (March 27^{th}, 2013), at which time the sand bank was further north; however, the satellite imagery serves as a good frame of reference, and is thus included.* (*Satellite imagery is from ESRI.*) 19

2.10 Surface wind magnitude and direction around the time of the nor'easter storm event, plotted in 6 minute intervals and averaged over 60 seconds, recorded on site with a weather station. The northeast winds are clearly visible, beginning on March 25^{th}. Several hours later, the wind speed tapers off as the center of the low-pressure system moves over the marsh, and then increases again, with slightly different direction. The winds continue to rotate westward over the next several hours. 20

2.11 Time series of $\eta(t)$ with the mean values separately subtracted. The subscript i in the y-axis label refers to each site, A-F. 21

2.12 Time series of $\eta(t)$ with the mean values separately subtracted. (a) before the storm event, neap phase; (b) during and shortly after the surge event, end of neap phase, beginning of spring phase; (c) after the storm event, end of spring phase, entering another neap phase beginning in April. The subscript i in the y-axis label refers to each site separately, A-F. 23

2.13 (a) Time series of measured depth at the channel mouth; (b) and (c) Time series of measured, depth-averaged, and filtered horizontal velocities in the East (u) and North (v) directions, respectively: (black) before storm event, (red) during storm event, (blue) after storm event. 24

2.14 Deployment of a catamaran vessel at mouth, near Site A, used to measure cross-sectional bathymetry. The picture is oriented in the direction looking towards Delaware Bay. The locations of the measured points are given in Figure 2.9. 25

2.15 Bathymetry of the cross-section measured at the mouth of Brockonbridge Gut, from traversing the inlet three times during a falling tide, as shown in Figure 2.9; (∗) Traversal #1, (•) Traversal #2, (o) Traversal #3. The solid line represents an approximated V-shaped channel, shown in Figure (2.16). Note: for reference, an axis into the page is in the landward direction, whereas an axis normal to the page, in the outward direction, is toward Delaware Bay. 26

2.16 Idealization of the cross-section taken at the mouth of Brockonbridge Gut 27

2.17 Stage-discharge curve for the inlet of Brockonbridge Gut computed by Eq. (2.4), where $\eta(x,t)$ is the surface elevation recorded at Site A by the piezometer in the ADCP. The line colors correspond to depths and velocities given in Figure 2.13: (black) before storm event, (red) during storm event, (blue) after storm event. 29

3.1 The effect of variable water depths on the drag coefficient, used in computing bottom stress in Eq. (3.15), for several different Manning numbers 39

4.1 DEM of the USGS LiDAR dataset collected in 2009. The larger marsh to the left is the Murderkill Estuary. The coverage area of Brockonbridge Marsh is outlined with a gray box. Delaware Bay is the body of water in the northeast corner of the image. (*Satellite imagery courtesy of ESRI*) 42

4.2 DEM of the smaller model domain used in phase one of model validation. Red dots denote the locations of Site B-F. The easting and northing values given are relative distances from the southwest corner of the domain. 44

4.3 Depth of channels measured during the surveys, interpolated onto the grid shown in Figure 4.2. The easting and northing values given are relative distances from the southwest corner of the domain. 45

4.4 Illustration of the correction for vegetation bias in a selected area from the original DEM. (a) High-resolution DEM; (b) Original 2 m resolution DEM; (c) Original 2 m resolution DEM with corrections applied for vegetation bias. A pressure gauge at Site 1 is labeled with a black triangle. 46

4.5 Depiction of adjustments applied to the original DEM. (a) Original DEM; (b) Black areas represent a mask for channels, mudflats and high-elevation areas where there is no presence of vegetation bias, so no corrections were applied; (c) Original DEM less the 15 cm bias in vegetated areas; (d) Final DEM, after passing a moving-window filter across the domain 4 times, to smooth out the noise. 46

4.6 Comparison between the north boundary at the mouth of two DEMs which have both been adjusted for vegetation bias, (left) before smoothing and (right) after smoothing. The black box in the left panel depicts a bulge which was successfully smoothed out. 47

4.7 Final DEM grid, demonstrating the results of adjustment for vegetation bias and smoothing. The black box in the upper right of the domain outlines where the boundary conditions are applied, as described in Figure 4.8. The locations of the pressure gauges are shown as red dots and labeled accordingly. 49

4.8 Visualization of the grid points at which the boundary conditions were imposed, marked with a red ($\mathbf{x}$). Sites B-F and Site 1 are marked with red dots and labeled accordingly. 50

4.9 Time series of the boundary condition which was imposed at the open boundary grid points of the small domain, which are marked with a red ($\mathbf{x}$) in Figure 4.8. 50

4.10 Model results for $\eta(t)$ vs field measurements, during the storm, for Sites B-F, and Site 1 as labeled in Figure 4.8; (a) Site B, (b) Site C, (c) Site D, (d) Site E, (e) Site F, (f) Site 1. The horizontal gray line marks the approximate marsh platform elevation at each site. — Field Data, - - Model Results 53

4.11 Instantaneous surface plots of computed $\eta(t)$ across the small domain, during the storm. (a) March 26^{th} 09:15, near high tide at mouth; (b) 4.5 hours later, March 26^{th} 13:45, during falling tide. Note the difference in scales for the color of η between the two plots. 54

4.12 Stage vs discharge curves for (a) Model results and (b) Field data, between the dates of March 21, 2013 14:00 and March 30, 2013 13:15, which include the storm, for the mouth of Brockonbridge Marsh. Note the difference in scales for the x-axis. 54

4.13 Model results for $\eta(t)$ vs field measurements, before the storm, for the open boundary, Sites B-F, and Site 1 as labeled in Figure 4.8; (a) North Boundary, (b) Site B, (c) Site C, (d) Site D, (e) Site E, (f) Site F, (g) Site 1. The horizontal gray line marks the approximate marsh platform elevation at each site. The bed elevation of Site 1 in panel (g) is 15 cm, so the channel goes dry for several hours each time the tide flows out, with the exception of the presence of the storm. Note the slight difference in the scales of the y-axis between the left and right panels. — Field Data, - - Model Results 55

4.14 Stage vs discharge curves for (a) Model results and (b) Field data, between the dates of March 21, 2013 00:00 and March 25, 2013 04:00, for the mouth of Brockonbridge Marsh. 56

4.15 DEM of the large domain, encompassing nearly all of Brockonbridge Marsh. Only elevations above 0 m (NAVD88) are shown in order to more clearly distinguish small differences in elevation. Sites A-F and Site 1 are marked with black dots and labeled accordingly. The locations along the North and East open boundaries where the boundary conditions are imposed are boxed with red lines. 59

4.16 Bathymetry of the large domain, encompassing nearly all of Brockonbridge Marsh. Only elevations below 0 m (NAVD88) are shown in order to more clearly highlight small differences in depth. 60

4.17 Time series of the boundary condition which was imposed at the open boundary grid points for the large domain, which are outlined with red boxes along the East and North open boundaries in the northeast corner of Figure 4.15. 61

4.18 Model results for $\eta(t)$ vs field measurements, during and after the storm, for Sites A-F and Site 1 as labeled in Figure 4.15; (a) Site A, (b) Site B, (c) Site C, (d) Site D, (e) Site E, (f) Site F, (g) Site 1. The horizontal gray line marks the approximate marsh platform elevation at each site. The bed elevation of Site 1 in panel (g) is 15 cm, so the channel goes dry for several hours each time the tide flows out, with the exception of the presence of the storm. Note the difference in the scales of the y-axis between the left and right panels. — Field Data, - - Model Results 63

4.19 Stage vs discharge curves for (a) model results and (b) field data, between the dates of March 24, 2013 05:15 and March 29, 2013 06:30. 64

4.20 Model results for $\overline{u}(t)$, $\overline{v}(t)$ and $|\overline{U}|(t)$ vs field measurements, during and after the storm, for Site A; (a) depth-averaged East/West velocities, (b) depth-averaged North/South velocities, (c) Magnitude of depth-averaged velocity. — Field Data, - - Model Results 65

5.1 Approximate analytic solution to time-varying coefficient diffusion equation in Eq. (5.4), with $n = 0.02$ and $||k_0||L = 1.562$. 72

5.2 Approximate analytic solution to time-varying coefficient diffusion equation in Eq. (5.4), with $n = 0.02$ and $||k_0||L = 3.492$. 72

5.3 Example of a Type A configuration. Grid used for model runs A1, A2 and A3. Note: the x-axis is in meters while the y-axis is given in kilometers. Inside the channel, Δx is 2 m. In the bay, Δy is 40 m. Not to scale. 74

5.4 Example of a Type B configuration. Grid used for model runs B1, B2 and B3. Inside the channel, Δx is 2 m, and Δy is 10 m. On the flats, Δx increases to also be 10 m, equaling Δy. In the bay, Δx is 10 m and Δy is 40 m. Not to scale. 74

5.5 Example of a Type C configuration. Grid used for model runs C1 and C2. Inside the channel, Δx is 2 m, and Δy is 10 m. On the flats, Δx increases to also be 10 m, equaling Δy. In the bay, Δx is 10 m and Δy is 40 m. Not to scale. 75

5.6 Example of a Type D configuration. Grid used for model runs D1 and D2. Inside the channel, Δx is 2 m, and Δy is 10 m. On the flats, Δx increases to also be 10 m, equaling Δy. In the bay, Δx is 10 m and Δy is 40 m. Not to scale. 75

5.7 Grid for model run D-SiteA (Type D). Inside the channel, Δx is 5 m, and Δy is 15 m. On the flats, Δx increases to also be 15 m, equaling Δy. In the bay, Δx is 15 m and Δy is 50 m. Not to scale. 76

5.8 Schematic setup of an idealized marsh with dunes separating the marsh platforms from open water. The variables which are defined are given for each case in Table 5.2. 77

5.9 Surface elevations for simulation A1, with $n = 0.02$ and $||k_0||L = 0.180$. The channel mouth is defined to be located at $x = L$, based on the notation used by Friedrichs and Madsen (1992). The landward end is defined at $x = 0$. 79

5.10 Surface elevations for simulation A2, with $n = 0.1$ and $||k_0||L = 0.403$. The channel mouth is defined to be located at $x = L$, based on the notation used by Friedrichs and Madsen (1992). The landward end is defined at $x = 0$. 80

5.11 Surface elevations for simulation A3, with $n = 0.2$ and $||k_0||L = 0.570$. The channel mouth is defined to be located at $x = L$, based on the notation used by Friedrichs and Madsen (1992). The landward end is defined at $x = 0$. 81

5.12 Stage-discharge curves for simulations A1, A2 and A3. 82

5.13 Surface elevations for simulation B1, with $n = 0.01$ and $||k_0||L = 0.758$. The channel mouth is defined to be located at $x = L$, based on the notation used by Friedrichs and Madsen (1992). The landward end is defined at $x = 0$. 83

5.14 Surface elevations for simulation B2, with $n = 0.02$ and $||k_0||L = 1.072$. The channel mouth is defined to be located at $x = L$, based on the notation used by Friedrichs and Madsen (1992). The landward end is defined at $x = 0$. 84

5.15 Surface elevations for simulation B3, with $C_d = 0.02$ and $||k_0||L = 2.056$. The channel mouth is defined to be located at $x = L$, based on the notation used by Friedrichs and Madsen (1992). The landward end is defined at $x = 0$. 85

5.16 Stage-discharge curves for simulations B1, B2 and B3. 85

5.17 Surface elevations for simulation C1, with $n = 0.02$ and $||k_0||L = 1.562$. The channel mouth is defined to be located at $x = L$, based on the notation used by Friedrichs and Madsen (1992). The landward end is defined at $x = 0$. 87

5.18 Surface elevations for simulation C2, with $n = 0.1$ and $||k_0||L = 3.492$. The channel mouth is defined to be located at $x = L$, based on the notation used by Friedrichs and Madsen (1992). The landward end is defined at $x = 0$. 88

5.19 Stage-discharge curves for simulations C1 and C2. 88

5.20 Surface elevations for simulation D1, with $n = 0.02$ and $||k_0||L = 1.562$. The channel mouth is defined to be located at $x = L$, based on the notation used by Friedrichs and Madsen (1992). The landward end is defined at $x = 0$. 89

5.21 Surface elevations for simulation D2, with $n = 0.1$ and $||k_0||L = 3.492$. The channel mouth is defined to be located at $x = L$, based on the notation used by Friedrichs and Madsen (1992). The landward end is defined at $x = 0$. 90

5.22 Stage-discharge curves for simulations D1 and D2. 91

5.23 Stage-discharge curve for simulation D-SiteA, where $\eta(t)$ is the surface elevation recorded at Site A. The line colors correspond to the time spans shown in Figure 2.13: (black) before storm event, (red) during storm event, (blue) after storm event. 92

5.24 Stage-discharge curves for simulations C2 and D1. 95

A.1 Comparison between model results from NearCoM and the exact solution from Thacker (1981). The bathymetry is shown in grey, the analytical solution for time, t, is shown in blue, and the numerical model computation is represented by the thick black line. (a) gives the initial configuration; (b) - (d) show the system at $\frac{1}{4}$, $\frac{1}{2}$, and $\frac{3}{4}$ the period of oscillation, respectively. Note that each plot is not to scale. The ratio of the vertical to horizontal length scale, $\frac{D_0}{L_1}$, is $O(10^{-3})$. . 107

ABSTRACT

In this work, the hydrodynamics of a salt marsh located along the coast of Delaware Bay are investigated through both a field study and numerical model. In order to obtain data for validation of the model, a field study was conducted on the main channel of Brockonbridge Marsh, which opens to Delaware Bay, in Kent County, Delaware. The study encompassed a full neap-spring tidal cycle, where pressure was measured at six locations in the main channel, while velocity profiles were recorded at the channel mouth. The velocity profiles are used along with a cross-sectional profile of the mouth to compute an estimate of total flux through the inlet.

Analysis of the tidal signals shows a fast rising tide, accompanied by a more slowly falling ebb tide, which is indicative of an estuary dominated by tidal variations in channel depth, rather than variations in estuary width. This suggests the wave crest diffuses landward faster than the trough. During deployment, a low-pressure system with strong winds directed onshore initiated a multi-day surge event, causing the duration asymmetry to become even more pronounced.

In addition to pressure and velocity measurements, two bathymetric surveys of the main channel were conducted to obtain a detailed map of the main channel. The data from these surveys are combined with LiDAR data to create a high-resolution, topo-bathy Digital Elevation Model (DEM) of the marsh. Two important characteristics of Brockonbridge Marsh are observed from the DEM, which separate it from the typical accepted definition for the geometry of a salt marsh. First, the marsh platform experiences a decrease in elevation with distance increasing from the bay. Second, the channel depth does not monotonically decrease further inland. Instead, it is shallow near the mouth, then suddenly deepens, followed by a general decrease in depth moving inland.

The maximum attainable water level at any point in the main channel does not appear to be influenced by the surface elevation at the inlet. Rather, the maximum is governed by the local geometry of the marsh in the immediate vicinity of the channel, which is a direct consequence of the negatively sloping marsh platform.

The high-resolution DEM and field data are used with the Nearshore Community Model (NearCoM), a quasi-3D numerical model, to perform a validation. A small domain which does not encompass the entirety of Brockonbridge Marsh is first used. The small domain represents water levels and total flux through the mouth very well for the neap phase of the data, when the tidal flats are seldom inundated. However, with the arrival of the storm, the small domain fails to adequately account for the sudden surge of water onto the marsh platform. When the domain is expanded to encompass nearly all of the floodable surface of Brockonbridge Marsh, the total discharge computed by the model under-predicts the field observations during the storm. Furthermore, the expanded domain exhibits difficulty in draining the marsh. Computed water levels in more landward areas of the channel are higher in the model when compared to field data.

Finally, it is shown how different marsh geometries can have profoundly different effects on tidal distortion. Ideal channelized salt marshes are classified into four categories based on their tidal flat configuration. Each type is modeled with NearCoM using different friction factors. For short estuaries, it is found that the presence of tidal flats serves as one of the major mechanisms in distorting the tide, leading to ebb/flood dominance. Furthermore, maximum attainable tidal amplitude is shown to be highly dependent on the direction in which the marsh platform increases in elevation. When compared to tidal propagation through a marsh with positively sloping tidal flats in the landward direction, water levels in the idealized marsh with negatively sloping flats exhibit trends much more similar to the field observations.

Chapter 1

INTRODUCTION

Salt marshes are found ubiquitously in low energy, estuarine environments along the East Coast of the United States. It is typical for a salt marsh to be partially or fully flooded during high tides (Boon et al., 1977). In many instances, they are characterized by a complex network of channels and surrounding flats (Temmerman et al., 2005; Mariotti and Fagherazzi, 2012). The flats are usually vegetated with grasses that are tolerant to a saline, brackish environment (Barbour, 1978). Different species of marsh grass exist in different elevations, based on the frequency in which that particular area of the marsh is flooded (McKee and Patrick, 1988). Marsh vegetation typically occupies elevations between mean sea level and mean high water (Kirwan and Guntenspergen, 2010). The bed material is usually composed of a mixture of inorganic mud and highly organic decayed plant matter, called peat (Mudd et al., 2009).

It is common for salt marshes in the Mid-Atlantic region to be bisected by one or more primary channels, from which several slightly shallower and more narrow secondary channels branch off (Allen, 2000). These secondary channels can have even smaller tertiary channels branching out in either direction. The result is a highly complex network of meandering channels, with the total length and average width and depth typically decreasing with each successive branch (D'Alpaos et al., 2009). As a result, modeling the hydrodynamics of these systems becomes very complicated.

Many studies in the past have focused on modeling the complex hydrodynamics in tidal marshes (Speer and Aubrey, 1985; Rinaldo et al., 1999; Temmerman et al., 2003). Rinaldo et al., (1999) developed a hydrodynamic model using a set of equations describing the 2-D, depth-averaged flow field on a tidal marsh platform. Their model contained several highly simplified assumptions about the propagation of the tide onto

the platform, including constant friction in space and time and an instantaneous vertical adjustment of the water level during flooding.

Several numerical models for salt marsh evolution have been developed over the past decade which couple geomorphological and ecological processes to predict landform evolution (see Fagherazzi et al., 2012 for an extensive review). However, these numerical frameworks are typically based on simplified assumptions and sparse data sets which are usually site-specific.

In addition, these studies tend to use domains with low spatial resolution (Kjerfve et al., 1991) to characterize friction factors and estuarine circulation. This has worked for estuarine environments that encompass a large area, in which length scales over which significant changes occur are on the order of several kilometers. However, low-resolution grids can improperly smear out sharp variations in bathymetry, which can cause the model to overestimate the friction, resulting in an under prediction of total flux. Volp et al., (2013) use the Chézy Equation for discharge to further explain this idea. They consider a channel with two different depths in the transverse direction, H_1 and H_2. Essentially, since the discharge is a function of $H^{3/2}$, where H is total water depth, the total discharge through the channel when considering both depths is always greater than or equal to the total discharge when using the average depth.

While a trade off for computational time must be made, the use of high-resolution grids in channelized estuarine environments can provide a better understanding of the overall circulation patterns and discharge. High-resolution models are especially useful when many of the momentum transporting channels have width on the scale of one or two model grid cells in the highly resolved domain.

When investigating more simplified cases, present models typically assume either an open ocean or a shallow tidal basin at one end of the domain, with a higher elevation salt marsh at the other end, separated from the tidal flat by a steep escarpment (Mariotti and Fagherazzi, 2010; Marani et al., 2011). Another typical assumption made is that the elevation of the marsh increases in the landward direction (van der Wegen, 2010).

While it has been shown to be characteristic of most tidal marshes to exhibit a general, monotonic increase in elevation of the platform with distance inland (Stoddart et al., 1989; Cahoon and Reed, 1995), the marsh being studied in the following manuscript, Brockonbridge Marsh, experiences a decrease in elevation with distance inland. Also, unlike the typical assumption of a steep scarp separating the platform from open water, Brockonbridge Marsh is protected from open waters by sand dunes, cut by a single inlet. As a result of these two distinct deviations from the standard model, flow through the inlet is the major conduit for water entering the marsh, while the flooding of the marsh platform begins in the most landward reaches of the domain.

In both present and historical literature, when investigating circulation patterns and flux asymmetries, there is a lack of consideration for marsh platforms with this negatively sloping configuration. The implications of the unique nature of Brockonbridge Marsh on its hydrodynamics are the main focus of this study.

1.1 Motivation

Delaware's coastal wetlands are home to a large variety of aquatic species and waterfowl. Migratory birds utilize many of the tidal marshes along Delaware Bay as breeding grounds and staging areas during migration seasons. The beaches and wetlands along the coast of Delaware Bay are also home to the largest spawning population of horseshoe crabs in the world. The importance of these tidal marshes in Delaware Bay has raised concerns about their survivability under future sea level rise conditions.

Historically, marshes around the world have been able to keep pace with rising seas. But with recent studies showing an acceleration in global sea level rise (Church et al., 2001; Church and White, 2006), the question of whether marshes around the world can keep pace becomes a more pressing issue. Numerous studies have investigated the impact an accelerated rise in sea level (Kirwan and Temmerman, 2009; Craft et al., 2009).

A study conducted by the EPA investigated the implications of different rates of Sea Level Rise (SLR) on coastal wetlands in the Mid-Atlantic region (Titus et al., 2008).

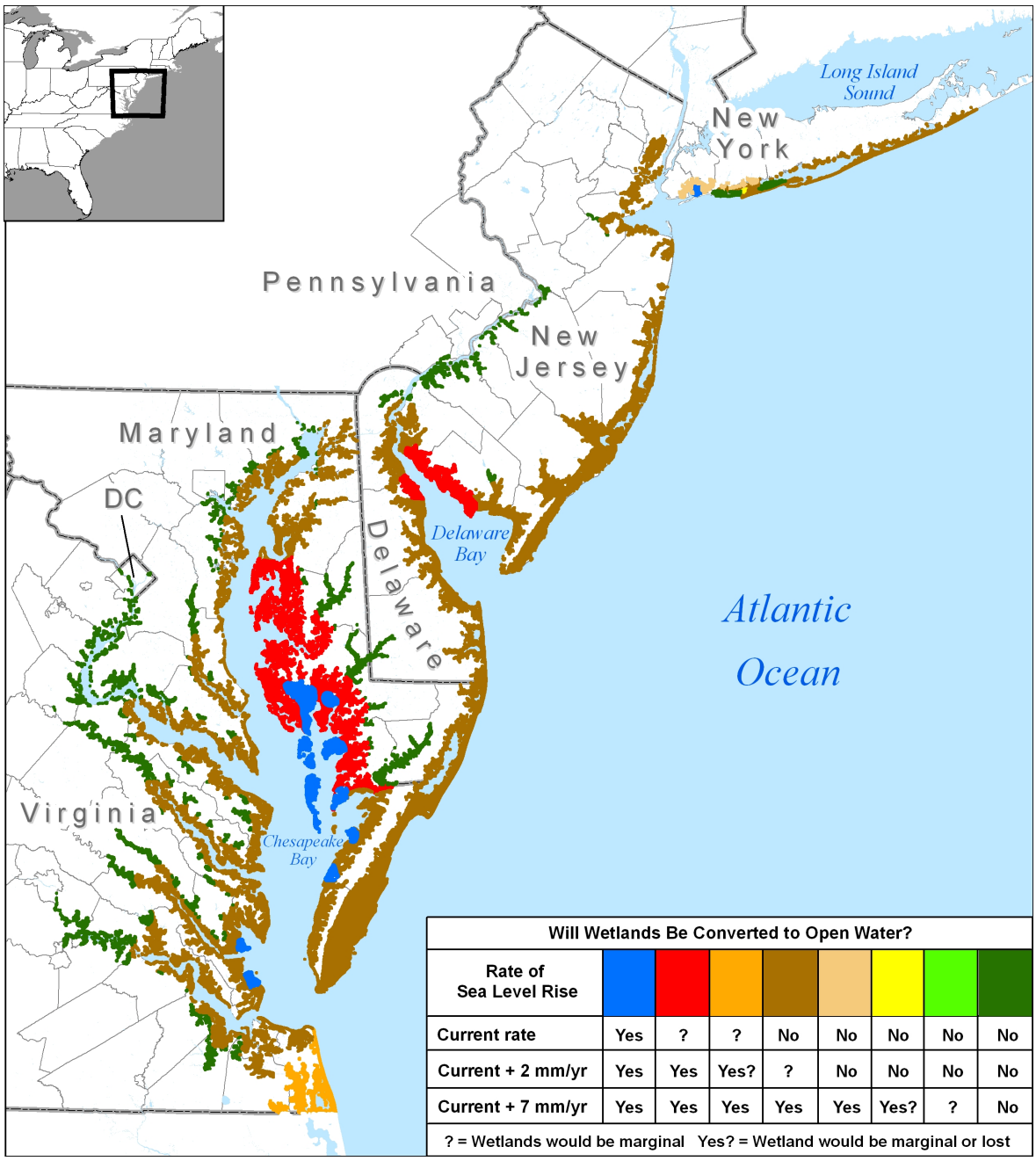

Figure 1.1: Potential risk for wetland loss in the Mid-Atlantic region due to different rates of Sea Level Rise (*Adopted from Titus et al., 2008*)

The study concluded at the current predicted rate of SLR, several wetland regions in the Chesapeake and Delaware Bays will be marginally lost (Figure 1.1). In particular, the area outlined with red in Figure 1.1 on the Delaware coast is Bombay Hook, a National Wildlife Refuge. With an additional 2 mm/yr above the current predicted rate of SLR, the area of wetlands that are predicted to be marginally converted to open water further increases to encompass nearly the entire coastal area in the Chesapeake and Delaware Bays.

Moreover, substantial quantities of contaminants reside in Delaware Bay (Greene and Miller, 1994). Specifically, Polychlorinated Biphenyls (PCBs) have been observed in elevated levels in the fringing marshes along Delaware Bay (Figure 1.2). While PCBs in the marshes are typically buried 20 to 30 cm beneath the surface (Velinsky et al., 2011), rising seas pose a threat in exposing these contaminants, due to potential marsh degradation (March and Smith, 2012).

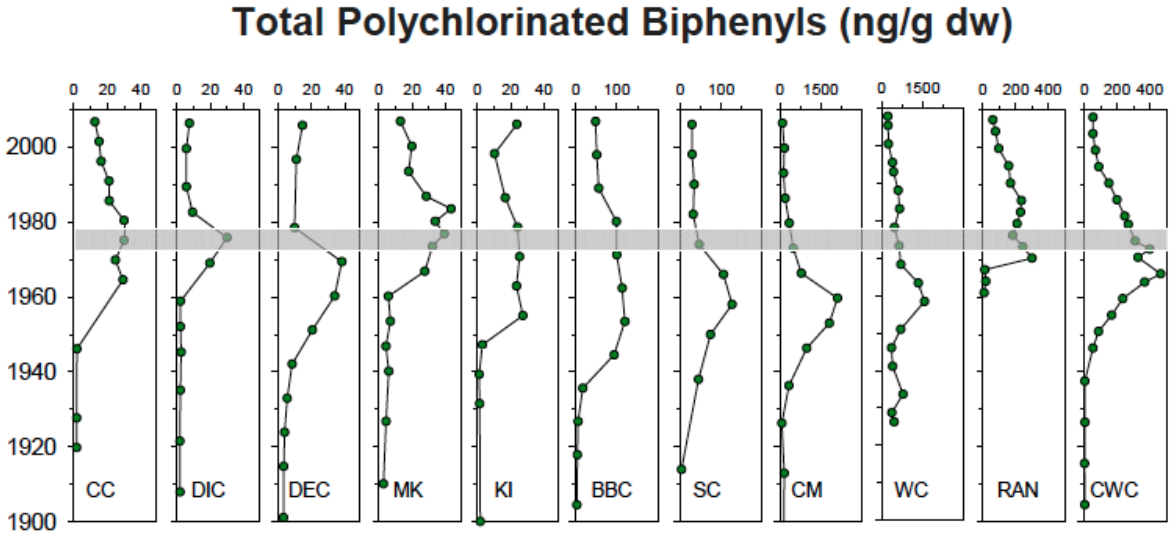

Figure 1.2: Total Polychlorinated Biphenyls (PCBs) in select Delaware Bay marshes. Each panel represents a different marsh, labeled with acronyms at the bottom, from the lower to upper Delaware Bay moving left to right. The gray bar across the panels marks the time period when use of PCBs was banned. (*Adopted from Velinsky et al., 2011*)

Chapter 2

FIELD STUDY

2.1 Introduction

A field study was conducted on the main channel of Brockonbridge Marsh in Kent County, Delaware, which opens to Delaware Bay. The study lasted two weeks during March and April 2013 and encompassed a full neap-spring tidal cycle. Of particular interest was understanding how the predominately semi-diurnal tide propagates throughout the marsh, given its complex network of secondary and tertiary channels. In order to measure surface elevation, five pressure gauges and an Aquadopp Profiler (ADCP) were deployed at six various locations, spanning 2.5 km along the channel axis. The ADCP was deployed at the channel's mouth to record the velocity profile.

Additionally, in the summer of 2013, two extensive surveys of the main channel's bathymetry were completed. These surveys provided high-resolution bathymetry data which were used to create a full topobathy digital elevation model (Mieras et al., 2014).

In the following sections, a description of the marsh, along with a description of why it was selected for this study, are presented. Next, the two data collection phases are discussed, starting with the pressure and velocity measurements, then moving to surveying the main channel. Finally, a brief report on the data analysis is given, followed by a brief discussion of the results of the analysis.

2.2 Description of Marsh

Brockonbridge Marsh is a tidal salt marsh which empties into Delaware Bay, located along the coast of Kent County, Delaware. Its geomorphic setting can be classified as saline fringe (Figure 2.1).

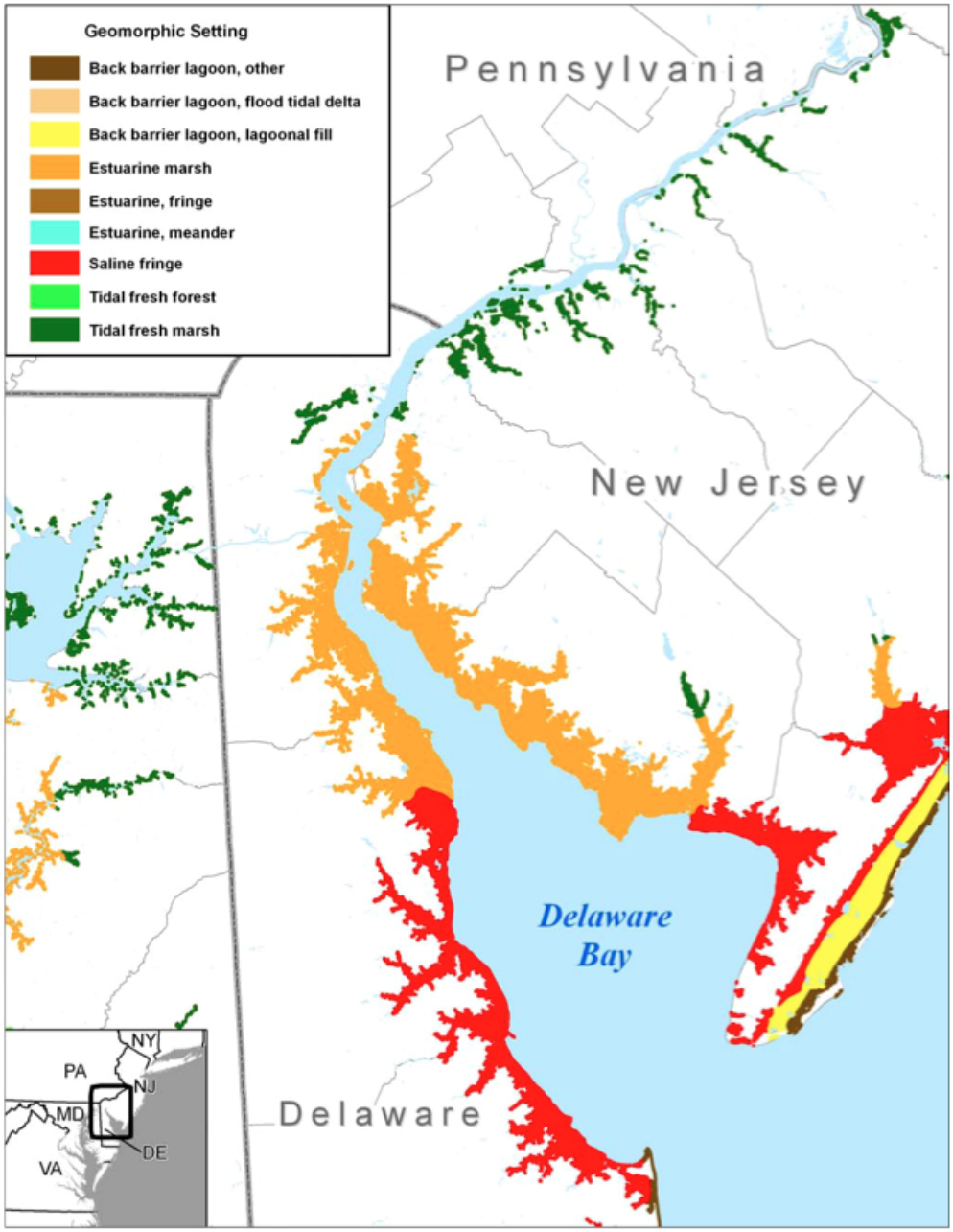

Figure 2.1: Map of the geomorphic settings of coastal areas along Delaware Bay (*Adopted from Titus et al., 2008*)

It is located about two kilometers south of the small coastal town of Bowers, DE, which sits in between the mouths of the Murderkill River and the St. Jones River. Brockonbridge Marsh (BM) is on the order of approximately 10 square kilometers in area. The marsh is protected by sand dunes along Delaware Bay and is predominantly surrounded by higher-elevation farmlands.

With the exception of spring high tides, at which time the marsh becomes interconnected with the Murderkill river to the northwest, the tide enters the marsh through the mouth of its main channel, referred to hereafter as the Brockonbridge Gut (BG). The BG runs primarily in the Northeast/Southwest direction (Figure 2.2).

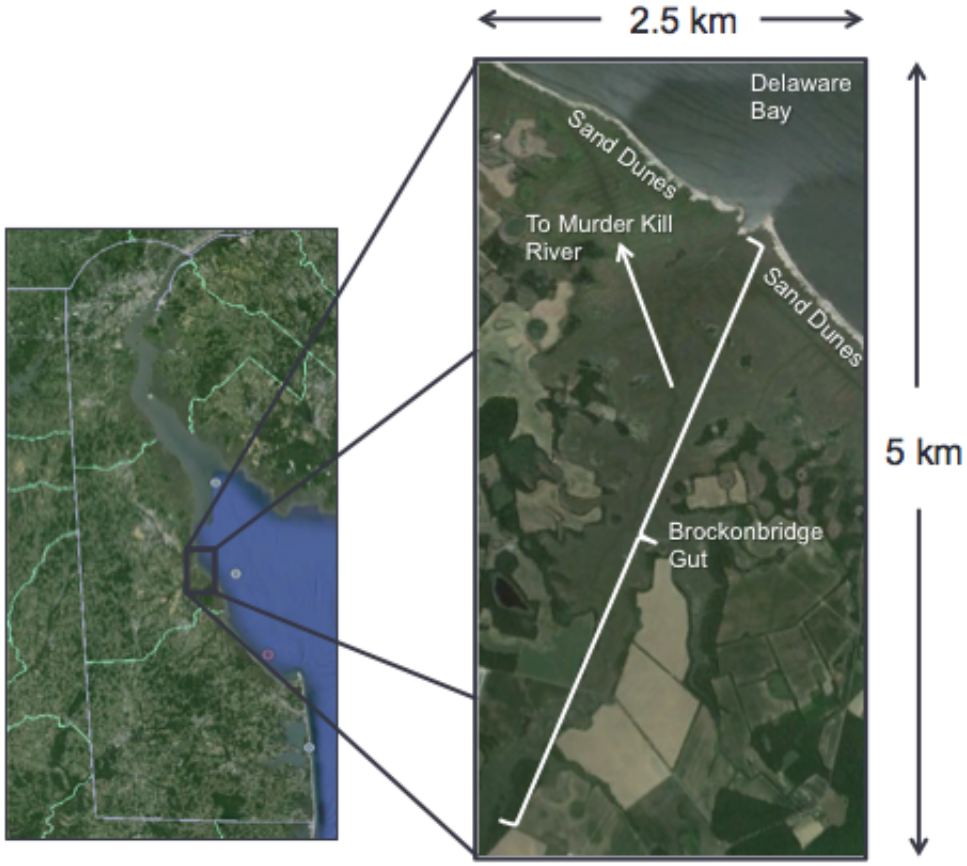

Figure 2.2: Satellite image of Brockonbridge Marsh showing its location in Kent County and that it covers an area 5-10 km^2, with Delaware Bay in the upper right corner (*Imagery courtesy of Google Earth*)

The mouth of the BG is roughly 15 meters wide during low tides and can get

up to 20 meters wide during high tides, where the tidal range is about 1 to 1.5 meters, depending on whether it's neap or spring tide. As a result, the overall depth of the channel at the mouth ranges from 1 meter to 2.5 meters.

The width of the channel exhibits an overall gradual narrowing with distance increasing inland, from about 25-30 m wide near the mouth, to less than 10 m wide four kilometers inland. The overall characteristic width of the entire marsh also exhibits the same gradual narrowing trend (Figure 2.2).

The marsh platforms are characterized by a decreasing slope moving landward from the bay. This is perhaps the most intriguing feature of this marsh, as almost every study regarding the modeling of marsh hydrodynamics and morphodynamics assumes a gradual increase in elevation with distance increasing landward. The consequences of these two different configurations on tidal propagation and residual flow will be investigated further in a later chapter.

Remnants of digging artificial ditches in high-marsh areas during the early nineteenth century are present in areas of the marsh near the bay (Figure 2.3).

Figure 2.3: Satellite image showing an example of the artificial, man-made ditches, called "mosquito ditches," in the upper Brockonbridge Marsh (*Imagery courtesy of Google Earth*)

(a) (b)

Figure 2.4: (a) An example of *Spartina alterniflora* in Brockonbridge Marsh; (b) An example of *Spartina patens* present in higher elevations of the marsh, which are inundated less frequently.

As a result of the elevation difference, the types of vegetation which are present in the marsh vary from a mix of *Spartina patens* and *Spartina alterniflora* in the regions closer to the bay, to predominately *Spartina alterniflora* further inland (Figure 2.4). Furthermore, the *Spartina alterniflora* which grows along the channel edges is generally taller than the *Spartina* grasses that do not grow near channels (Morris et al., 2002; Mudd et al., 2009). Consequently, the channels throughout the marsh exhibit a levee system along their edges (Temmerman et al., 2005).

These "levees" are clearly visible in an aerial photograph taken of the marsh shortly after Hurricane Sandy struck the East Coast in November 2012 (Figure 2.5). The ponded water in the back of the marsh shows higher elevation dikes which have formed adjacent to the channel banks. Figure 2.5 also shows the negatively sloping marsh platform away from the bay, which is illustrated by the ponding of water near the back of the marsh.

2.3 Site Selection

Due to the muddy and soggy nature of tidal marshes, access by foot is usually limited to just tens of meters away from higher elevated, dry land, before the ground becomes too soggy to walk on. Furthermore, access to these areas by any motor vehicle

Figure 2.5: Aerial photograph of Brockonbridge Marsh, taken from an airplane flying over Delaware Bay, along the coast of Delaware, after Hurricane Sandy in 2012 (*Photo courtesy of Art Trembanis, University of Delaware, Geology 2012*)

is nearly impossible without sinking into the mud. As a result, selecting a marsh for a comprehensive study is highly dependent on its accessibility. In the case of the BM, there were numerous access points, by both land and water, with a nearby public boat launch at the Murderkill River. The mouth of the main channel was accessible by kayak, boat, ATV and foot, which provided many options. There is also a small bridge which crosses the marsh roughly 3 km inland, serving as a good solid surface for deployment of any instruments.

Additionally, as is shown in Figure 2.3, the areas of the upper marsh near the bay are incised with man-made "mosquito ditches." The role in which these ditches play in the overall hydrodynamics and morphodynamics of tidal marshes was of principle interest at the onset of this study. The presence of many man-made channels added to the site's attractiveness.

Although the aforementioned characteristics of Brockonbridge Marsh seemed to be enough to qualify this as a good marsh for a field study, it was the availability of several high-resolution Digital Elevation Models (DEMs) that classified this as a good marsh for a comprehensive study. Access to the DEMs, coupled with the high accessibility, would make it possible to conduct a detailed model validation.

The overall size of the marsh is also rather small, as shown in Figure 2.2. This made it possible to conduct extensive bathymetry surveys of the main channel over the course of just several hours. Consequently, these data could be combined with the high-resolution DEMs to create a full topo-bathy DEM of the marsh, which could be used in modeling the details of the marsh's hydrodynamics.

Finally, alongside the field study conducted on the main channel, a smaller scale study was planned to be carried out on a small tributary of the BG by Jack Puleo and Aline Pieterse from the University of Delaware's Center for Applied Coastal Research, and Thomas McKenna from the Delaware Geological Survey. The study investigated flow patterns during tidal inundation of a mudflat, at a much smaller scale. A collaboration with this group would provide access to more data that would be used to further validate the hydrodynamics of a numerical model.

All of these factors are difficult to find all together in most marsh studies around the world. The combination of these unique aspects provided for the collection of large scale and small scale tidal and bathymetry data, as well as the use of these data in the validation of a hydrodynamic model, all in a single study.

2.4 Field Methods

The first phase of the field study took place between March 20^{th}, 2013 and April 4^{th}, 2013. Phase I of data collection involved deploying a total of 7 instruments throughout the main channel, Brockonbridge Gut (Figure 2.6). The goal of the deployment was to encompass a full 14-day spring-neap cycle, which would provide enough data to extract the lower frequency, fortnightly constituents.

The second phase of the study consisted of mapping the bathymetry of the BG and all tributary channels that were navigable during spring high tides.

Details of the data collection methods for these two phases are discussed below.

2.4.1 Measuring Pressure and Tidal Currents

A total of five pressure gauges were deployed at various locations in the channel. In addition to recording velocity profiles, the Aquadopp that was deployed at the channel mouth also recorded pressure. The seventh instrument, a Conductivity, Temperature and Depth (CTD) gauge marked with a green dot at Site G, was not recovered. As a result, pressure data was recorded at a total of six sites, hereafter referred to as Sites A-F, labeled in Figure 2.6. A concerted effort was made to equally distribute them throughout the channel, as well as to cover the largest extent of the channel as possible. As a result, the distance between gauge A (located at the mouth) and gauge F (located as far inland as was navigably possible with the outboard motor during low-tide) is about 2.5 km along the channel's centerline. The measured distance of each from Site A is listed in Table 2.1.

A 2 MHz ADCP was deployed at the mouth of BG, directly on the bottom, in an upward facing configuration. Velocity profiles were measured every 6 minutes,

Figure 2.6: Layout of instrument locations in Brockonbridge Marsh. The black dot near the upper left corner marks the location of a USGS tidal and discharge gauge station, at the mouth of the Murderkill River. The location labeled Site G is the aforementioned small bridge in the discussion of site selection. (*Satellite imagery is from ESRI.*)

Table 2.1: Total along-channel distance from Site A to each of the sites in the Brockonbridge Gut, as well as the representative percentage of the total distance. Along-channel in this case is defined as the total distance along the channel's centerline.

	Distance from Site A (m)	% of Total
Site B	251	9.87
Site C	810	31.86
Site D	1,480	58.22
Site E	2,089	82.18
Site F	2,542	100.00

averaging over 60 seconds, with a vertical cell size of 10 cm and a blanking distance of 10 cm. The pressure sensors recorded a value every three minutes, since they were not as limited as the ADCP for battery life.

2.4.2 Bathymetric Surveys

Two surveys were conducted on July 26^{th} and August 24^{th}, 2013, during spring high tides when the width of the channel is at a maximum, to ensure the greatest number of depth measurements could be made (Figure 2.7). As is evident in Figure 2.7, different survey courses were taken on each day. This allowed for more extensive coverage of the major channels.

The data from the two separate surveys were combined and the kriging technique was used in ArcMap to interpolate the measured elevations onto a structured grid. For the model domain, the points were interpolated onto a grid with 2 meter resolution, consistent with the resolution of the LiDAR DEMs. However, the two images displayed in Figure 2.8 are a result of kriging onto a grid with 1 meter spacing, solely for the sake of visually showing a higher resolution map of the channel bathymetry. The elevations are shown with respect to the NAVD88 datum, which was used because the DEMs used in the creation of a full topo-bathy grid used NAVD88 as their vertical datum.

A couple of interesting points are notable from the survey results given in Figure 2.8. First, in the ∼300 m span near the mouth, before the channel undergoes an abrupt meander, the elevation remains relatively constant, around -1 meter NAVD88. Then

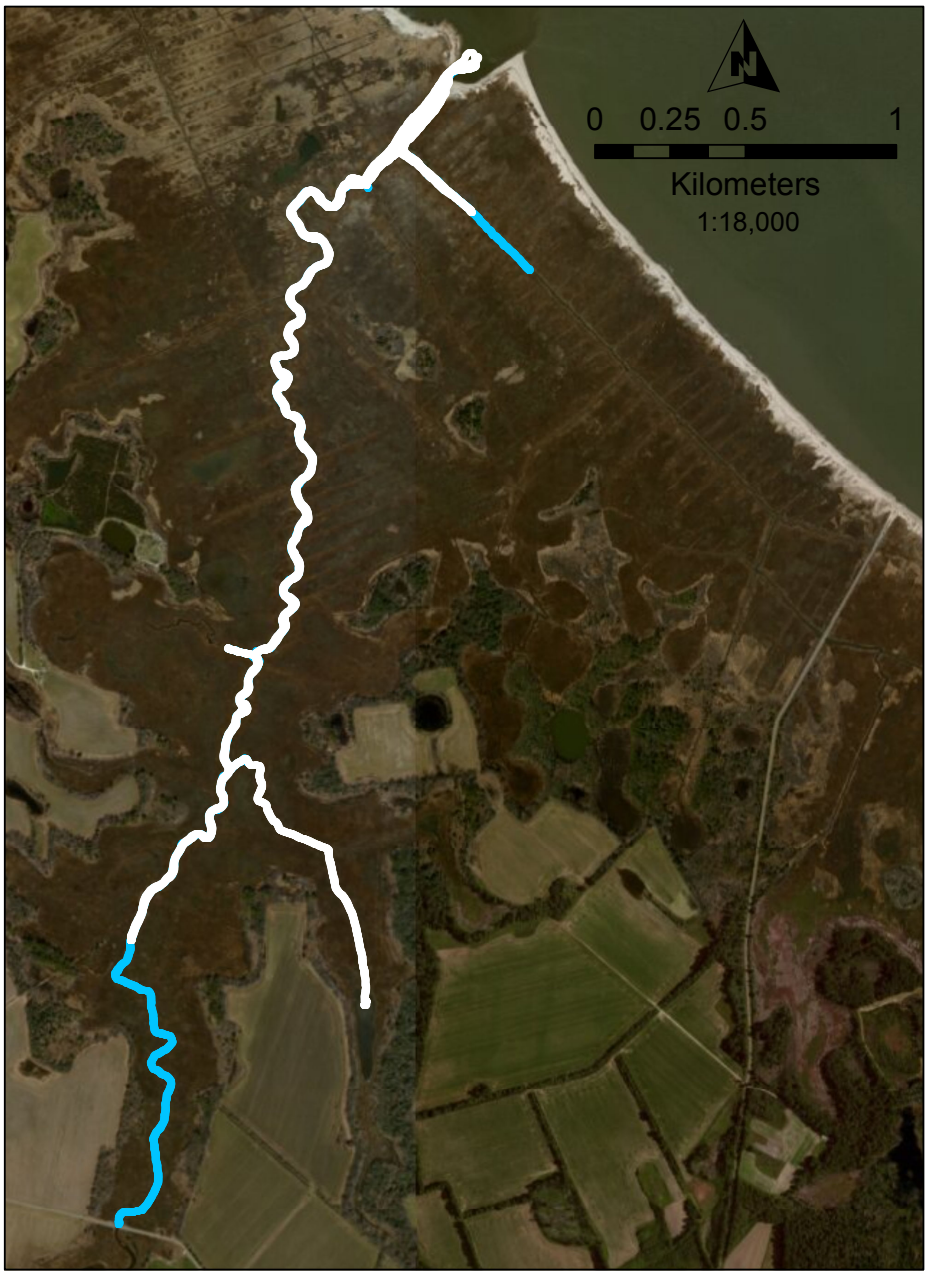

Figure 2.7: The extent of Brockonbridge Gut which was covered during each survey: (blue dots) survey conducted on July 26^{th}, 2013; (white dots) survey conducted on August 24^{th}, 2013. (*Satellite imagery is from ESRI.*)

(a) (b)

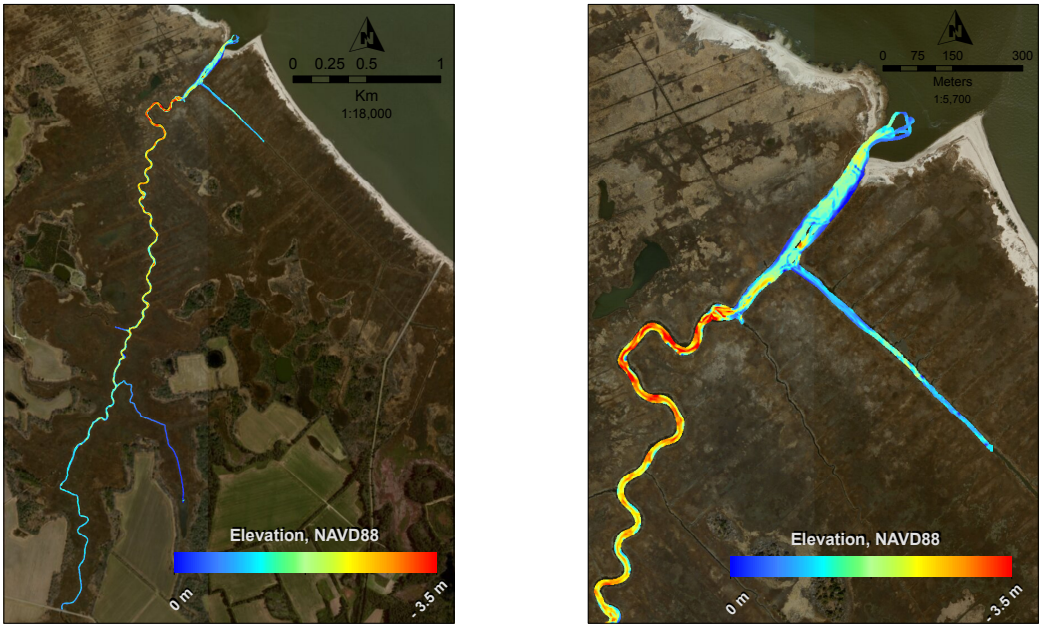

Figure 2.8: Interpolated bathymetry of Brockonbridge Gut and its navigable branches, computed with the kriging technique. (a) The entire Brockonbridge Marsh up to the bridge; (b) Enlargement of domain near the mouth. The grid spacing is 1 meter. The maximum search radius was 3 meters, with a maximum of 10 nearest points used during interpolation. *Note: the satellite image was taken prior to the dates during which the bathymetric surveys were conducted, at which time the sand bank near the mouth was further north; however, the satellite imagery serves as a good frame of reference, and is thus included.* (*Satellite imagery is from ESRI.*)

the channel experiences a sharp increase in depth over a short distance, just before the first meander. The elevation of the bed suddenly drops down to -3 meters NAVD88, and even below -3.5 meters NAVD88 in several areas (Figure 2.8b). Moving inland from the sudden deepening at the first meander, the main channel exhibits an overall increasing trend in bed elevation, reaching a bed elevation of ∼0.8 meters NAVD88 two kilometers inland (Figure 2.8a). There are numerous sections that experience sharp gradients in elevation; however, these areas are localized and are likely constantly changing magnitude and location from erosion and deposition over time. Some of these spots might also be local oyster beds. A couple of likely oyster beds are visible as blue spots surrounded by green and yellow colors to the left of the scale bar in Figure 2.9.

This unusual trend in channel bed elevation is an intriguing discovery, as many tidal marsh studies which don't have detailed bathymetry maps typically assume channel depth to be deepest at the mouth, then decreasing monotonically further inland. But the main channel of Brockonbridge Marsh clearly does not follow this trend. In fact, while the width of the channel from the mouth to the bridge undergoes significant narrowing, the channel bed elevation is almost equivalent in these two areas, separated by over 3 kilometers in along-channel distance. To a lesser degree, the southeastward branching channel shown in Figure 2.8b exhibits a similar span of constant depth, followed by an abrupt deepening, only to become shallow once again.

2.5 Data Analysis and Discussion

The total water depth at the mouth was computed using data recorded by the piezometer on the ADCP and applying salt water corrections. The same was done for data measured by the 5 pressure gauges. All pressure data was also corrected by removing atmospheric variations in pressure, which were collected during the entire deployment using a locally deployed weather station constantly recording in-situ weather conditions on site (see Mieras and Kirby, 2014 for more details).

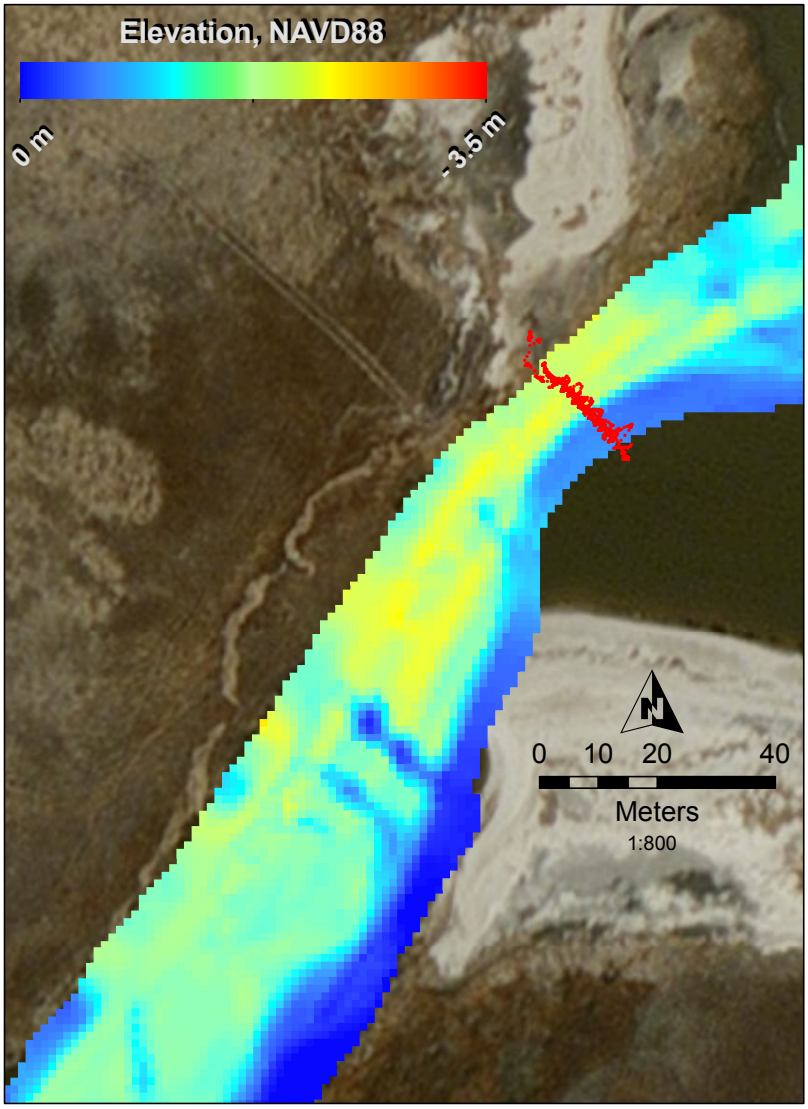

Figure 2.9: Interpolated depth surface from bathymetric surveys, zoomed in to the mouth, seen in the upper portion of Figure 2.8b. The (red dots) denote the locations where depth was recorded during a previous cross-sectional survey. *Note: the satellite image was taken prior to the dates during which the cross-sectional survey was conducted (March 27th, 2013), at which time the sand bank was further north; however, the satellite imagery serves as a good frame of reference, and is thus included.* (*Satellite imagery is from ESRI.*)

During the deployment, a nor'easter wind event occurred (Figure 2.10) with a duration of approximately 12 hours, resulting in a considerable surge of water across the marsh. This caused a multi-day set-up in surface elevation throughout the marsh. This surge event contributed to the presence of a highly non-stationary component in water level, which can be seen in Figure 2.11 during March 25^{th} through March 26^{th}.

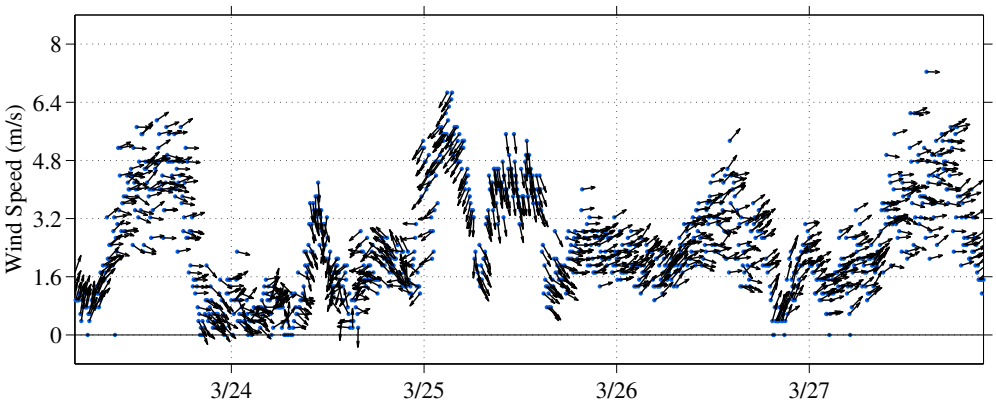

Figure 2.10: Surface wind magnitude and direction around the time of the nor'easter storm event, plotted in 6 minute intervals and averaged over 60 seconds, recorded on site with a weather station. The northeast winds are clearly visible, beginning on March 25^{th}. Several hours later, the wind speed tapers off as the center of the low-pressure system moves over the marsh, and then increases again, with slightly different direction. The winds continue to rotate westward over the next several hours.

In the following sections, the presence of asymmetries in tidal propagation through Brockonbridge Gut, resulting in shorter rising and longer falling tides, will be discussed. In addition, the stage relationship between volumetric discharge and water levels, as well as variations in the distortion of this relationship on a fortnightly timescale, will be analyzed. Finally, the modulations to these attributes as a result of the surge event will be discussed.

2.5.1 Lack of Vertical Control

First, it's important to mention that during the deployment and retrieval of the gauges in the channel, an effort was made to record the elevation of the bed on which the instruments were deployed. However, the stability of the small vessel used

in deployment limited our ability to record the exact elevation of the bed with respect to a fixed datum. Instead, the only GPS data which were recorded reliably were the easting and northing positions of each instrument. Due to this, there is no vertical control on the values of surface elevation with respect to a fixed datum. The depths are known, but without knowledge of the elevation of the bed at each site with respect to a certain datum (i.e., NAVD88), it's impossible to know the surface elevation, $\eta(t)$, with respect to any datum either.

An attempt was made to use the known elevation(s), with respect to NAVD88, from the nearest data point(s) in the aforementioned bathymetric surveys conducted several months later. But obvious issues were apparent in three of the signals, where the depth which was estimated from the surveys was clearly off by up to half a meter. This could be due to a sharp gradient being present in the area of the gauge, where even the nearest measured elevation point, though possibly being within 10 cm of the gauge's known easting and northing position, could be off by tens of centimeters. This could also be due to some areas of the channel bed having undergone erosion/accretion between April and July/August.

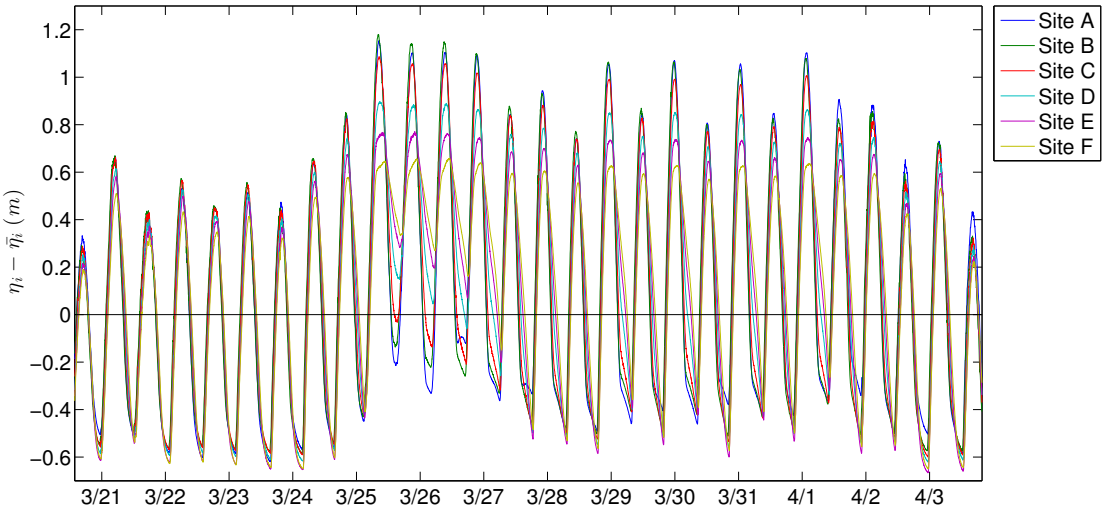

Figure 2.11: Time series of $\eta(t)$ with the mean values separately subtracted. The subscript i in the y-axis label refers to each site, A-F.

As a result, when referring to η throughout the remainder of this paper, it

should be understood that there is a lack of vertical control. In order to obtain a relation between the surface elevation at the mouth and the stations throughout the marsh, the mean value of η from each gauge was subtracted, making the mean value of each curve equal to zero. Finally, 0.1 m was added to every curve, as shown in Figure 2.11. The reader is referred to Mieras and Kirby (2014) for a more detailed discussion of this matter.

2.5.2 Pressure and Velocities

The resulting variations in surface elevation for the 14-day deployment are marked by three distinct time spans, as pictured in Figure 2.12. While, in general, the tide in Brockonbridge Gut is characterized by a more quickly rising tide followed by a slower falling tide, the differences in these phase shifts are very dependent on the marsh geometry.

Variations in surface elevation during neap phase are shown in Figure 2.12a. In this period of time, phase lags during rising and falling tides are more likely governed by varying channel depth. This is because the water levels during this phase rarely reach levels high enough to inundate any considerable amount of marsh platform. LeBlond (1978) explains the lag in tidal phase is due to frictional forces dominating inertial forces over the majority of the tidal cycle. As a result, the propagation of the tide can be explained by a diffusive wave through a shallow embayment. Friedrichs and Madsen (1992) further point out that by accounting for time variations in the diffusion coefficient, for tidal channels dominated by changes in water levels, as is the case in Figure 2.12a, there is a mean set-up in the channel, resulting in shorter rising tides and longer falling tides. A further investigation into how well the time-varying diffusion solution of Friedrichs and Madsen (1992) explains the observed phenomena in Figure 2.12a is conducted in Chapter 5.

The storm's arrival is marked by a sudden surge of water into the marsh on March 25^{th} (Figure 2.12). The effect of the negatively sloping marsh platform away from the bay is seen by the separation in maximum water levels reached at each site

during the surge event. With distance increasing landward, the marsh platform becomes lower. As the water begins to spill out of the channel and onto the flats, the rate of increase in water level decreases. This is due to a sudden lateral spreading of the water in the transverse direction. The locations closer to the bay are lined with large levees in either side of the channel and are thus able to support higher water levels.

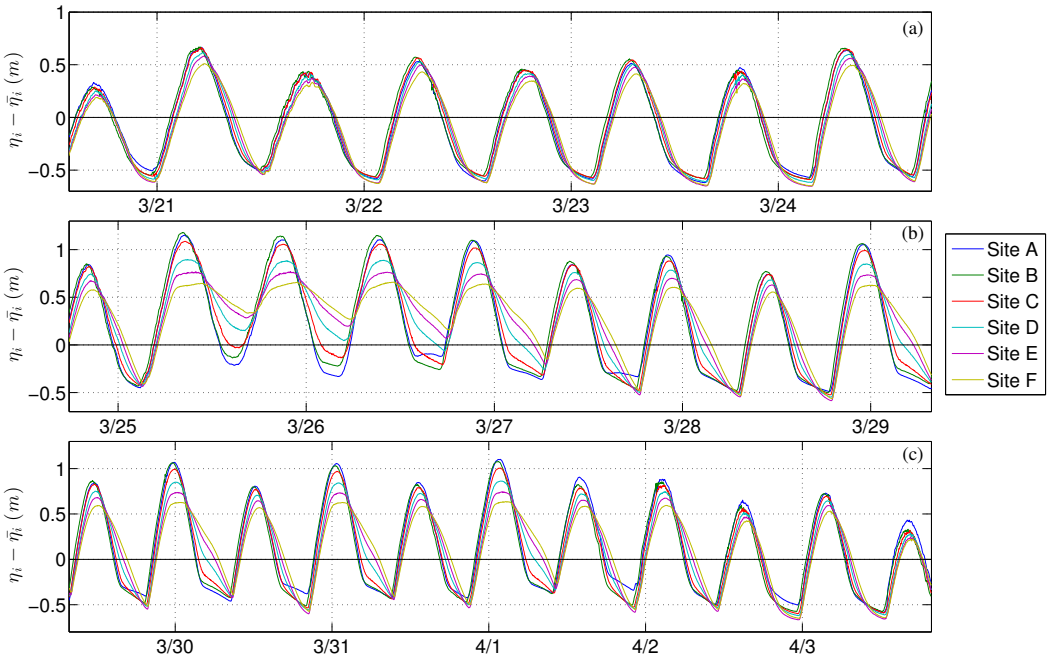

Figure 2.12: Time series of $\eta(t)$ with the mean values separately subtracted. (a) before the storm event, neap phase; (b) during and shortly after the surge event, end of neap phase, beginning of spring phase; (c) after the storm event, end of spring phase, entering another neap phase beginning in April. The subscript i in the y-axis label refers to each site separately, A-F.

It takes a couple days for the low tides throughout the marsh to return to the typical levels. During this period, the variation between water levels at low tide and high tide becomes noticeably smaller with distance increasing from the mouth. By the time the water surface has dropped below the marsh flat, the subsequent flood tide arrives and the water levels begin to rise again.

From Figure 2.12c, we can see that the rate at which the tide recedes is governed by the amount of water that spills over onto the flats. At the mouth, during spring

phase, the higher of the two daily high tides reach levels which are about 20-30 cm higher than the lower-high tides. This results in every other high tide inundating the marsh platform slightly more (Figure 2.12c). When this occurs, there is more separation in the water levels during high tide, followed by more slowly falling tides. This pattern continues until about April 2nd, when neap phase arrives again and the platform in landward areas of the marsh is no longer inundated during high tides.

Finally, from both 2.12b and 2.12c, it is concluded that there is a physical maximum water level that can be reached, within reason (i.e. barring a surge event on the order of > 1 m above typical water levels), based on the elevation of the marsh platform in the immediate vicinity of a particular point in the main channel. There appears to be no influence by the surface elevation at the inlet; rather, the maximum is governed by the local geometry of the marsh.

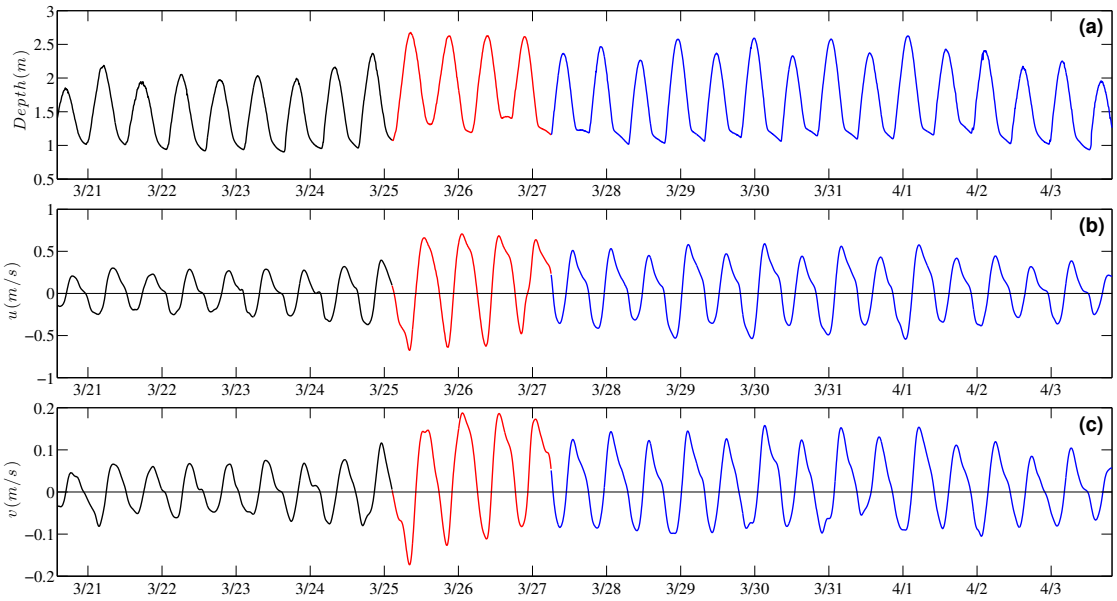

Figure 2.13: (a) Time series of measured depth at the channel mouth; (b) and (c) Time series of measured, depth-averaged, and filtered horizontal velocities in the East (u) and North (v) directions, respectively: (black) before storm event, (red) during storm event, (blue) after storm event.

The three curves in Figure 2.13 are split into three time spans: (1) before the storm, neap phase; (2) during the surge event, March 25^{th}-26^{th} (see Figure 2.10); and

(3) after the storm, spring phase. The distinction between these three time spans is made due to the noticeable difference in several characteristics. Furthermore, the implications of this split are better understood when coupled with the flux through the inlet, as is discussed in the final section of this chapter.

2.5.3 Computing Discharge

As pointed out by Blanton et al., (2002), knowing the relationship between surface elevation and total flux through the inlet can provide insight into the asymmetries present in the marsh. In order to compute discharge, a few assumptions needed to be made. First, the cross-sectional bathymetry of the channel's inlet was measured by traversing a moving-vessel across the mouth several times during a falling tide (Figure 2.14).

Figure 2.14: Deployment of a catamaran vessel at mouth, near Site A, used to measure cross-sectional bathymetry. The picture is oriented in the direction looking towards Delaware Bay. The locations of the measured points are given in Figure 2.9.

There are several things to consider here. First, the cross-sections were mapped during the spring phase, in order to allow for the widest portion of the channel to be mapped. However, the higher of the high tides during this phase were at night, so an

assumption of slight extension of the channel banks must be made. Finally, considering the blanking distance of the device, coupled with the depth of submergence - in all equating to about 30 cm - fully mapping the edges of the channel was inhibited.

Taking all of that into consideration, Figure 2.15 shows the extension of the banks as a linear approximation of the bed, up to mean high water. Based on both survey data and field observations of the high-water debris line on the sandy bank, the width of the channel inlet at MHW is approximated to be 20 meters. The depth of 2.5 meters is prescribed from noting the maximum depths during the spring phase in Figure 2.13a.

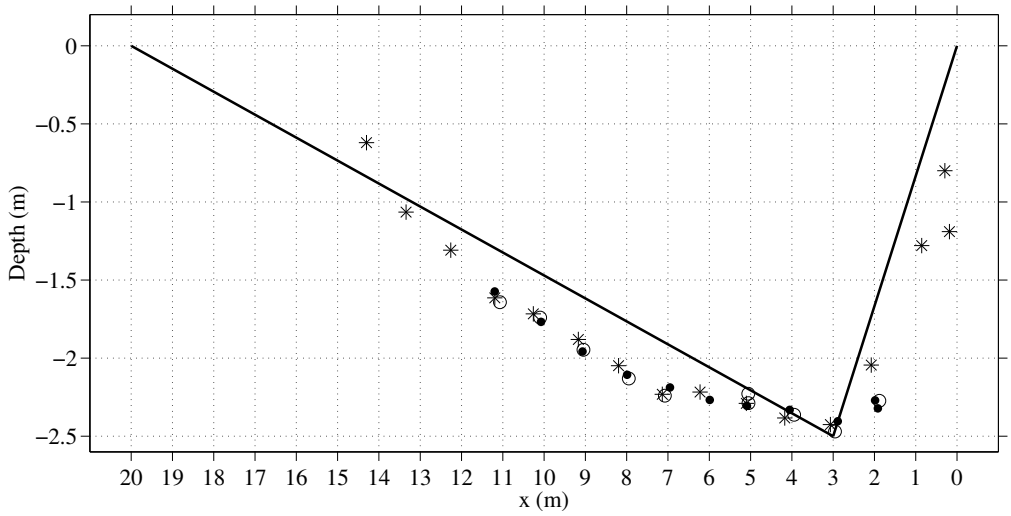

Figure 2.15: Bathymetry of the cross-section measured at the mouth of Brockonbridge Gut, from traversing the inlet three times during a falling tide, as shown in Figure 2.9; (∗) Traversal #1, (•) Traversal #2, (o) Traversal #3. The solid line represents an approximated V-shaped channel, shown in Figure (2.16). Note: for reference, an axis into the page is in the landward direction, whereas an axis normal to the page, in the outward direction, is toward Delaware Bay.

As a reference, the bottom mounted ADCP was deployed near at the cusp of the approximate cross-section in Figure 2.15. We can see from Figure 2.15 that the idealized bedform certainly under predicts the total cross-sectional area, leading to a possible under prediction in total volumetric discharge. However, the assumption of uniform velocity across the channel cross-section is also made, due to lack of spatially

variable velocity profile data. Although this assumption would typically lead to over estimation of total discharge, as velocities near the edges tend to be lower, the under estimation of cross-sectional area serves to counter balance the assumption of cross-sectional uniformity in flow.

The assumptions of a V-shaped channel and uniform velocities across the inlet allow for the total volumetric flux to simply be calculated with

$$Q(t) = \overline{v}(t) \int_0^{b_{MHW}} h(t)dx = \overline{v}(t)A(t) \tag{2.1}$$

where $Q(t)$ is the total volumetric discharge, b_{MHW} is the width of the inlet at Mean High Water (MHW) level, $h(t)$ is the total water depth at $x = 3$ m in Figure 2.15, $A(t)$ is the time-varying cross-sectional area of the channel at the mouth, and $\overline{v}(t)$ is the depth-averaged velocity in the direction of flow which is normal to the cross-section. But with the assumption of uniform velocity across the channel, $\overline{v}(x,t)$ becomes only time dependent. Therefore, $\overline{v}(x,t)$ reduces to just the temporal variation in the depth-averaged axial component of velocity, $\overline{v}(t)$, measured by the ADCP at site A. Positive values of $Q(t)$ represent flooding of the marsh, while negative values represent outflow of water from the marsh.

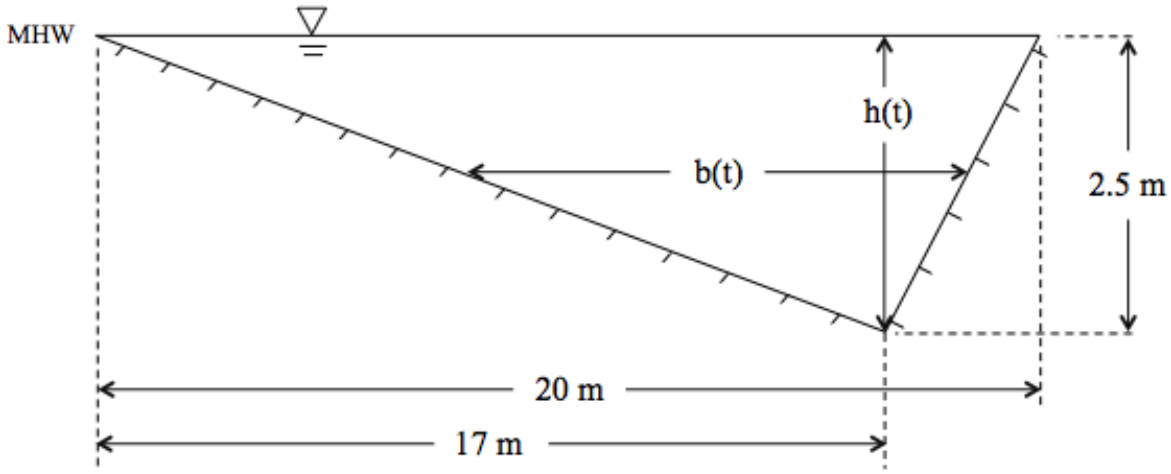

Figure 2.16: Idealization of the cross-section taken at the mouth of Brockonbridge Gut

From Figure 2.16, we can see that the cross-sectional area can be computed by

$$A(t) = \frac{1}{2} b(t) h(t) \tag{2.2}$$

where $b(t)$ is the instantaneous width of the channel and $h(t)$ is the depth of the channel at the location of the cusp. Equation (2.2) can be further reduced to only a function of depth, $h(t)$, by utilizing the known ratios of height and width in Figure 2.16. This is useful since we only have the depth measurements at the cusp from the bottom mounted ADCP deployed at the mouth (Figure 2.13a).

$$A(t) = 4h(t)^2 \tag{2.3}$$

Substituting the cross-sectional area approximation, given by (2.3), into (2.1), gives us the following relationship between water level and volumetric discharge

$$Q(t) = 4\overline{v}(t) h(t)^2 \tag{2.4}$$

Results obtained using (2.4) are shown in Figure 2.17. Total discharge was computed by the addition of the flux in the east and north directions, where the specified velocities for the east and north directions are given in Figure 2.13b and Figure 2.13c, respectively.

As was done in the previous section, the stage-discharge curve in Figure 2.17 is split into three distinct time spans: (1) before the storm, neap phase; (2) during the surge event, March 25^{th}-26^{th} (Figure 2.13); and (3) after the storm, spring phase. First, in general, it seems as though, apart from surge events in the bay, the phase relationship between low tide and zero discharge is similar to that of a standing wave, as can be seen by the cusp on the y-axis of Figure 2.17, in the black and blue curves. However, during the storm event, this phase relationship during low tide shifts to something more in between that of a standing and a progressive wave. There is a clear increase in distortion of the tide with increasing water levels in the marsh, resulting from larger inter-tidal storage capacity.

Before the storm, the tide appears to be represented well by a standing wave in a channel. This is evidenced by the maximums in discharge coinciding with water levels near zero, while the slack waters and flow reversals occur during extremes in surface elevations. This is due to the fact that during the neap phase of the cycle, high tides are rarely, if ever, reaching levels to spill onto the surrounding platforms. Furthermore, the stage-discharge curve exhibits near symmetry during both the ebb and flood stages. It's not until the transition period from neap to spring phase that any distortion of the tide becomes noticeably pronounced.

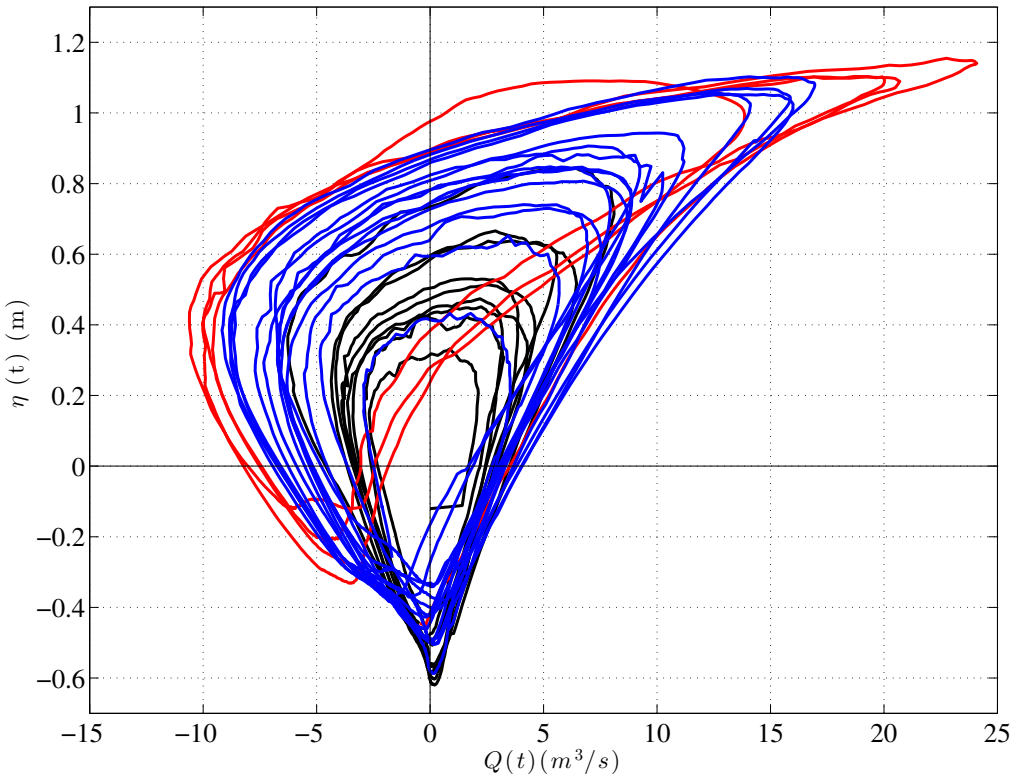

Figure 2.17: Stage-discharge curve for the inlet of Brockonbridge Gut computed by Eq. (2.4), where $\eta(x,t)$ is the surface elevation recorded at Site A by the piezometer in the ADCP. The line colors correspond to depths and velocities given in Figure 2.13: (black) before storm event, (red) during storm event, (blue) after storm event.

The storm causes the most extreme distortion of the stage-discharge curve during the 14-day deployment. The behavior during flood tides is more like what would

be expected for a progressive wave. In this case, the flow reversal doesn't occur during tidal extrema. Instead, it occurs near the middle of the rising tide, around $\eta = 0.2$ meters. As the northeast winds from the storm begin to push water into the marsh, the entire stage-discharge curve undergoes an upward shift. Although the duration of the northeast winds was roughly half a day, or one tidal period (Figure 2.10), both the upward shift and pronounced distortion persist for more than two days. Additionally, the peak positive values for discharge, which represent flux into the marsh, are nearly 25% larger than the maximum flood values during spring tides.

The blue curve in Figure 2.17 provides great insight into how flooding the marsh platform during a normal spring tidal phase, and not a storm surge event, effects the propagation of the tide through the marsh. As the tide begins to rise from low tide, there is not much difference between the spring and neap phases. However, as the water at the mouth rises to levels which cause the marsh platform to get flooded, the curve undergoes a pronounced surge for small increases in η. Consequently, in a similar fashion to the stage-discharge relation during the surge event, peaks in flood flux occur closer to high tide, which is characteristic of a progressive wave. Dronkers (1986) points out that this is caused by an increased gradient in the water surface throughout the marsh. This increased pressure gradient arises as a result of more slowly rising water levels due to the sudden horizontal expanse onto the platform. This behavior is further investigated with a numerical model using idealized marshes in Chapter 5.

Chapter 3

NUMERICAL MODEL NEARCOM

The Nearshore Community Model system, NearCoM, was developed for predicting waves, currents and sediment transport in the nearshore domain (Shi et al., 2013). NearCoM couples the wave model SWAN with a nearshore circulation model, SHORECIRC, as well as a sediment transport model. Since the focus of this study is modeling the hydrodynamics and tidal propagation in a small, channelized tidal marsh at high resolution, the following chapter will not discuss every feature of NearCoM. Rather, only the modules important to the modeling efforts conducted for the present study will be covered. More specifically, the SHORECIRC component (Svendsen et al, 2004) will be covered in extensive detail, as it includes all of the necessary physics and hydrodynamics.

3.1 Background

When SHORECIRC was originally developed, its governing equations were based on a cartesian coordinate system. These equations were solved using a finite difference scheme in which time stepping was treated by the predictor-corrector scheme. Shi et al., (2003) improved upon this version by developing a curvilinear version of SHORECIRC based on a coordinate transformation from cartesian to a generalized curvilinear grid. In addition, SHORECIRC was further improved upon with the implementation of a CFL-free numerical scheme with improved computational efficiency (Shi et al., 2007).

Following Toro (2009), the newest version of SHORECIRC uses a Total Variation Diminishing (TVD-type) hybrid method which combines the finite-volume and finite-difference schemes. As a result, a conservative set of equations were derived for

use with the hybrid TVD scheme. Adaptive time stepping is used, based on the Runge-Kutta method. This is an improvement from the previous version of SHORECIRC, which used an explicit time stepping scheme. For the spatial scheme, a MUSCL reconstruction technique accurate up to fourth order is used in the Riemann solver. The MUSCL-TVD scheme is especially beneficial for modeling tidal propagation through tidal marshes, where sharp elevation gradients could give rise to shocks in the system.

Finally, the coupled version of NearCoM is fully parallelized with MPI, which uses equal CPU load for each processor.

3.2 Governing Equations of SHORECIRC

SHORECIRC is a quasi-3D nearshore circulation model for the prediction of wave-induced nearshore circulation. It is a two-dimensional horizontal (2DH) model which incorporates the mixing effect induced by the vertical variation of wave-induced horizontal circulation. In Putrevu and Svendsen (1999), the instantaneous horizontal velocity in Cartesian coordinates (x_1, x_2) is split as

$$u_\alpha^{ins} = u'_\alpha + u_w^\alpha + u_\alpha + u_1^\alpha \tag{3.1}$$

where $\alpha = 1, 2$, and $u'_\alpha, u_w^\alpha, u_\alpha$ and u_1^α are, respectively, the turbulence component; the wave component; the component of depth-averaged and short-wave-averaged velocity; and the vertical variation of the short-wave-averaged velocity.

Unlike Haas et al. (2003), who use Eulerian averaging, the depth-averaged and short-wave-averaged velocity u_α is defined in the current version of SHORECIRC by Lagrangian averaging as

$$u_\alpha = \frac{1}{H}\overline{\int_{-h}^{\zeta} u_\alpha^{ins}} \tag{3.2}$$

where ζ is the instantaneous surface elevation. The complete SHORECIRC equations can be expressed in Cartesian coordinates (x_1, x_2) as in Svendsen et al. (2004)

$$\frac{\partial \eta}{\partial t} + \frac{\partial H u_\alpha}{\partial x_\alpha} = 0 \tag{3.3}$$

$$\frac{\partial H u_\alpha}{\partial t} + \frac{H u_\alpha u_\beta}{\partial x_\beta} + f_\alpha + gH\frac{\partial \eta}{\partial x_\alpha} + \frac{1}{\rho}\frac{\partial T_{\alpha\beta}}{\partial x_\beta} + \frac{1}{\rho}\frac{\partial S_{\alpha\beta}}{\partial x_\beta} + \frac{\tau_\alpha^b}{\rho} - \frac{\tau_\alpha^s}{\rho} + ROT_\alpha = 0 \quad (3.4)$$

where η represents the wave-averaged surface elevation, and $H = \eta + h$, in which h is still water depth.

In equation (3.4), f_α represents the Coriolis force term which was not considered in the previous SHORECIRC equations (Putrevu and Svendsen, 1999). $T_{\alpha\beta}, S_{\alpha\beta}, \tau_\alpha^s$ and τ_α^b are the depth-integrated Reynolds' stress; the wave-induced radiation stress (Longuet-Higgins and Stewart, 1962 & 1964); and the surface shear stress and the bottom shear stress, respectively. ROT represents the rest of terms associated with 3D dispersion which are not presented here because they do not involve the coordinate transformation to be discussed next. Further details of the 3D dispersion terms can be found in Putrevu and Svendsen (1999).

In this section, we derive a conservative form of the equations in generalized curvilinear coordinates in order to use the TVD numerical scheme. The present approach follows Shi and Sun (1995), who used both Cartesian and contravariant variables in the derivation of the momentum equations. The advantage of using a conservative form versus the contravariant form in Shi et al. (2003) is that a conservative form can be implemented using a hybrid numerical scheme with all forcing terms in vector form in Cartesian coordinates. For example, the radiation stress term $S_{\alpha\beta}$ uses the original form defined in Cartesian coordinates, hence there is no need to make a transformation for the second-order tensor. The disadvantage is that the conservative form of the equations contains both Cartesian and contravariant components. For the hybrid numerical scheme used in the study, it is convenient to solve for the dependent variables using an explicit scheme, rather than the implicit numerical scheme used in Shi et al. (2007).

A curvilinear coordinate transformation is introduced in the general form

$$\xi^1 = \xi^1(x_1, x_2), \qquad \xi^2 = \xi^2(x_1, x_2) \quad (3.5)$$

where (ξ^1, ξ^2) are the curvilinear coordinates. Superscript indices, i.e., $()^\alpha$, are used to represent the contravariant component and subscript indices are used for the Cartesian component of a vector. The relation between the Cartesian component u_α and the contravariant component u^α can be written by definition as

$$u^\alpha = u_\beta L^\alpha_\beta \tag{3.6}$$

where

$$L^\alpha_\beta = \frac{\partial \xi^\alpha}{\partial x_\beta} \tag{3.7}$$

For a strictly Cartesian input grid, the definition for L^α_β in (3.7) reduces to

$$L^\alpha_\beta = \begin{cases} 0, & \alpha = \beta \\ 0.5, & \alpha \neq \beta \end{cases}$$

Using the chain rule, the derivative of a function F with respect to x_α in Cartesian coordinates can be expressed in the curvilinear coordinates ξ^α by

$$\frac{\partial F}{\partial x_\alpha} = L^\beta_\alpha \frac{\partial F}{\partial \xi^\beta} \tag{3.8}$$

Using the metric identity law (Thompson et al., 1985)

$$\frac{\partial}{\partial \xi^\alpha}(J L^\alpha_\beta) \equiv 0 \tag{3.9}$$

where J is the Jacobian matrix and determinant, (3.8) can be rewritten as

$$\frac{\partial F}{\partial x_\alpha} = \frac{1}{J} \frac{\partial F J L^\beta_\alpha}{\partial \xi^\beta} \tag{3.10}$$

Using (3.10), the conservative form of the SHORECIRC equations in curvilinear coordinates can be written as

$$\frac{\partial \eta}{\partial t} + \frac{1}{J} \frac{\partial J P^\alpha}{\partial \xi^\alpha} = 0 \tag{3.11}$$

$$\frac{\partial Hu_\alpha}{\partial t}+\frac{1}{J}\frac{\partial}{\partial \xi^\beta}\left[JP^\beta u_\alpha+\frac{1}{2}g(\eta^2+2\eta h)JL_\alpha^\beta\right]+f_\alpha-g\eta\frac{1}{J}\frac{\partial}{\partial \xi^\beta}(hJL_\alpha^\beta)$$
$$+\frac{1}{\rho}\frac{1}{J}\frac{\partial}{\partial \xi^\gamma}(S_{\alpha\beta}JL_\beta^\gamma)+\frac{1}{J}\frac{\partial}{\partial \xi^\gamma}(\tau_{\alpha\beta}JHL_\beta^\gamma)+\frac{\tau_\alpha^b}{\rho}-\frac{\tau_\alpha^s}{\rho}+ROT_\alpha=0 \qquad (3.12)$$

In (3.11) and (3.12), $P^\alpha = Hu^\alpha$, denotes the contravariant component of volume flux. However, the Coriolis force f_α uses the Cartesian components, (i.e., $-f_cHv, f_cHu$, where f_c is Coriolis parameter), and $S_{\alpha\beta}$ represents the Cartesian component of radiation stress. In the present version, the divergence of radiation stresses (the fifth term of (3.12)) is obtained directly from the wave module SWAN. $\tau_{\alpha\beta}$ represents the Cartesian component of turbulent shear stress, while τ_α^b and τ_α^s are the Cartesian components of bottom stress and wind stress, respectively.

The surface gradient term (the fourth term of (3.4)) is treated following Shi et al., (2011) to obtain well-balanced momentum equations in a MUSCL-TVD scheme of a general order. The expression in curvilinear coordinates can be written as

$$-gHJ\frac{\partial \eta}{\partial x_\alpha}=-\frac{\partial}{\partial \xi^\alpha}\left[\frac{1}{2}g(\eta^2+2\eta h)JL_\beta^\alpha\right]+g\eta\frac{\partial}{\partial \xi^\alpha}(hJL_\beta^\alpha) \qquad (3.13)$$

The wind-induced surface stress in SHORECIRC is computed as (Church and Thornton, 1993):

$$\tau_\alpha^s = C_{dw}\rho_a|\mathbf{W}|W_\alpha \qquad (3.14)$$

where $\mathbf{W}$ is wind speed at a 10 m elevation above the water surface, ρ_a represents air density, C_{dw} is the drag coefficient for wind. Values for C_{dw} are recommended by the WAMDI Group (1988) to be

$$C_{dw}=\begin{cases}1.2875\times10^{-3} & \text{if } W<7.5m/s\\ (0.8+0.065W)\times10^{-3} & \text{if } W\geq 7.5m/s\end{cases}$$

The wave-averaged bottom stress in SHORECIRC includes wave-current interaction, which is written as (Svendsen and Putrevu, 1990)

$$\tau_\alpha^b = C_d \rho u_0 (\beta_1 u_{b\alpha} + \beta_2 U_{w\alpha}). \tag{3.15}$$

where C_d is a constant friction factor (e.g., Jonsson, 1966), $U_{w\alpha}$ is the amplitude of short-wave particle velocity which can be obtained from the wave module SWAN, $u_{b\alpha}$ is the current velocity at the bottom to be discussed in equation (3.18), and u_o is the maximum magnitude of current velocity between the bed velocity, $u_{b\alpha}$, and wave velocity, $U_{w\alpha}$. In this formulation, the shear stress τ_α^b is contributed by the current velocity, $u_{b\alpha}$, with weighting factor β_1 and the wave velocity, $U_{w\alpha}$, with weighting factor β_2. The data from laboratory experiments under monochromatic wave conditions show that β_1 and β_2 are dependent on $U_{w\alpha}/u_{b\alpha}$ and the angle between wave and current vectors (Svendsen and Putrevu, 1990). In the present model version, $\beta_1 = 1.0$, $\beta_2 = 0.5$ (Shi et al., 2011). The friction factor, C_d, can be calculated by using an alternate version of Manning's formula to incorporate the effect of water depth H with a given Manning coefficient, n, taken to be a constant (Manning, 1891). In metric units, which are universally used in this study, Manning's coefficient has the units $[s \cdot m^{-1/3}]$.

$$C_d = \frac{g n^2}{H^{1/3}} \tag{3.16}$$

NearCoM-TVD also provides an alternative option to calculate the bottom stress under wave current interaction based on Soulsby et al. (1993):

$$\tau_\alpha^b = Y(\tau_\alpha^c + \tau_\alpha^w) \tag{3.17}$$

where τ_α^c is the current-only bottom stress, τ_α^w is the wave-only bottom stress and Y can be parameterized by a set of fitting coefficients (Soulsby et al., 1993; Soulsby et al., 1997). The equation governing the vertical structure of horizontal velocity can be solved analytically using the lowest order of the equation for vertical variation of

current:

$$\frac{\partial u_{1\alpha}^{(0)}}{\partial t} - \frac{\partial}{\partial z}\left(\nu_t \frac{\partial u_{1\alpha}^{(0)}}{\partial z}\right) = F_\alpha \tag{3.18}$$

where ν_t is the eddy viscosity and F_α is a general form of the local forcing (see equation (31) in Putrevu and Svendsen, 1999 for details). The solution of depth variant current velocity u_1^α adopted here is the same as that discussed in Shi et al., (2003). The bottom current velocity u_b^α can be evaluated using u_α and u_1^α at $z = -h$:

$$u_b^\alpha = u_\alpha + u_1^\alpha|_{z=-h} \tag{3.19}$$

For a detailed description of the numerical schemes employed in NearCoM; the governing equations for SWAN and the sediment modules; and more information regarding parallelization; the reader is referred to Shi et al., (2013) and Chen et al., (2014).

3.3 Specification of Boundary and Initial Conditions

There are several ways in which boundary conditions can be specified in the SHORECIRC module of NearCoM. The many options are given in Shi et al., (2013); however, only the applications which are relevant to this study will be listed here.

The boundary conditions can be coupled with surface elevation data specified at the open boundaries. In this application, there is no requirement to supply any information about the velocities at the boundary. Rather, with this coupling method, the resulting velocities due to a surface gradient between the boundary cell and its neighboring cells are used for the coupled boundary conditions. This is convenient because it doesn't require any previous knowledge about the velocities at any boundaries; just the time variation in the surface elevation.

The downside to this coupling method is that shocks near the boundary can generate large surface gradients, which propagate to the open boundary. The result is artificially large velocities at the open boundaries. A solution to this problem is to

ensure the boundary is far enough away from any sudden shifts in elevation and any kinks in the bathymetry.

NearCoM also allows for initial conditions to be specified. Initial values for the u and v velocities, as well as initial values for η can be specified as input grids, which must be the same size as the model domain.

3.4 Important SHORECIRC Parameters

There are many parameters that can be defined in NearCoM, but again, only the important ones for this study will be discussed here. The first of these parameters is the Froude number cap. An upper limit on the Froude number can be defined to limit spurious velocities from propagating throughout the domain. By limiting the value of the Froude number

$$Fr = \frac{u_{i,j}}{\sqrt{gH_{i,j}}} \tag{3.20}$$

to a maximum value, values of $u_{i,j}$ which cause the Froude cap to be exceeded are replaced by

$$u_{i,j} = Fr_{cap}\sqrt{gH_{i,j}} \tag{3.21}$$

where, as previously mentioned, H is the total water depth and is represented by $H = h + \eta$. It is suggested that a value of 0.8 be used for Fr_{cap} in shallow areas, which is the case in the transitional phase of the flow from the BG onto the marsh platform.

The second important parameter is the minimum depth for wetting and drying. If the total water depth of a cell has exceeded the minimum depth, the cell will be stored as wet. This check is repeated explicitly at each time step.

The Courant-Friedrichs-Lewey (CFL) criterion is used in NearCoM's adaptive time-stepping scheme.

$$\Delta t = C\min\left(\min\frac{\Delta x}{|u_{i,j}| + \sqrt{gH_{i,j}}}, \min\frac{\Delta y}{|v_{i,j}| + \sqrt{gH_{i,j}}}\right) \tag{3.22}$$

where C is the Courant number. In this study, a Courant number of 0.5 is always

used. As a result of a small grid size and depths exceeding 5 meters in this study, Δt is typically very small, $O(10^{-1})$ seconds.

Finally, in domains with sharp gradients in elevation and bathymetry, potentially causing the total water depth in neighboring cells to be very different, the friction factor, C_d becomes very important. From (3.16), we can see that the friction is strongly dependent on the total water depth, given a constant Manning number. Figure 3.1 illustrates the variability of this relationship, which is shown by a linear relationship in log-log scale.

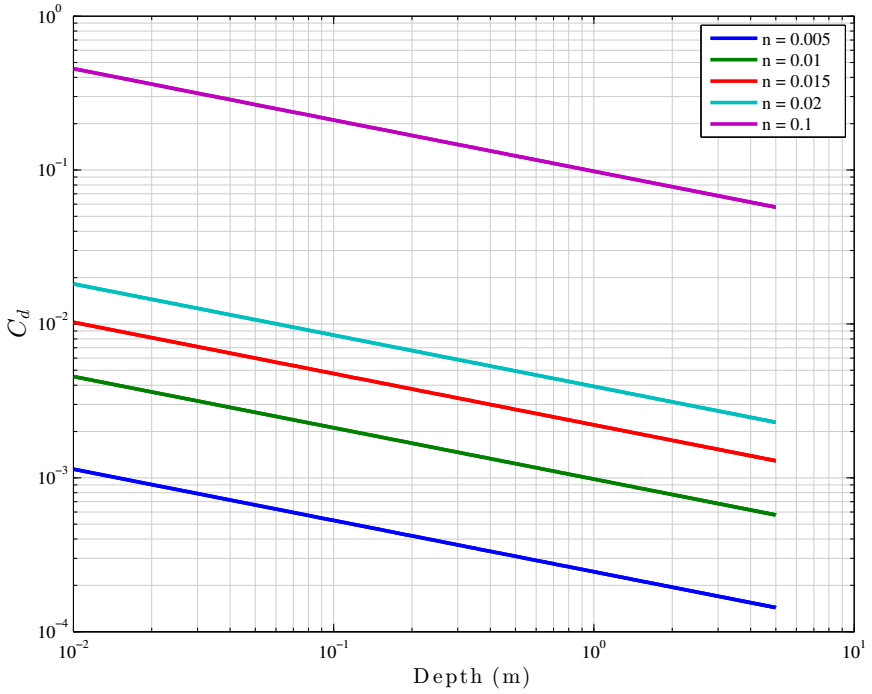

Figure 3.1: The effect of variable water depths on the drag coefficient, used in computing bottom stress in Eq. (3.15), for several different Manning numbers

3.5 Computational Environment

Modeling work was carried out using the Mills HPC Community Cluster, managed by Information Technologies at the University of Delaware. Mills consists of 200

SMP compute nodes with 5,136 cores in total. The Linux based cluster uses Scientific Linux 6 as its operating system.

Chapter 4

MODEL VALIDATION FOR A DELAWARE BAY SALT MARSH

4.1 Introduction

This chapter details the process of validating the hydrodynamics of the numerical model used for this study, NearCoM. Two different model domains were used during this process, each with respective advantages and disadvantages. First, a summary of the simulations with the smaller domain is given, including the reasons behind the choice of using a smaller domain, and how they compare to the field data. Then we discuss the model parameters that were used and the application of boundary conditions. This is followed by a discussion of the results pertaining to this domain. Next, a brief description of the reasons for choosing to expand the domain is provided. Again, the model setup of boundary conditions and parameters will be laid out. Finally, comparisons are made between field measurements (Chapter 2) and model computed results, and the differences between results from using the small versus large domain are presented.

4.2 Small Model Domain

4.2.1 Creating the Model Grid

In the first phase of model validation, a high-resolution Digital Elevation Model (DEM) was used as the domain. This DEM was constructed using LiDAR data which were collected by the United States Geological Survey (USGS) (Nardi, 2009). The plane that was outfitted with the LiDAR device flew over the marsh at the predicted low tide, thus allowing for the most elevation measurements to be made without the hindrance of water, since LiDAR doesn't penetrate water. Additionally, the LiDAR

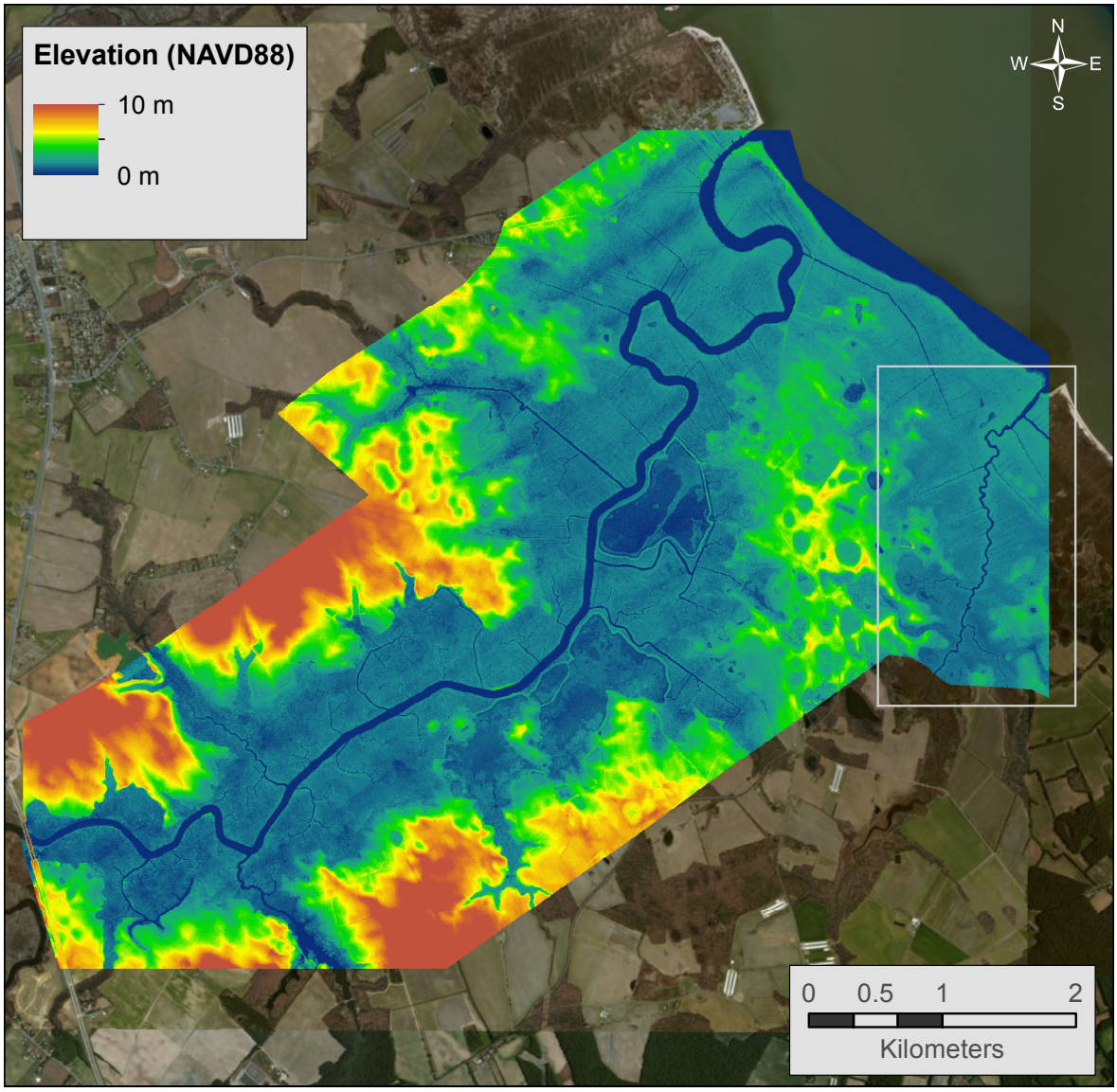

Figure 4.1: DEM of the USGS LiDAR dataset collected in 2009. The larger marsh to the left is the Murderkill Estuary. The coverage area of Brockonbridge Marsh is outlined with a gray box. Delaware Bay is the body of water in the northeast corner of the image. (*Satellite imagery courtesy of ESRI*)

data were measured specifically for the Murderkill and Brockonbridge Marshes. These factors all considered made this DEM the best available dataset for the BM.

However, one slight issue became apparent; the coverage of Brockonbridge Marsh was somewhat limited. Essentially, no elevation data was available east of the mouth, nor was there any coverage more than about two kilometers south of the inlet. But since the quality of the DEM was so much better than statewide datasets, the decision was made to accept the costs of not modeling the entire domain. The northern end of coverage ended around the mouth, which was where the ADCP was deployed at Site A. Furthermore, all sites A-F were contained within the small domain. Therefore, the north, east and south boundaries were governed by the edges in coverage area of the DEM, as shown in Figure 4.1. The west boundary was then determined based on forcing the size of the domain to be 500 x 1000 (Figure 4.2). Forcing the domain to be this size made it easy to use multiple processor configurations during computation.

The data from the bathymetric surveys conducted in the summer of 2013 (Figure 2.8) were interpolated onto the grid to create a topo-bathy DEM, with a resolution of 2 meters (Figure 4.3).

Although the DEM was adjusted for an overall bias of 5 cm (Nardi, 2009), the presence of vegetation introduces a local bias into the data. A study conducted in the neighboring Murderkill Estuary by McKenna (2009) determined there was an additional +15 cm bias in the data as a result of vegetation. There are also seasonal variations in vegetation height, but these were not considered here as this information was not available. A high-resolution map of a small area in the western region of Brockonbridge Marsh was created from detailed surveys (Puleo, J. A., Pieterse, A. and McKenna, T. M.) (Figure 4.4a). Since the elevations in this high-resolution map represented the true marsh platform, it was used to verify the +15 cm bias in the 2 m DEM. Figure 4.4b demonstrates the existence of vegetation bias on the marsh surface (red colors) when compared with platform elevations of 4.4a (yellow colors), whereas the mudflat in 4.4a and 4.4b (blue colors) both show similar elevations. Finally, when Figure 4.4c, which has 15 cm subtracted from areas with vegetation, is compared

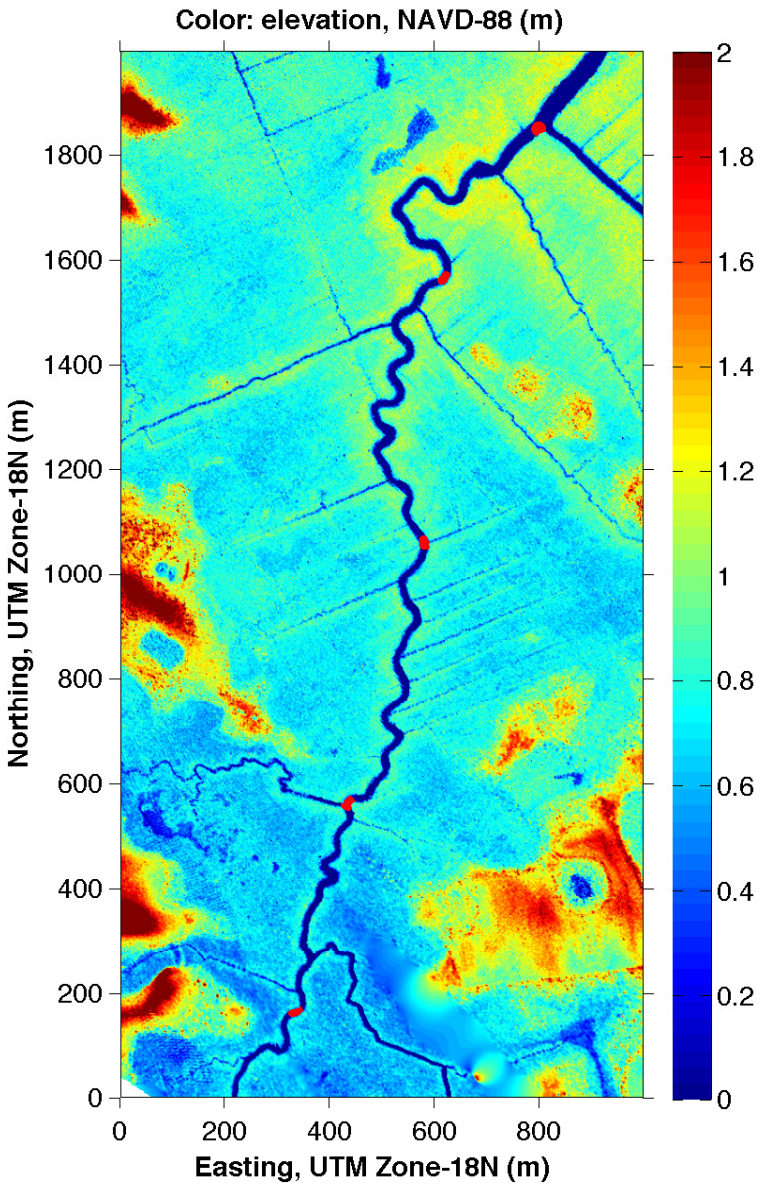

Figure 4.2: DEM of the smaller model domain used in phase one of model validation. Red dots denote the locations of Site B-F. The easting and northing values given are relative distances from the southwest corner of the domain.

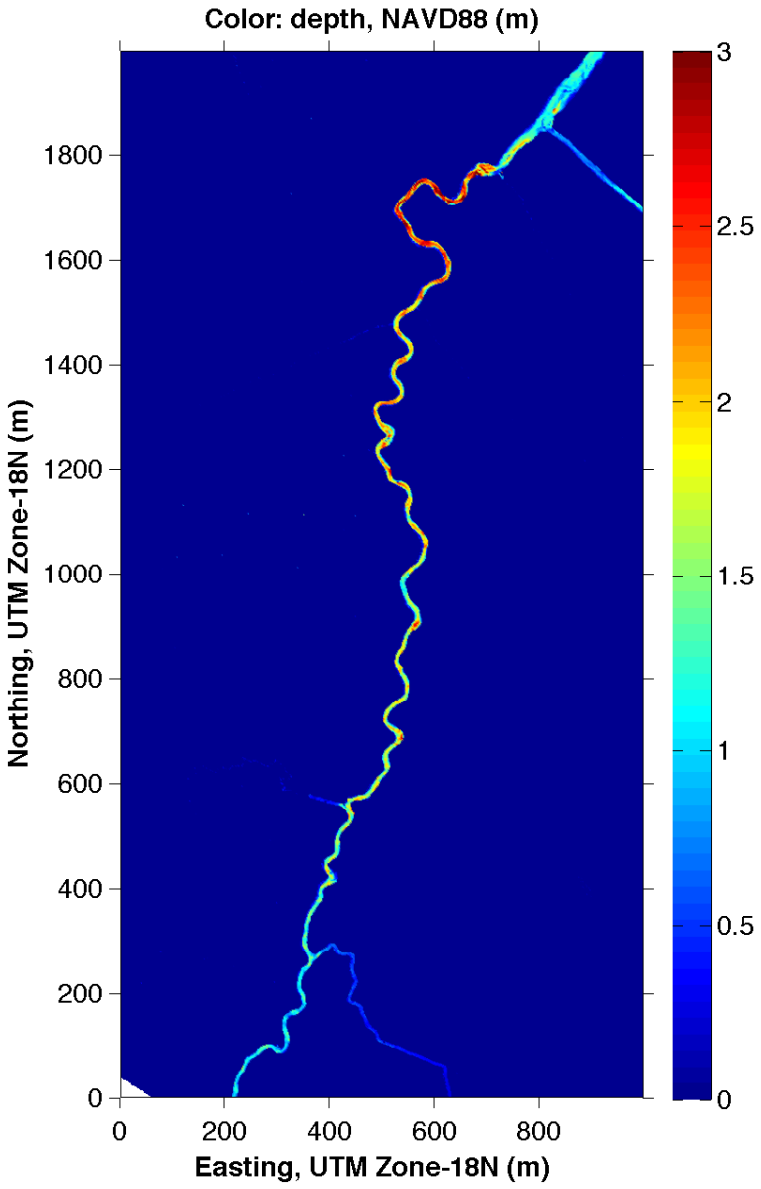

Figure 4.3: Depth of channels measured during the surveys, interpolated onto the grid shown in Figure 4.2. The easting and northing values given are relative distances from the southwest corner of the domain.

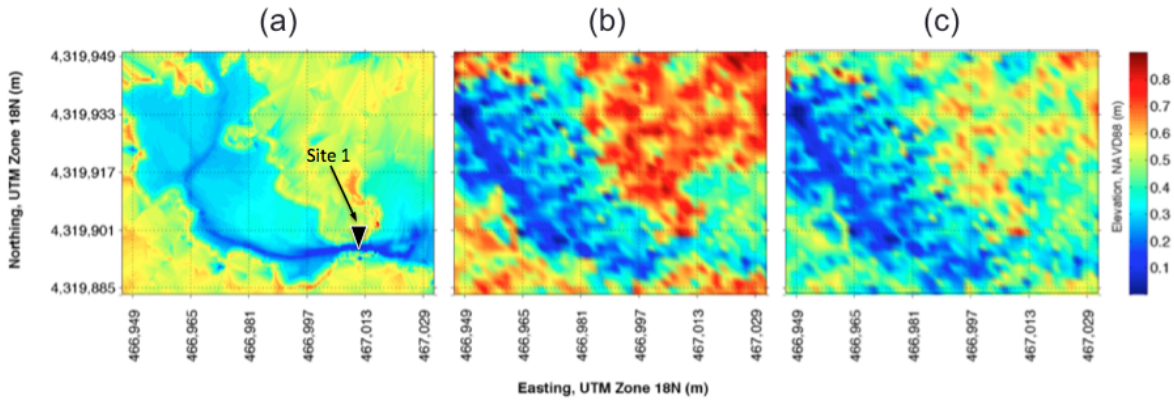

Figure 4.4: Illustration of the correction for vegetation bias in a selected area from the original DEM. (a) High-resolution DEM; (b) Original 2 m resolution DEM; (c) Original 2 m resolution DEM with corrections applied for vegetation bias. A pressure gauge at Site 1 is labeled with a black triangle.

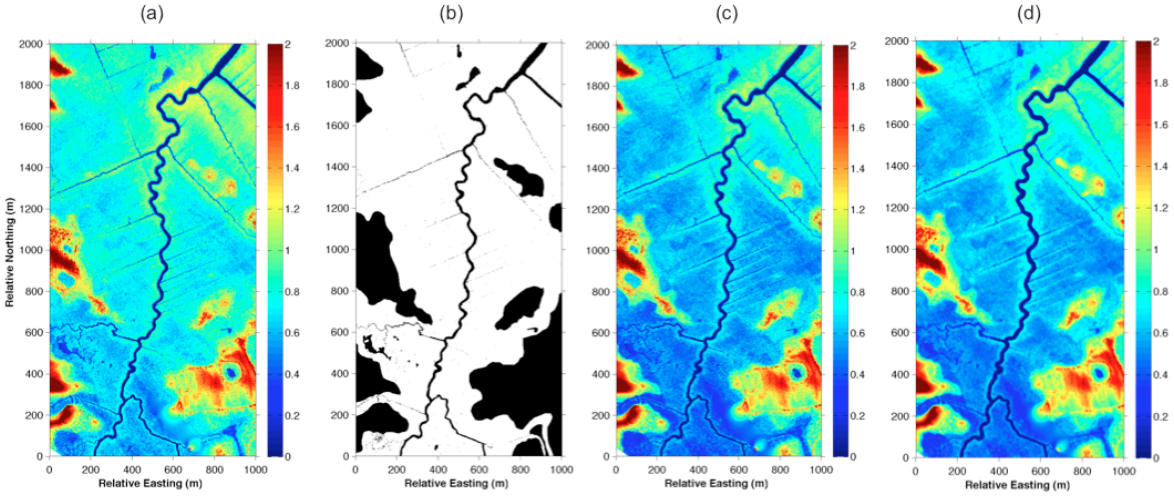

Figure 4.5: Depiction of adjustments applied to the original DEM. (a) Original DEM; (b) Black areas represent a mask for channels, mudflats and high-elevation areas where there is no presence of vegetation bias, so no corrections were applied; (c) Original DEM less the 15 cm bias in vegetated areas; (d) Final DEM, after passing a moving-window filter across the domain 4 times, to smooth out the noise.

with the high-resolution DEM in 4.4a, the agreement between the two is much better. However, comparing them also demonstrates the limitations of using a 2 m DEM, as it becomes obvious that even though a 2 m resolution is considered to be high-resolution on a larger scale, it still fails to resolve many subgrid features which may be important. The topic is worth mentioning but is outside the scope of this present manuscript. However, it is also apparent from Figure 4.4 that controlled, LiDAR based DEMs can be extremely accurate, to the degree for which their resolution allows.

The results of Figure 4.4 show that locations such as channels, mudflats and upland areas are not affected by the bias, but regions highly vegetated by *Spartina* grass need to be adjusted. Figure 4.5b outlines the difference between these two areas, where the vegetated regions are shown in white. Figure 4.5c shows the DEM after 15 cm has been subtracted from the white areas in Figure 4.5b.

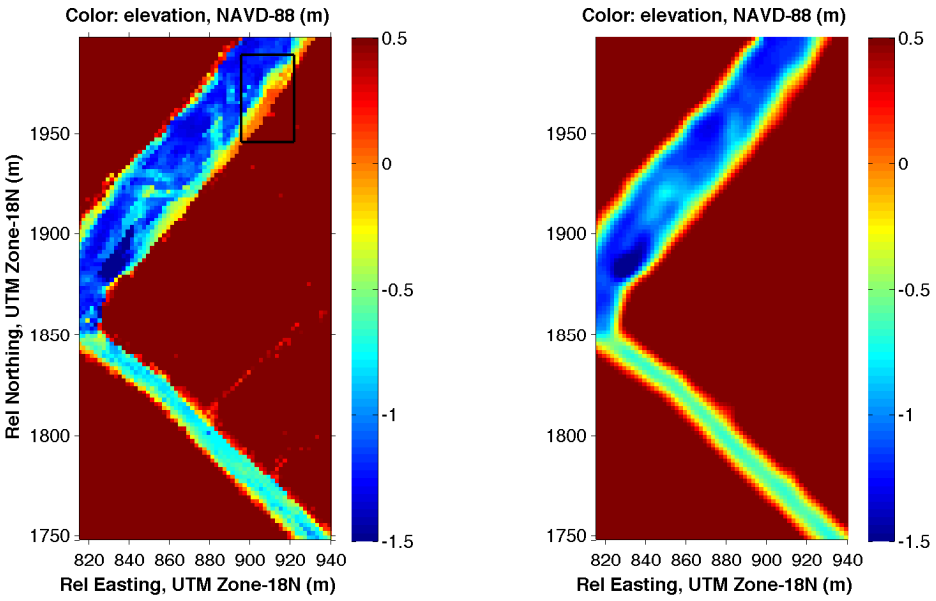

Figure 4.6: Comparison between the north boundary at the mouth of two DEMs which have both been adjusted for vegetation bias, (left) before smoothing and (right) after smoothing. The black box in the left panel depicts a bulge which was successfully smoothed out.

Finally, the DEM appeared to have some noisy areas (see Figure 4.4b & 4.4c). Furthermore, some bulges near the north boundary were present (left panel in Figure

4.6). This had potential to cause problems since the velocities used to force the open boundaries are computed from the gradient between neighboring cells. If a large shock occurs as a result of any bulge near the boundary, the shock will propagate back towards the boundary, causing the velocities to possibly flip from flood to ebb, which is not realistic. Therefore, a moving-window filter was used to smooth out the domain. For each pass with the moving-window, the value of a grid cell is computed by taking the average of itself and the eight cells surrounding it. This nine-cell moving-window technique serves to smooth out the grid without compromising the high-resolution nature of the DEM. The number of necessary passes was determined by how many were needed to sufficiently smooth the bulges and create a bathymetry near the boundary with smooth transitions. This was successfully achieved after four passes. Figure 4.6 shows the result of removing the bulge after four passes with the filter. In addition, Figure 4.7 shows the final DEM which was used in the model of the first phase.

4.2.2 Model Setup

As shown in Figure 4.8, the north end of BG is cut off where the channel opens to the bay, near the location of Site A. This was specifically done so that the water levels recorded by the ADCP at Site A could be used to impose the boundary condition for the model (Figure 4.9). The points at which to apply the coupled boundary condition were selected based on their elevation being lower than the lowest value in the forcing condition. These points will thus always be wet. From Figure 4.9, we can see this value is between -0.5 and -0.6 m. Therefore, the boundary condition was applied to all grid points on the open boundary that are lower than -0.6 m, NAVD88. The measured data at Site A was cut to begin at March 20^{th}, 2013 14:03 since the surface elevation was zero at that time. The whole domain begins uniformly with zero elevation, so there is a lag in the beginning, further into the channel, before there is any adjustment in water level.

For both the small and large domains, the following assumptions are made for every simulation:

1. There is no freshwater input into the system (any rainfall is neglected).

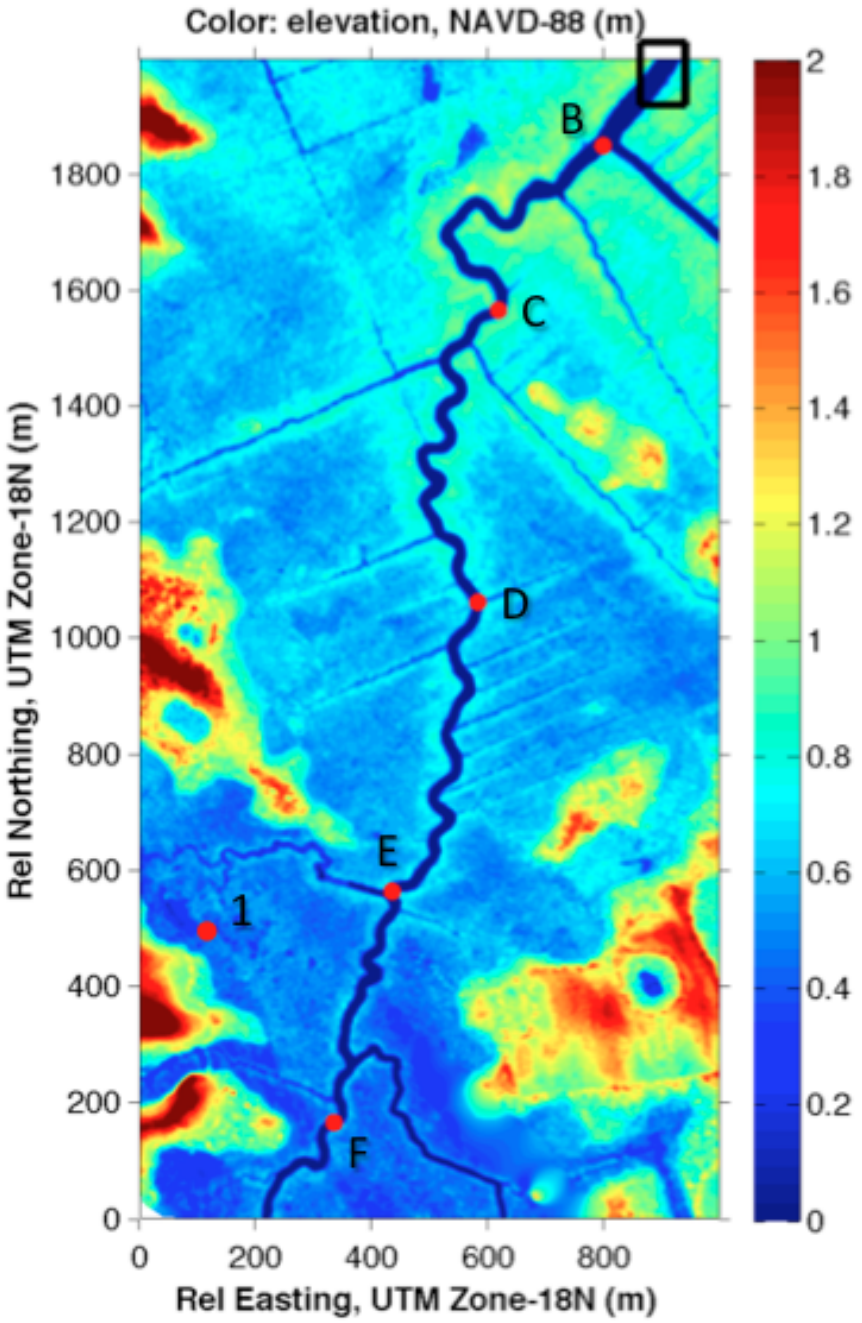

Figure 4.7: Final DEM grid, demonstrating the results of adjustment for vegetation bias and smoothing. The black box in the upper right of the domain outlines where the boundary conditions are applied, as described in Figure 4.8. The locations of the pressure gauges are shown as red dots and labeled accordingly.

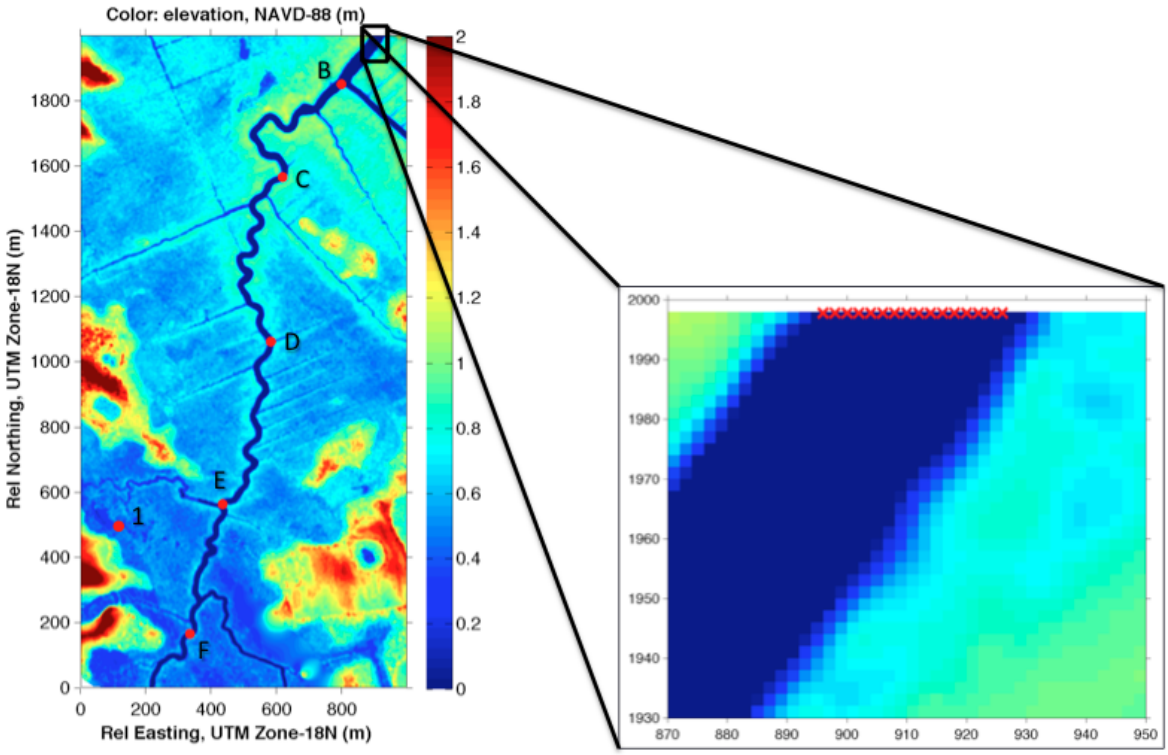

Figure 4.8: Visualization of the grid points at which the boundary conditions were imposed, marked with a red (**x**). Sites B-F and Site 1 are marked with red dots and labeled accordingly.

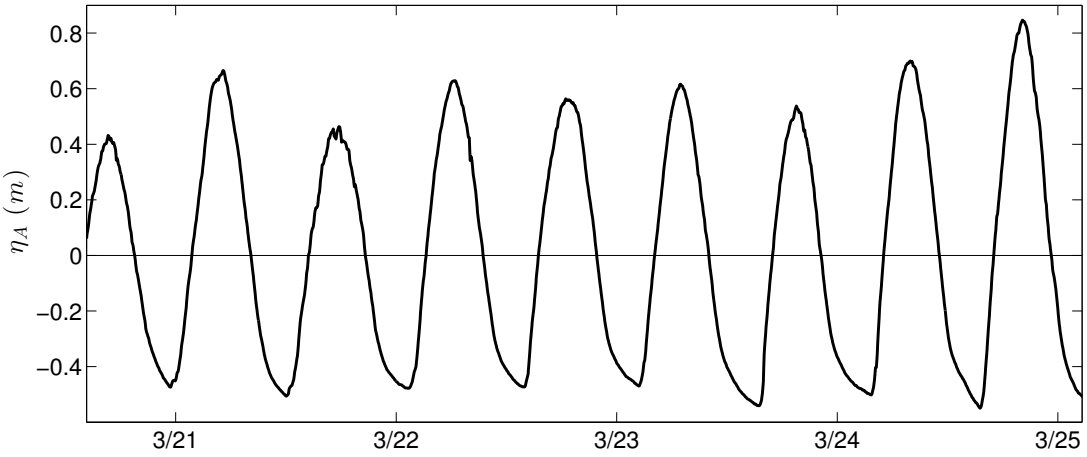

Figure 4.9: Time series of the boundary condition which was imposed at the open boundary grid points of the small domain, which are marked with a red (**x**) in Figure 4.8.

2. The marsh is completely saturated, so there is no flux of water through the bed.
3. The bed is stationary. There is no erosion, accretion or deposition.
4. There are no external inputs or forcing mechanisms into the system, outside of the coupled boundary condition.
5. The marsh is well-mixed. Effects of salinity variations are not included.
6. Surface waves do not propagate through the inlet, thus are not considered in the model runs.
7. Variations in barometric pressure are not considered; however, they are removed from the measured pressure data.
8. Wind stress is not included in the results presented in this manuscript.

Wind stress was considered in several runs but had no significant effect on the modulation of water levels or discharge. Since the boundary is forced with measured water levels that were a response to the in-situ wind conditions, the wind can be considered to be implicitly included in the simulations.

Presently, there is no explicit vegetation component in NearCoM. In order to account for the heightened flow resistance on the marsh platform during the beginning stages of flooding and later stages of ebb, a constant Manning number is used. As a result, for small depths, drag is increased by up to an order of magnitude (Figure 3.1), serving to resist the flow, as would be the case if vegetation were present. A Manning friction factor of $n = 0.02$ is used in the simulations for the results which are shown in the following section.

Due to such fine grid resolution, which contributes to small time steps in the time domain as a consequence of the CFL criterion (Eq. 3.22), each simulation was conducted in a parallel environment using 800 cores. A speedup analysis was carried out, with several configurations of processor cores. It was determined that the cost of increased cross-core communication between 800 processors did not outweigh the increased computational speed. Furthermore, a benchmark test was completed to test NearCoM's ability to numerically handle domains like that of Brockonbridge

Marsh. The results of the test demonstrated that NearCoM was well equipped for high-resolution, slowly-varying domains, with a skill value of 0.9999 (see Appendix).

4.2.3 Results and Discussion

Tidal elevations computed by the model are compared with those recorded by pressure gauges at Sites B-F and data at Site 1, which were recorded through the collaboration with Puleo and Pieterse (CACR). Sites B-F are all located in various locations throughout the main channel, Brockonbridge Gut (BG), while the gauge at Site 1 is located in a narrow channel that's roughly 2 m wide and with channel walls only about 40 cm tall. The bed elevation at Site 1 is +15 cm, NAVD88, so is usually only flooded during high tides. The channel in which the Site 1 gauge is located is a branch off of a connecting channel to the BG, which opens to the BG near Site E (see Figure 4.7). Finally, it's worth noting that the channel at Site 1 is a conduit for flow entering a mudflat, which is depicted in Figure 4.4a.

Several simulations were carried out, with the best results obtained using the parameters described in the previous section. In all cases, the limitation of the small domain was revealed during the time of the storm (Figure 4.10). During the storm, the smaller domain lacked the ability to represent an appropriate inter-tidal storage volume, causing the water levels to surge upward near the mouth (Figure 4.11). This resulted in unrealistically large volumes of flux across the open boundary (Figure 4.12). Therefore, only model results up to the arrival of the storm will be further discussed in the rest of this section.

Figure 4.13 demonstrates that the smaller domain does well to compute water levels accurately, so long as water does not spill over the banks of the channel near the mouth, as pictured in Figure 4.11a. Another shortcoming of the smaller domain is revealed with Figure 4.13g. As best seen in Figure 4.4c, the small scale geometric features in the areas surrounding Site 1 are not well represented by a 2 m resolution grid. The consequence is seen by the model's inability to drain effectively. The water levels drop to about 0.5 meters, where it remains until the ensuing high tide. This

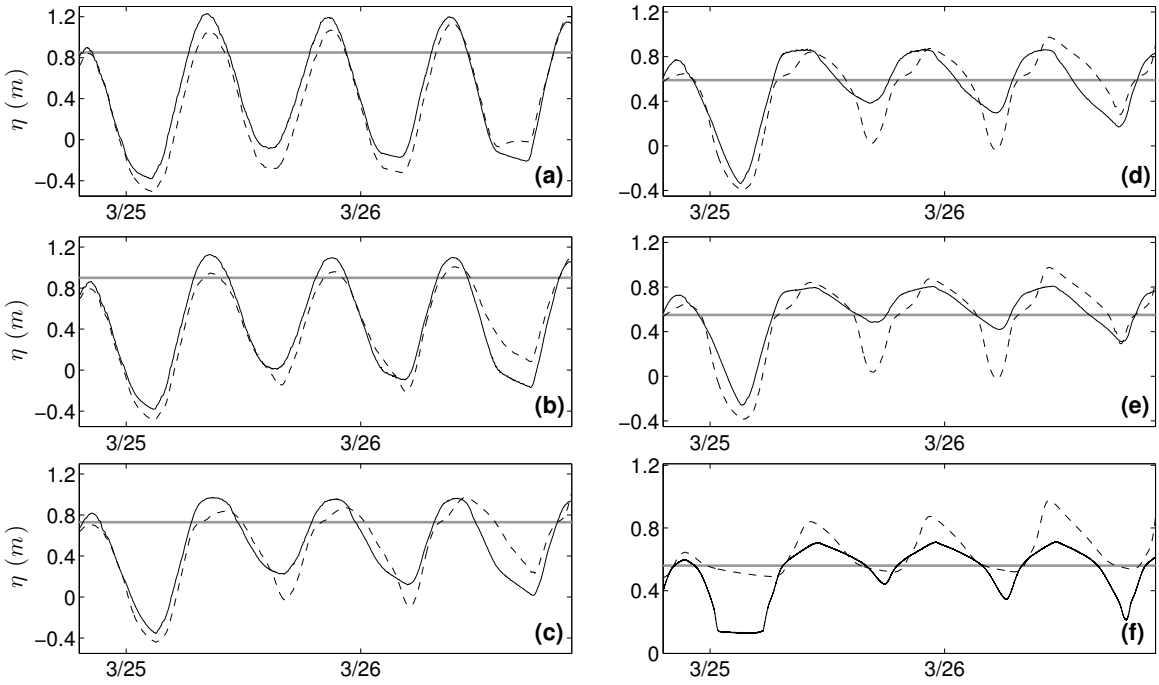

Figure 4.10: Model results for $\eta(t)$ vs field measurements, during the storm, for Sites B-F, and Site 1 as labeled in Figure 4.8; (a) Site B, (b) Site C, (c) Site D, (d) Site E, (e) Site F, (f) Site 1. The horizontal gray line marks the approximate marsh platform elevation at each site. — Field Data, - - Model Results

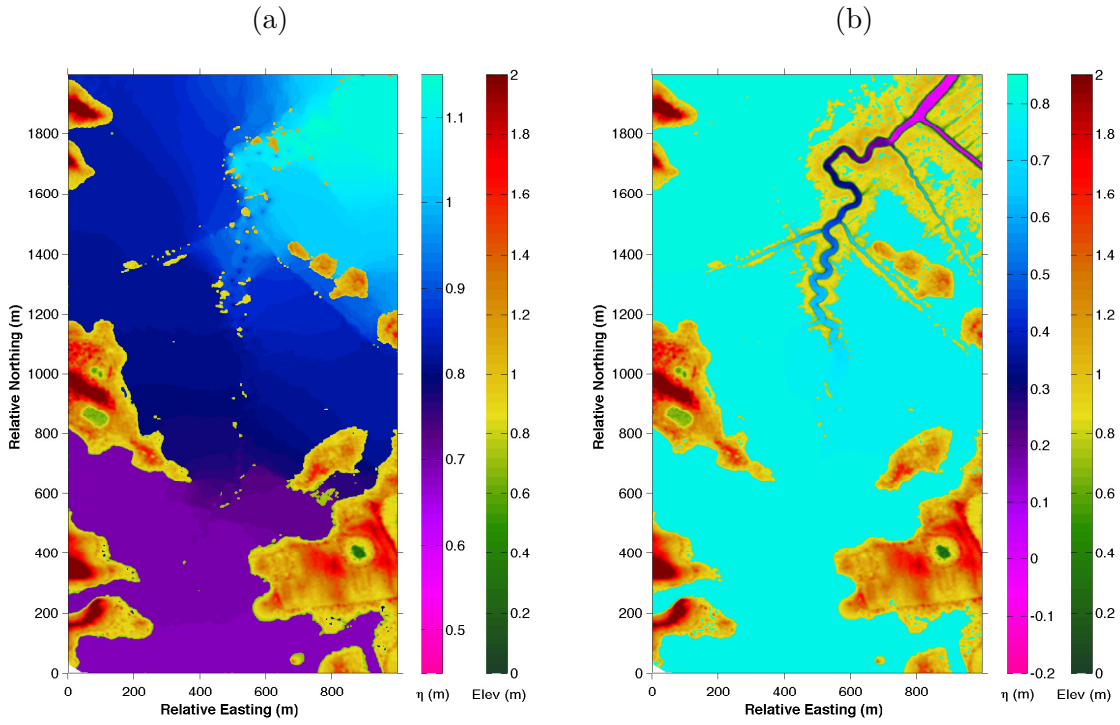

Figure 4.11: Instantaneous surface plots of computed $\eta(t)$ across the small domain, during the storm. (a) March 26^{th} 09:15, near high tide at mouth; (b) 4.5 hours later, March 26^{th} 13:45, during falling tide. Note the difference in scales for the color of η between the two plots.

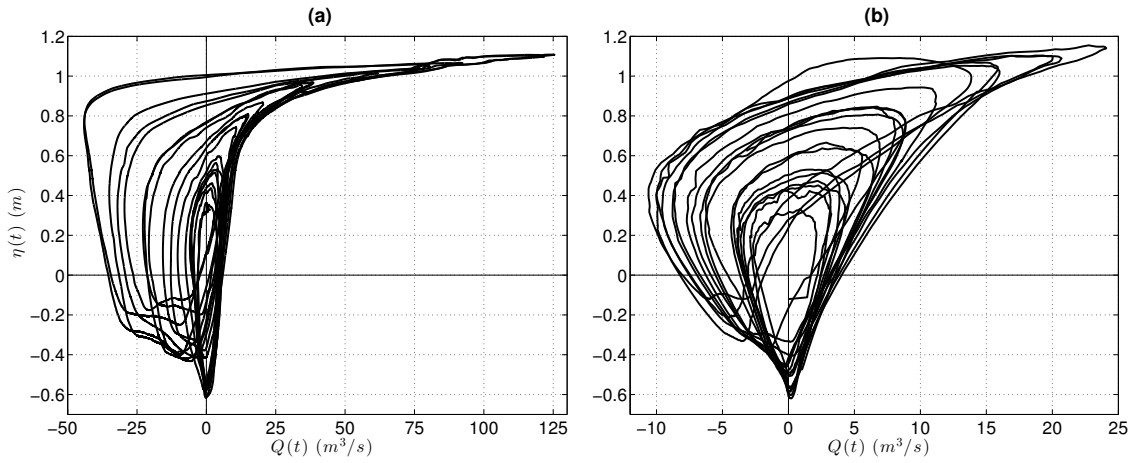

Figure 4.12: Stage vs discharge curves for (a) Model results and (b) Field data, between the dates of March 21, 2013 14:00 and March 30, 2013 13:15, which include the storm, for the mouth of Brockonbridge Marsh. Note the difference in scales for the x-axis.

is likely due to disconnects in the secondary and tertiary levels of channel networks, functioning as a sort of dam for the water, which essentially remains ponded on the marsh surface. Further care is taken in the following section to manually remove these "dam-like" features from narrow channels that branch from the Brockonbridge Gut.

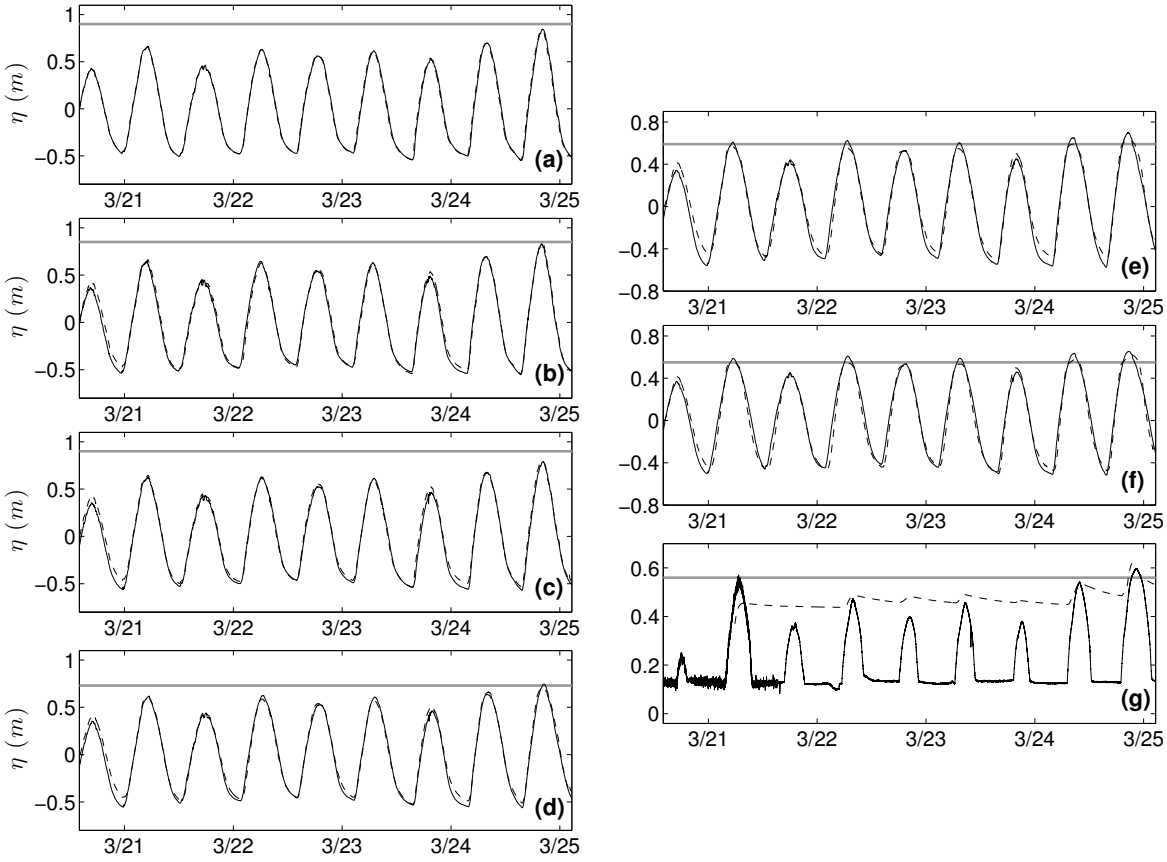

Figure 4.13: Model results for $\eta(t)$ vs field measurements, before the storm, for the open boundary, Sites B-F, and Site 1 as labeled in Figure 4.8; (a) North Boundary, (b) Site B, (c) Site C, (d) Site D, (e) Site E, (f) Site F, (g) Site 1. The horizontal gray line marks the approximate marsh platform elevation at each site. The bed elevation of Site 1 in panel (g) is 15 cm, so the channel goes dry for several hours each time the tide flows out, with the exception of the presence of the storm. Note the slight difference in the scales of the y-axis between the left and right panels. — Field Data, - - Model Results

In addition to accurately computing water levels throughout the main channel, we compare stage-discharge relationships between the field data and model results. Drawing from Figure 4.14, we note similar curves for both the model results and field

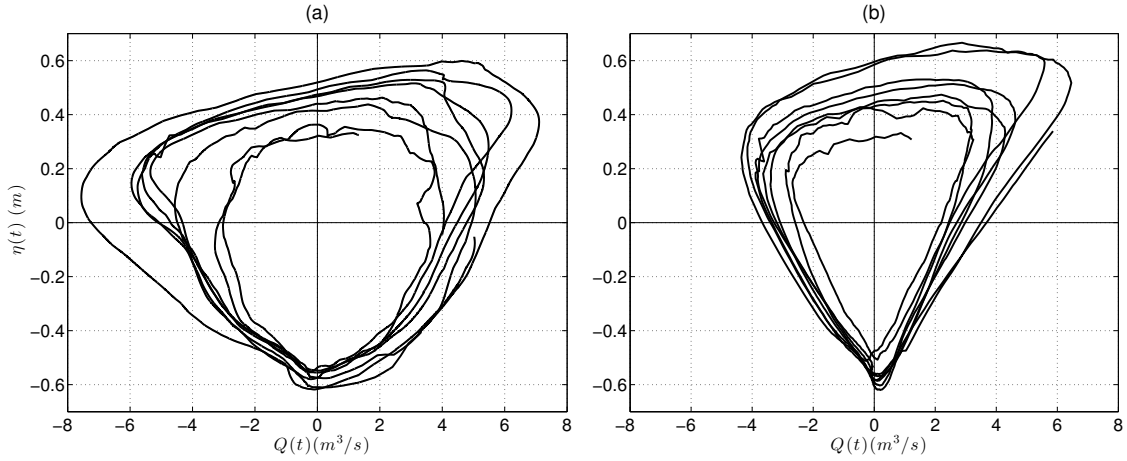

Figure 4.14: Stage vs discharge curves for (a) Model results and (b) Field data, between the dates of March 21, 2013 00:00 and March 25, 2013 04:00, for the mouth of Brockonbridge Marsh.

measurements. The curve in Figure 4.14a was obtained by substituting the model computed velocities into Equation (2.4). The water levels of slack water coincide at nearly identical times for both the model and field results. However, slightly before and after low-tide slack waters, the field data exhibit a more gradual shift from ebb to flood. When compared to the field data, the model tends to over predict the magnitude of flood flux in the first couple of hours after low-water slack. Consequently, the model also expresses a tendency to over predict the maximum magnitude of the ebbward discharge. The overestimation becomes increasingly larger for higher water levels (Figure 4.12).

Conversely, the model and field data agree fairly well regarding the timing and magnitude of maximum inward flux. Furthermore, as the direction of flux switches from flood to ebb, the slopes of the curves in Figure 4.14 exhibit similar declines. Overall, the model results tend to agree with the field measurements much better for higher water levels. Their agreement diverges as the tide starts to drop below zero. This is likely attributable to an oversimplification of friction in the model. However, the model reasonably reproduces the general trend of the stage-discharge relationship observed in the field.

The enhanced ebbward jet computed by the model, especially for the higher

water levels, can possibly be explained as a consequence of the small domain. Since flow across the boundaries of the domain is prohibited, with the exception of the open boundary at the mouth, there is a large setup of water in the domain. When the water level drops at the mouth, a large pressure gradient arises, where water levels differ by almost 1 m over a distance of only 1 km (Figure 4.11b). Since velocities at the open boundary are computed based on the pressure gradient, the large surface gradient can generate large velocities through the mouth, causing the computed discharge values to be excessively high (Figure 4.12a). The presence of the large pressure gradient is clearly seen in Figure 4.11. Excessive amounts of water are stored in the surrounding flats, as evidenced by Figure 4.11a. The resulting gradient in the water surface serves to drive the flow out of the domain, causing the water levels in the channel to drop significantly (Figure 4.10), accompanied by an enhanced volume of flux. This is a consequence of forcing the domain at the inlet, instead of using an expanded domain where the forcing conditions are applied at an offshore boundary.

4.3 Large Model Domain

The small domain used in model runs discussed in the previous section demonstrated that, although it was an oversimplification of the entire system, water levels that remained in the main channel could be computed with reasonable accuracy. However, as the model reached the point of the storm in the boundary condition, the pressure gradient became so large that the results were no longer acceptable (Figures 4.10 and 4.11). The flux into and out of the system during the storm was up to an order of magnitude larger than the field data (Figure 4.12). In addition, the multi-day setup of water observed in the field data (Figure 2.12b) was not repeated accurately by the model in the days following the storm. Due to the large pressure gradient forcing water out of the domain, water levels throughout the marsh dropped well below measured values during low tides in the days following the storm event (Figure 4.10).

In the following section, a brief discussion of the new, larger domain is given. This is followed by an outline of the parameters and boundary conditions used for the

model. Finally, the results of the model simulation are presented.

4.3.1 Model Setup

Since it was shown in the previous section that the smaller domain could adequately reproduce the observed water levels in the field prior to the storm, the focus of this section will be on modeling the surge event and the days following. In order to more accurately model the response to a surge event, the domain is extended to include nearly the entire floodable surface of Brockonbridge Marsh. Consequently, the open boundary was shifted to be located in Delaware Bay.

The creation of the extended domain was a very complex process which involved merging multiple DEMs from three different sources, with different spatial resolutions in different coordinate systems. There were many issues involved in creating the new topo-bathy grid. A full, detailed description of the procedure carried out in creating the DEM, as well as general issues that arise when merging DEMs from difference sources, is given in Mieras et al., (2014). However, a few important points are mentioned below.

When creating the DEM, care was taken to ensure there were no disconnects in the large secondary and tertiary channels. Furthermore, the mosquito channels near the coastal region of the marsh were manually "burned" into the domain. Finally, as can be seen at about 1000 meters north and 750 meters east of the lower-left corner of the DEM in Figure 4.15, a bridge passes over the marsh. The channel flows freely under the bridge, but on either side of the channel, the flow is restricted by the higher elevated road. In the DEM, the bridge over the channel was manually removed, and its values were replaced with similar values to the channel's depth in the adjacent areas.

Since LiDAR cannot penetrate through water, there was no coverage of the bathymetry of Delaware Bay near the coastline from the LiDAR based DEMs (Figure 4.15). Consequently, these data must be merged with lower resolution bathymetry data, at the boundary of the coastline.

Delaware Bay bathymetry obtained from the Federal Emergency Management Agency (FEMA) has a resolution of 10 m. The bathymetry becomes very inaccurate

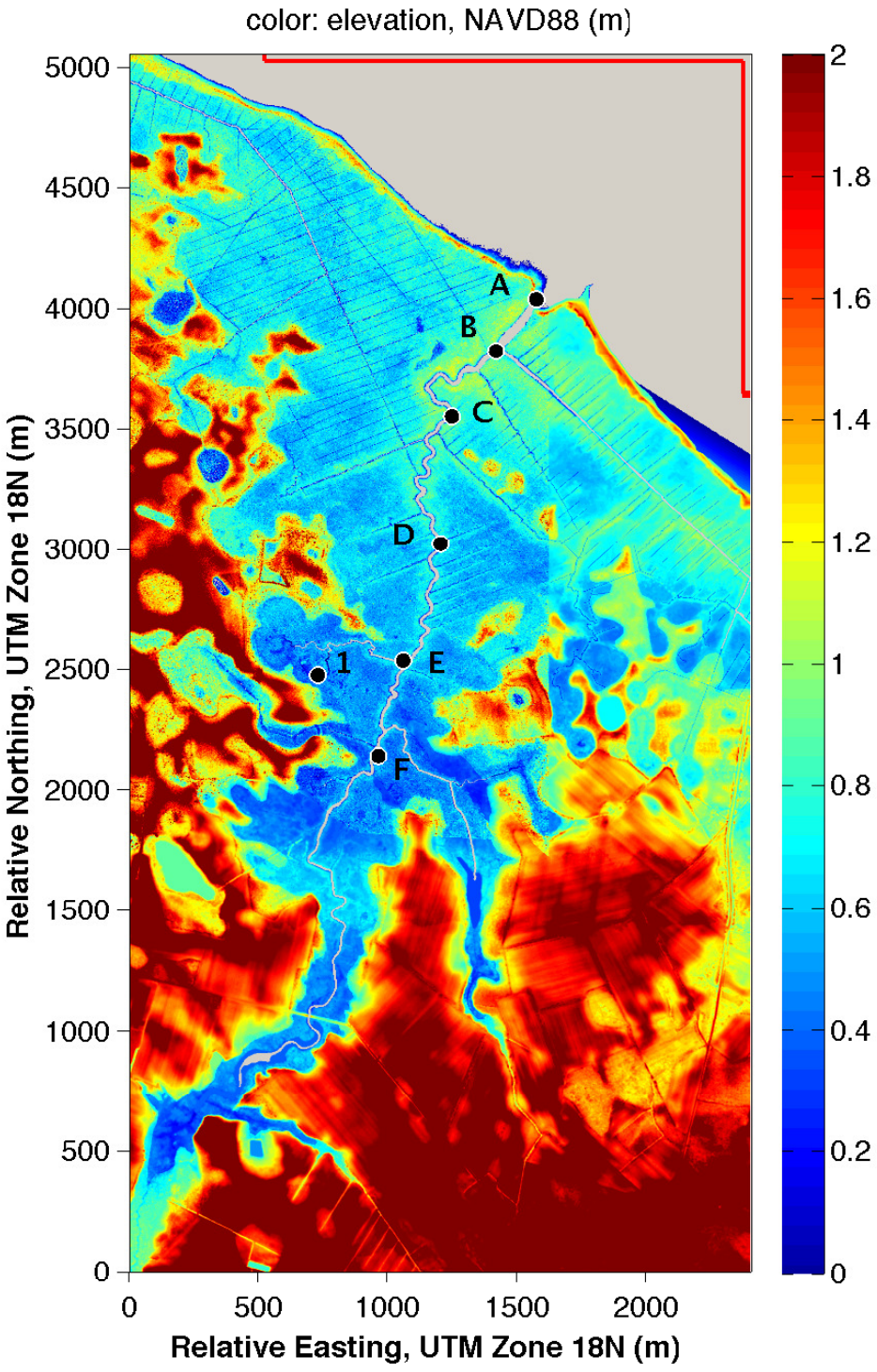

Figure 4.15: DEM of the large domain, encompassing nearly all of Brockonbridge Marsh. Only elevations above 0 m (NAVD88) are shown in order to more clearly distinguish small differences in elevation. Sites A-F and Site 1 are marked with black dots and labeled accordingly. The locations along the North and East open boundaries where the boundary conditions are imposed are boxed with red lines.

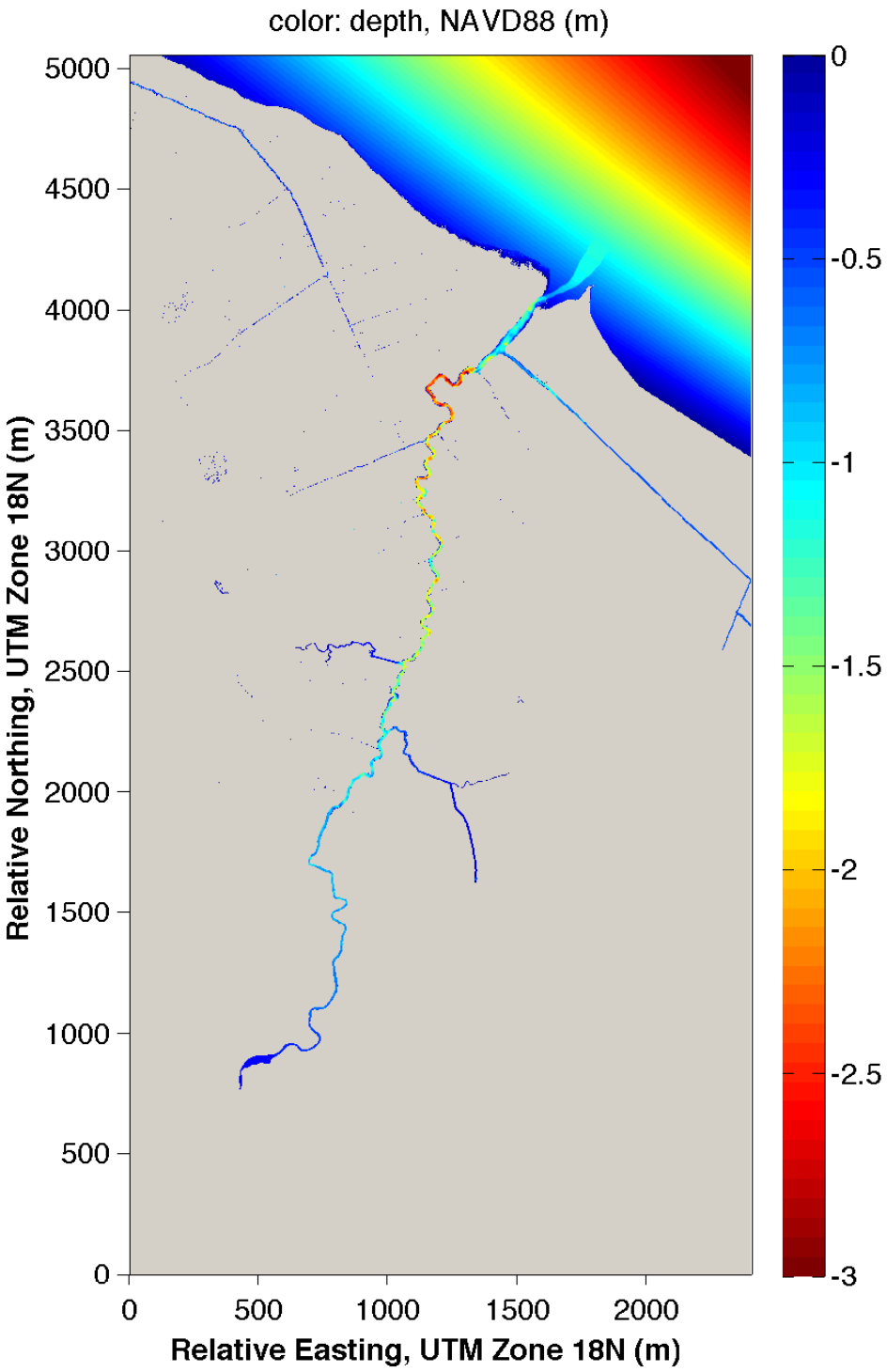

Figure 4.16: Bathymetry of the large domain, encompassing nearly all of Brockonbridge Marsh. Only elevations below 0 m (NAVD88) are shown in order to more clearly highlight small differences in depth.

near the coastline, due to the influence of higher elevation sand dunes. For much larger scale studies, this isn't a big issue. But when merging the 10 m grid with a highly accurate DEM with 2 m resolution, the inaccuracies in the FEMA data contaminate the merging boundary. Because of this problem, the bathymetry for Delaware Bay in the model domain was computed by applying a linearly sloping bed away from the coastline (Figure 4.16). The depth at the most offshore location was obtained from the FEMA dataset, which then defined the bottom slope. This essentially provided a first order approximation of the seabed. The highly approximated bed would suffice since its main purpose was to serve as a medium for marching the tidal boundary condition into Brockonbridge Gut. A few assumptions about the bathymetry near the inlet of the marsh had to be made, since it was known through field observations during low tides at the mouth that a shallow channel extended several tens of meters beyond the coastline, into the bay.

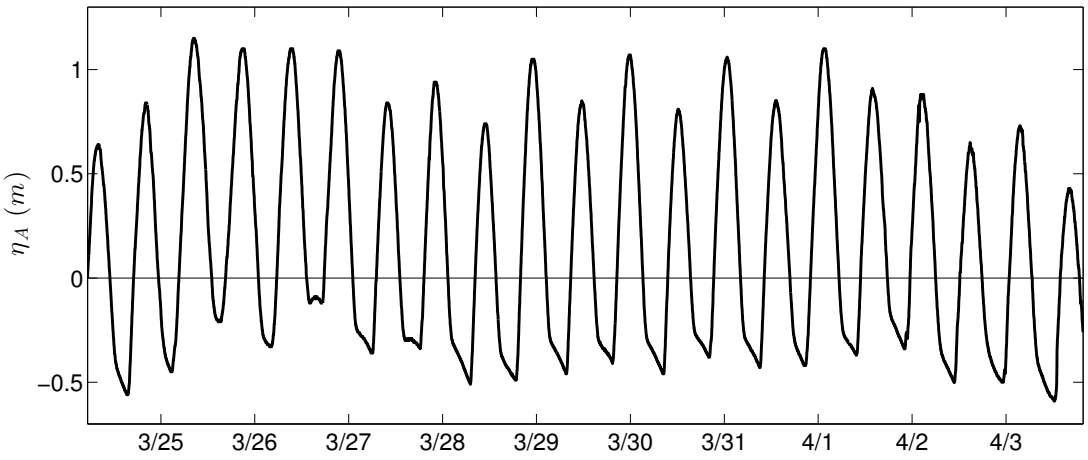

Figure 4.17: Time series of the boundary condition which was imposed at the open boundary grid points for the large domain, which are outlined with red boxes along the East and North open boundaries in the northeast corner of Figure 4.15.

The coupled boundary condition was applied to the open boundaries in the northeast region of the domain, which is outlined with red boxes in Figure 4.15. Again, the data from the ADCP deployed at Site A was used to force the water levels at the boundary (Figure 4.17). The forcing was applied uniformly at all points which were

to always remain wet. As before, the boundary condition was applied to all grid cells with a depth greater than 0.6 m.

In order to give the water levels in more landward areas of the domain some time to ramp up, the boundary condition begins early on March 24^{th}, the day before the surge event. This provides roughly two full tidal cycles for the model to ramp up before the arrival of the storm.

The same assumptions about the model that were listed for the small domain are made here. Finally, a Manning number of $n = 0.02$ is used, as was done with the small domain.

4.3.2 Results and Discussion

The results from the larger domain simulations proved to be able to better adjust to the large surge of water during the storm. Figure 4.18 clearly shows that the increased inter-tidal storage area removes the setup that was computed by the model during the storm in the small domain (Figure 4.10f). Furthermore, because of the increased storage area, a large pressure gradient does not form serving to drive water levels well below measured values during the storm. Rather, the water remains stored in the landward areas of the marsh. In fact, the larger domain introduces a new problem.

Figure 4.18 shows that flow in the channels is likely overdamped, causing water levels to remain high for several days compared to measurements. However, the level to which the tide drops during low waters during and after the storm is marked by a steady decline in both the field data and model results. This shows that the model is at least capturing the overall physical process of draining the marsh.

As was done in the previous section for the small domain, we take a look at the stage-discharge relationship to gain a better understanding of the total flux through the inlet (Figure 4.19).

While the two curves in Figure 4.19 appear to be completely different, there are a few similarities. First, the model accurately predicts the timing of flow reversal for

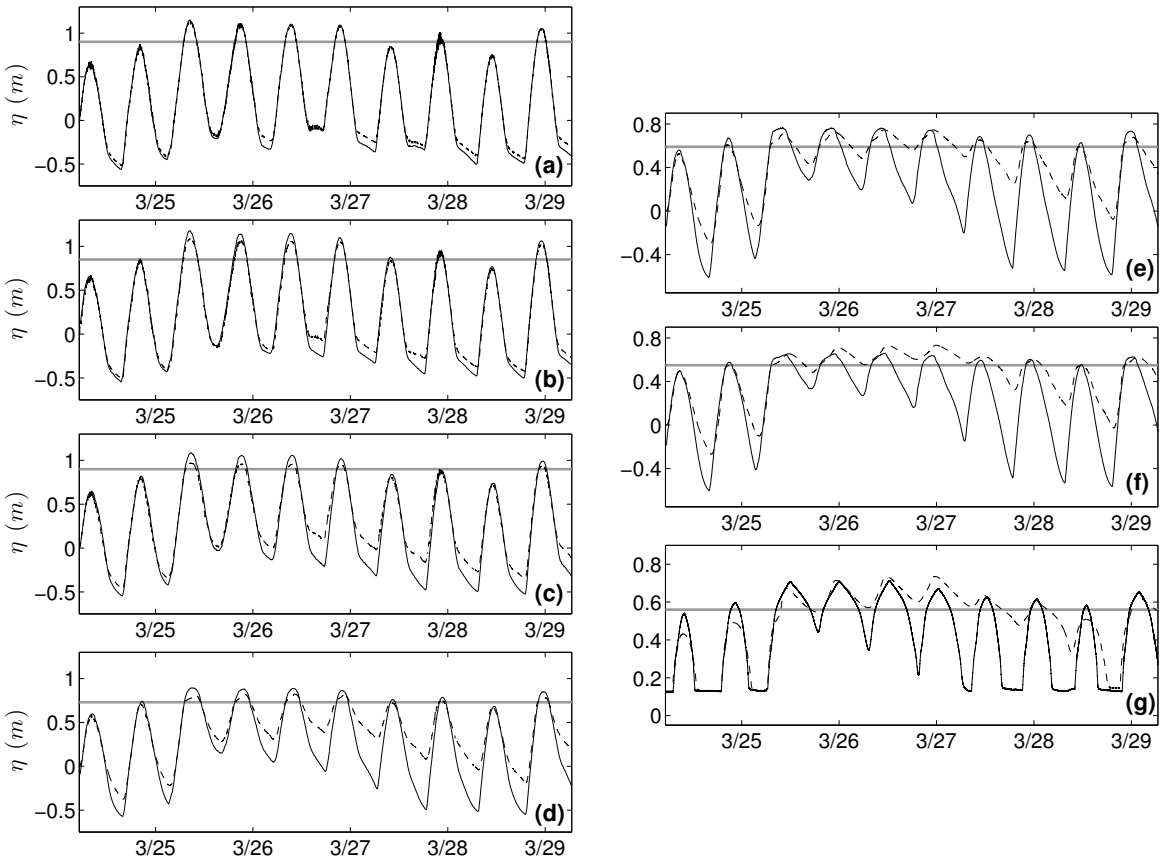

Figure 4.18: Model results for $\eta(t)$ vs field measurements, during and after the storm, for Sites A-F and Site 1 as labeled in Figure 4.15; (a) Site A, (b) Site B, (c) Site C, (d) Site D, (e) Site E, (f) Site F, (g) Site 1. The horizontal gray line marks the approximate marsh platform elevation at each site. The bed elevation of Site 1 in panel (g) is 15 cm, so the channel goes dry for several hours each time the tide flows out, with the exception of the presence of the storm. Note the difference in the scales of the y-axis between the left and right panels. — Field Data, - - Model Results

both flood to ebb, and ebb to flood. Furthermore, the model also accurately predicts the water levels at which the flow reversals occur. This demonstrates the model's ability to compute the phase of tidal propagation through the marsh very well. The surface elevation comparisons in Figure 4.18 support this as well.

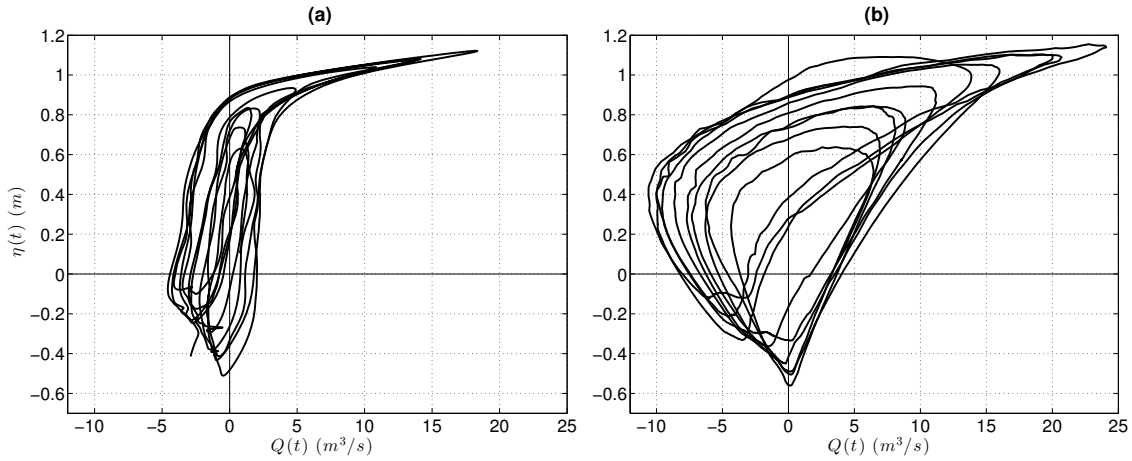

Figure 4.19: Stage vs discharge curves for (a) model results and (b) field data, between the dates of March 24, 2013 05:15 and March 29, 2013 06:30.

However, it is also very clear that the model largely under predicts the magnitudes of volumetric flux through the mouth. This is likely the reason for the computed elevated water levels during low tides. The flux through the mouth is under predicted because water levels are not dropping in the landward areas of the channel. In the model, mass must be conserved. If the total change in volume is small (i.e. water levels not dropping as much as measured data), the total flux will also be smaller than measured values in order to satisfy mass conservation.

Additionally, the benefit of moving the open boundary to a more offshore location is seen here. Unlike the discharge values during the storm for the small domain, the magnitudes of discharge computed by the model with the large domain are on the same order as the measured values. The reason for this is due to the larger inter-tidal storage capacity represented by the bigger model domain, which is more representative of the actual marsh.

Also, the field data in Figure 4.19 exhibits a continuously increasing magnitude of influx during rising tides, whereas the model results have a constant inflow until the water level reaches 0.8 m. At that height, the influx suddenly jumps to a peak value of about 18 m^3/s. Then, similarly to the field data, the rate of inflow undergoes a sharp decrease. The difference is that when the direction of flux flips to ebb, the model maintains a generally steady ebb discharge value, while the magnitude of ebb flux in the field data continues to increase with decreasing water levels. As will be pointed out in Chapter 5, the model results in Figure 4.19a are comparable to a highly overdamped marsh bisected by a single channel, with negatively sloping tidal flats away from the bay.

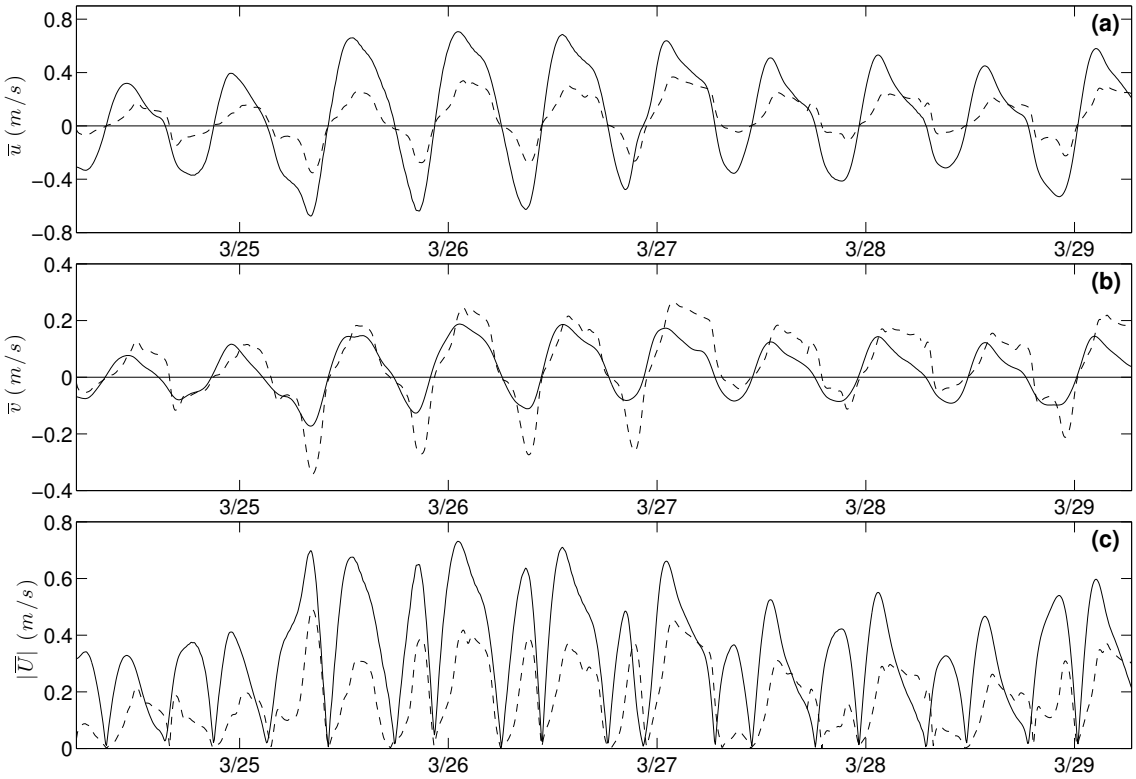

Figure 4.20: Model results for $\overline{u}(t)$, $\overline{v}(t)$ and $|\overline{U}|(t)$ vs field measurements, during and after the storm, for Site A; (a) depth-averaged East/West velocities, (b) depth-averaged North/South velocities, (c) Magnitude of depth-averaged velocity. — Field Data, - - Model Results

When we look at the computed versus measured magnitudes of velocities at Site

A (Figure 4.20), we see that the model velocities are never reaching the magnitude of measured values. This explains why there is not any pronounced bulge of influx or outflow in the model computed stage-discharge curve in Figure 4.19a. While it is obvious that the computed velocities are too low in magnitude to generate an enhanced ebbward flux during ebb phases following the storm, it's worth mentioning a few possible explanations for the differences between field measurements and model results.

First, an important factor that is neglected in the present modeling study is the linkage of Brockonbridge Marsh to the Murderkill River estuary during higher-high tides, such as spring high tides. The surge event likely inundated the channel that connects the two estuaries, which is labeled in Figure 2.2 and shown in the upper left region of the DEMs in Figures 4.15 and 4.16. Due to unknown boundary conditions at the connection with the Murderkill River, a no-flux condition was specified in the model. The possibility of the two estuaries being connected during the storm event is high. This connection may have served to help drain the Brockonbridge Marsh but is not quantifiable due to lack of any flow or tidal stage data acquired there.

Another possible cause for the prolonged suspended water levels in the model results can be linked to the under resolved "mosquito ditches" which are inundated during the surge event. Although care was taken to burn in these channels, many of them have widths that are less than the grid cell size of 2 m. As a result, many of them are not fully represented in the DEM, which can potentially block flow through them.

Finally, the assumption of a non-permeable bed was made; therefore, no water is able to drain through the bed in the model. Groundwater flow and soil saturation levels were not measured in the field study, so any quantitative explanations are difficult, if not impossible, to make. Although neglecting water draining through the marsh surface might have only contributed very slightly to the overall difference in water levels between the model and field data, it is worth pointing out. It certainly does not explain the large differences in magnitudes of flux through the mouth between measured and modeled results.

Chapter 5

MODELING IDEALIZED MARSHES WITH DIFFERING TOPOGRAPHIES

5.1 Introduction

As shown in Figure 2.12 and discussed in Chapter 2, there are clear asymmetries in duration of the rising and falling tides throughout the marsh. However, the magnitude of asymmetry is not constant over the 14-day cycle. During the first several days, the lag times are almost identical during flood and ebb tides, with falling tides lasting just slightly longer (Figure 2.12a). But during the storm, the rate at which the tide recedes during ebb phase is severely reduced, with this effect amplified further landward into the marsh (Figure 2.12b). Finally, Figure 2.12c continues to follow the overall trend of faster rising tides, accompanied by more slowly falling water levels.

Duration asymmetries of tidal propagation in frictionally dominated estuarine environments primarily arise through four sources of nonlinearity. In the momentum equation, the friction term is quadratic in velocity and depends inversely on time-varying channel depth. In continuity, time-varying channel depth again plays a role in nonlinearity, as does the variable width of the estuary with rising and falling tides.

LeBlond (1978) first proposed that in the frictionally dominant regime, more specifically in shallow rivers, tidal propagation can be understood as a nonlinear diffusive process, where time lags are accounted for by a constant, nonlinear diffusion coefficient. This solution does well in demonstrating that diffusion can sometimes explain long time lags better than a simple wave propagation model. But it falls short of accounting for time-varying parameters, such as changes in channel depth and embayment width, which play important roles in governing the diffusion of the wave's crest and trough.

Friedrichs and Madsen (1992) further derived second-order solutions for tidal propagation in a channelized estuary, closed at one end, by approximating the nonlinear diffusion coefficient as constant in space, and only expanding the time varying portion. The time varying diffusion coefficient in the solutions of Friedrichs and Madsen (1992) includes the influence of all four aforementioned principle sources of nonlinearities in frictionally dominated systems.

In the following chapter, a scaling analysis is first carried out to demonstrate the nature of friction dominance for Brockonbridge Marsh. Then, several idealized marsh domains will be simulated with NearCoM, with characteristic length scales chosen to most closely represent those of Brockonbridge Marsh. It will be shown that the approximate analytic solutions for the zeroth, second, and third harmonic components derived by Friedrichs and Madsen (1992) are very useful for describing the observed asymmetries in Figure 2.12a, where flow was primarily contained to channels. However, the diffusive solution fails to completely explain certain aspects of the apparent duration asymmetries in Figure 2.12b and 2.12c. The limitations of their diffusive solution will be explored, with further applications to Brockonbridge Marsh.

5.2 Scaling the Problem

To investigate the relative importance of each term in the governing equations, we use the formulation proposed by Speer and Aubrey (1985), which assumes a well-mixed, channelized estuary, with intertidal flats. Friedrichs and Madsen (1992) express the cross-sectionally averaged, 1-D continuity and momentum equations as

$$b\frac{\partial \zeta}{\partial t} + \frac{\partial (b_c h u)}{\partial x} = 0 \tag{5.1}$$

$$\frac{\partial u}{\partial t} + u\frac{\partial u}{\partial x} + g\frac{\partial \zeta}{\partial x} = -\frac{C_d u|u|}{h} \tag{5.2}$$

where b is the total width of the marsh, including tidal flats; h is the cross-sectional average of channel depth; ζ is the surface elevation; u is the cross-sectional average velocity; b_c is the channel width; and C_d is the drag coefficient. Additionally, in the

scaling analysis, it is assumed that $u = 0$ on the flats and that the channel width, b_c, is much greater than the cross-sectionally averaged channel depth ($b_c/h >> 1$).

If we scale tidal amplitude with a, velocity with U, time with the tidal period T, and x with a characteristic length scale L, and further assume that tidal amplitude and velocities change over a similar length scale, it can be shown that friction scales with inertia in the following way (Friedrichs and Madsen, 1992),

$$\frac{Friction}{Inertia} = \frac{TUC_d}{h} \tag{5.3}$$

There are two final constraints in the scaling analysis to consider. First, according to typical scale values, for friction to dominate, the amplitude of current velocities associated with the dominant M_2 constituent should be ~0.5 m/s. Second, the ratio of tidal amplitude to average channel depth should be large enough for friction to have a more significant influence than inertia. The frictional dominance tends to break down when $a/h < 0.1$ (Pingree and Maddock, 1978).

The magnitude of velocity, U, in Brockonbridge Marsh is well described by a characteristic scale of 0.5 m/s (Figure 2.13b). This falls into the necessary range mentioned above. Other characteristic scales in Brockonbridge Marsh are as follows: $T \sim 12$ hrs ($\sim$ 43,000 sec), $a \sim 0.75$ m, $h \sim 2$ m. Typical values for C_d are usually between 10^{-2} - 10^{-3}. With these values, using (5.3), our scaling argument tells us that the friction term should dominate the inertial term by 1 to 2 orders of magnitude. We also note that for Brockonbridge Gut, $a/h > 0.1$.

5.3 Introduction to Nonlinear Diffusion of Tidal Propagation

In order to make the interpretation of the results more understandable, a brief description of the methods and parameters used by Friedrichs and Madsen (1992) is provided. After using the frictional dominance assumption to derive a zero-inertia governing equation, their solution for $\zeta(t)$ is obtained from the following 1-D, constant

diffusion equation

$$\frac{\partial \zeta}{\partial t} - D_0 \frac{\partial^2 \zeta}{\partial x^2} = 0 \tag{5.4}$$

with

$$D_0 = \frac{\overline{b}_c \overline{h}_0^{5/3}}{\overline{b}_0 n \overline{(|\partial \zeta / \partial x^{1/2}|)}_0} = constant \tag{5.5}$$

where ζ is surface elevation, D_0 is the diffusion coefficient, n is Manning's friction parameter, b_c is average channel width, b is the average width of the entire embayment, and h is the cross-sectionally averaged channel depth. The overbars, $\overline{()}$, denote average values which are x-independent, while subscripts $()_0$ denote time-averaged quantities. Once a solution is derived from (5.4), they expand the time-varying geometric parameters, using values at the mouth to be representative.

An estuary with a prismatic geometry is assumed, similar to that of Speer and Aubrey (1985). A forcing condition is applied at the mouth, which is defined to be located at $x = L$, using a sine wave with amplitude, a and period, T,

$$\eta(t) = asin(\omega t)$$

where L is the total length of the channel, and ω is the angular frequency, $\omega = 2\pi/T$. At the landward end, $x = 0$, the following boundary condition is imposed:

$$\frac{\partial \zeta}{\partial x}|_{x=0} = 0$$

The assumption that the geometric parameters in the diffusion coefficient, D_0, are not a function of x reveals one of the limitations in applying the solution of Friedrichs and Madsen (1992). Moreover, the diffusion equation in (5.4) is one-dimensional, in the x-direction, which doesn't account for the influence of transverse tidal propagation over a slowly varying flat, as a result of sharp changes in bathymetry. Nonetheless, in each idealized case, representative values were assigned, in order to compare the model results to the analytical solution.

Finally, Friedrichs and Madsen (1992) define an asymmetry parameter, γ, as

$$\gamma = \frac{5a}{3\bar{h}_0} - \frac{\Delta\bar{b}}{\bar{b}_0} \tag{5.6}$$

where $\Delta\bar{b}$ represents half of the total change in estuary width between low and high tide. For $\gamma > 0$, the changes in channel depth over a tidal cycle are more important than changes in embayment width. This results in an overall flood dominance, as the high tide from the next tide cycle will "catch up" to the low tide from the previous tide. Conversely, for $\gamma < 0$, changes in the width of the estuary between low and high tide are dominant over changes in depth. The result is a faster falling tide, accompanied by a more slowly rising tide, leading to an ebb dominant system.

The parameter $||k_0||L$, where the double bars denote magnitude of the complex number $k_0 = \left(\frac{i\omega}{D_0}\right)^{1/2}$, is described completely in Friedrichs and Madsen (1992), but the following qualitative description should suffice for this manuscript. Essentially, the value of $||k_0||L$ takes into account all of the spatially-averaged geometrical parameters of the estuary, including the friction factor. Very small values of $||k_0||L$ correspond to a solution similar to a standing wave, where peak velocities precede high and low waters by 90°. Very large values of $||k_0||L$ correspond to solutions more like a decaying progressive waveform, where high and low waters are out of phase with peak velocities by 45°.

Two approximate solutions are given in Figures 5.1 and 5.2 with $||k_0||L$ values of 1.562 and 3.492, respectively. These values are chosen to plot based on model runs C1, D1 and C2, D2, which are described in the next section, such that comparisons may later be drawn. As the value of $||k_0||L$ increases, the effective distance over which the signal travels decreases. This is why in Figure 5.2, there is a pronounced separation between the curves and their maximum amplitudes. The curves in Figure 5.2 also demonstrate the aforementioned 45° shift in phase.

It's important to note that the x-direction used in this section represents a direction parallel to the channel. This is used in order to be consistent with Friedrichs

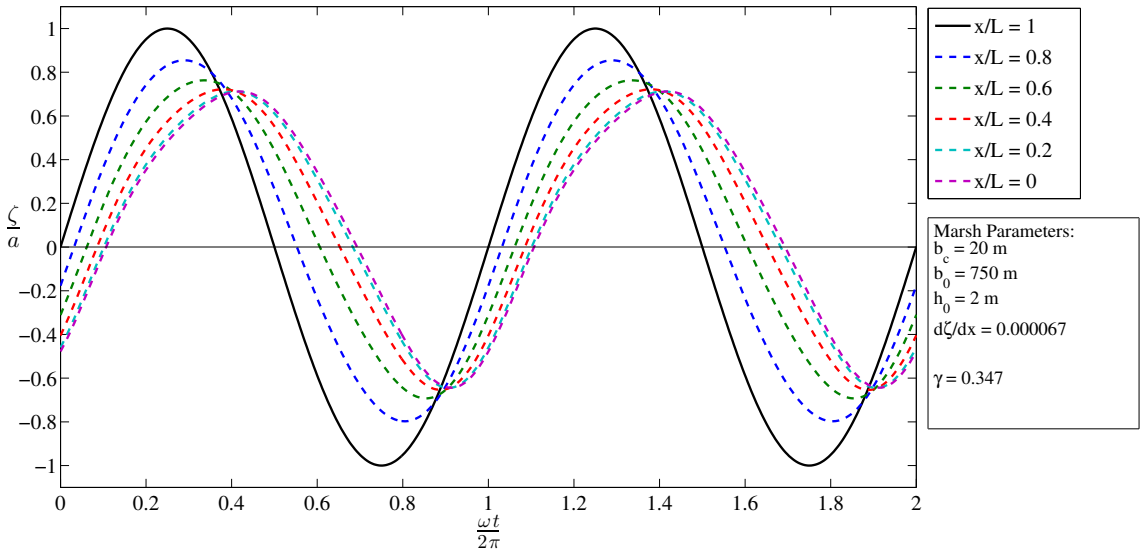

Figure 5.1: Approximate analytic solution to time-varying coefficient diffusion equation in Eq. (5.4), with $n = 0.02$ and $||k_0||L = 1.562$.

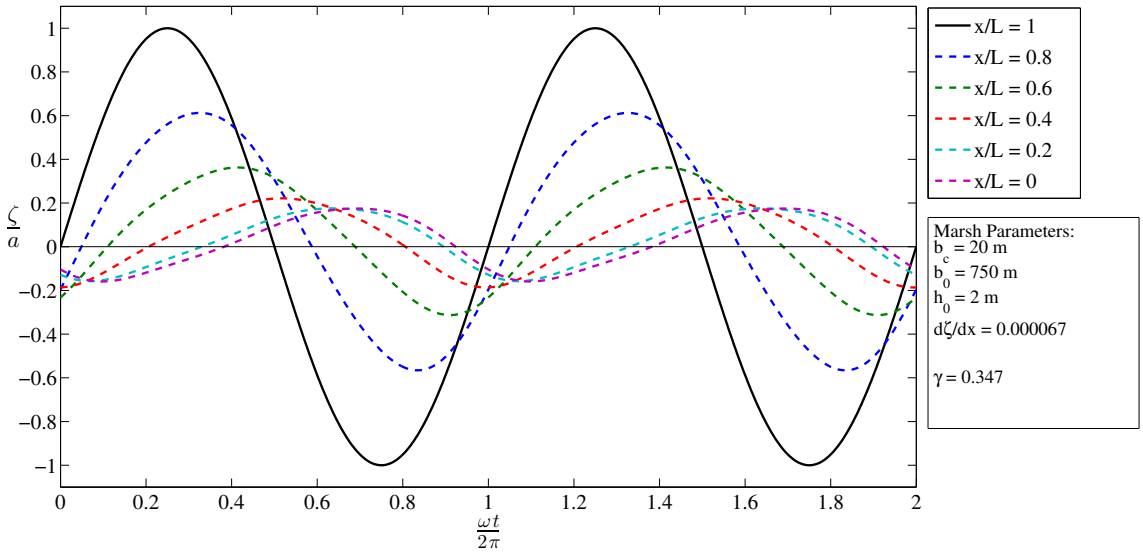

Figure 5.2: Approximate analytic solution to time-varying coefficient diffusion equation in Eq. (5.4), with $n = 0.02$ and $||k_0||L = 3.492$.

and Madsen (1992). However, in subsequent sections, the x-axis will be transverse to the direction of the channel, while the y-axis will represent the direction along the channel's axis.

5.4 Model Setup

Four different types of idealized marshes were considered in the simulations (Table 5.1). All four types are incised by one channel, which extends to the end of the domain. Also, all four types contain an open boundary at one end, which represents a bay, where tidal forcing is applied. Finally, every idealized marsh is separated from the bay by representations of sand dunes, with an opening for an inlet in the middle. Although not the case for the Brockonbridge Gut, as discussed in Chapter 2, the depth of the channels for the idealized marshes linearly decreases away from the bay.

Table 5.1: Descriptions of the configurations of the tidal flats in the four types of idealized marshes that were considered in the simulations.

Type	Description of Tidal Flat Configuration	Example
A	Flow in channel only, no flow onto tidal flats	Figure 5.3
B	Tidal flat elevations increasing away from channel centerline ($\pm$ x-direction)	Figure 5.4
C	Tidal flat elevations increasing away from bay ($+$ y-direction)	Figure 5.5
D	Tidal flat elevations decreasing away from bay ($+$ y-direction)	Figure 5.6

It should also be mentioned that a slope is defined for the tidal flats in only one spatial direction. For example, the slope of Type B flats (Figure 5.4) varies in the x-direction, with no elevation changes in the y-direction. The opposite is true for Type C & D flats. This was done in order to isolate the effects of each specific flat configuration.

For the grid used in case D-SiteA (Figure 5.7), the marsh platform elevation at the mouth is 1.2 meters and then decreases to 0.34 m at the landward boundary. These values are specifically drawn from representative elevations of Brockonbridge Marsh at these locations.

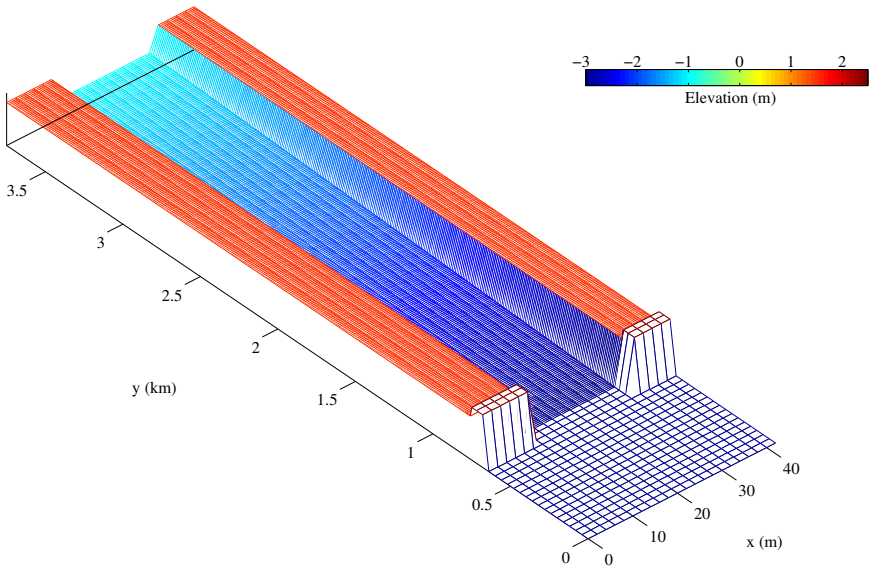

Figure 5.3: Example of a Type A configuration. Grid used for model runs A1, A2 and A3. Note: the x-axis is in meters while the y-axis is given in kilometers. Inside the channel, Δx is 2 m. In the bay, Δy is 40 m. Not to scale.

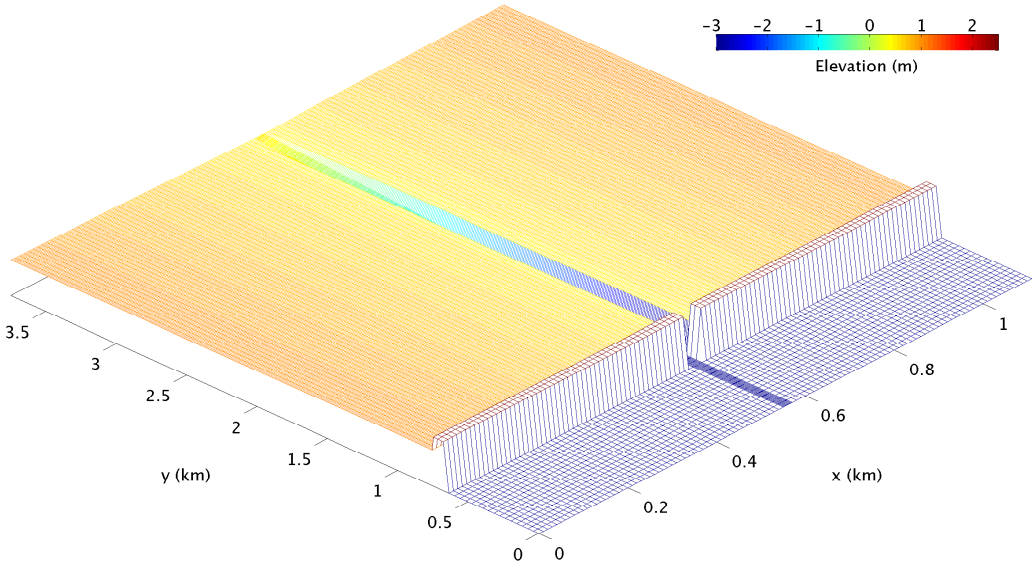

Figure 5.4: Example of a Type B configuration. Grid used for model runs B1, B2 and B3. Inside the channel, Δx is 2 m, and Δy is 10 m. On the flats, Δx increases to also be 10 m, equaling Δy. In the bay, Δx is 10 m and Δy is 40 m. Not to scale.

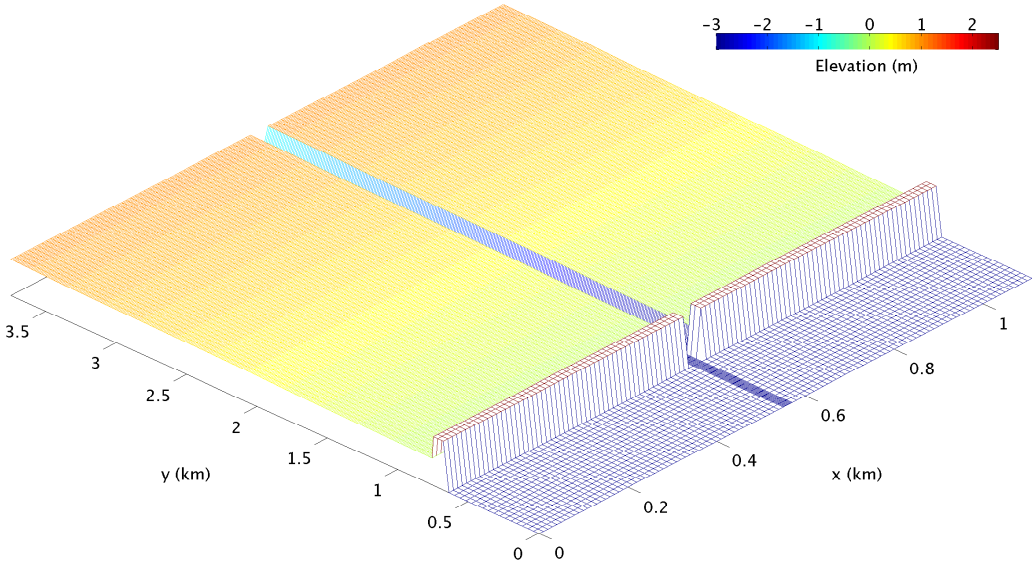

Figure 5.5: Example of a Type C configuration. Grid used for model runs C1 and C2. Inside the channel, Δx is 2 m, and Δy is 10 m. On the flats, Δx increases to also be 10 m, equaling Δy. In the bay, Δx is 10 m and Δy is 40 m. Not to scale.

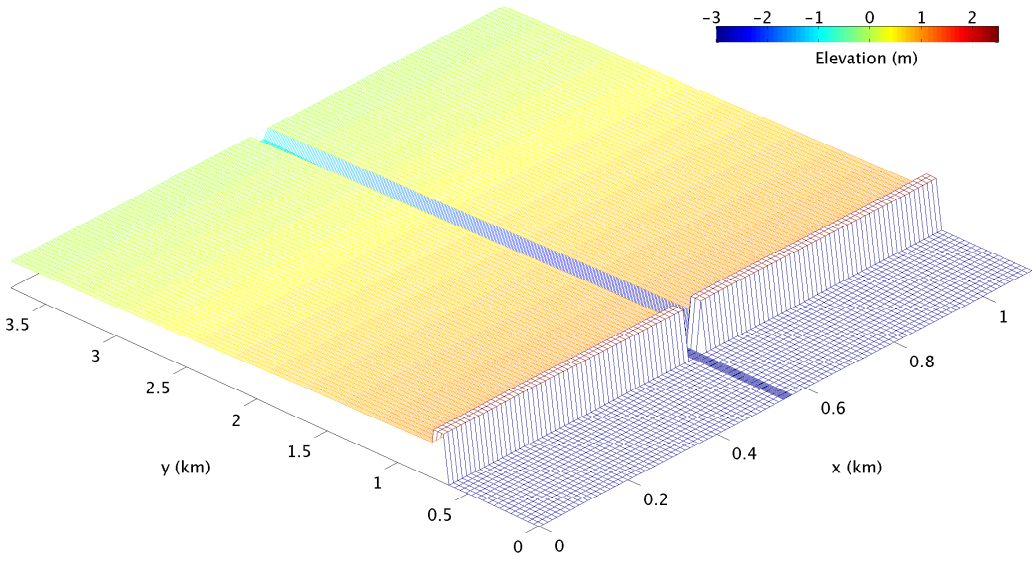

Figure 5.6: Example of a Type D configuration. Grid used for model runs D1 and D2. Inside the channel, Δx is 2 m, and Δy is 10 m. On the flats, Δx increases to also be 10 m, equaling Δy. In the bay, Δx is 10 m and Δy is 40 m. Not to scale.

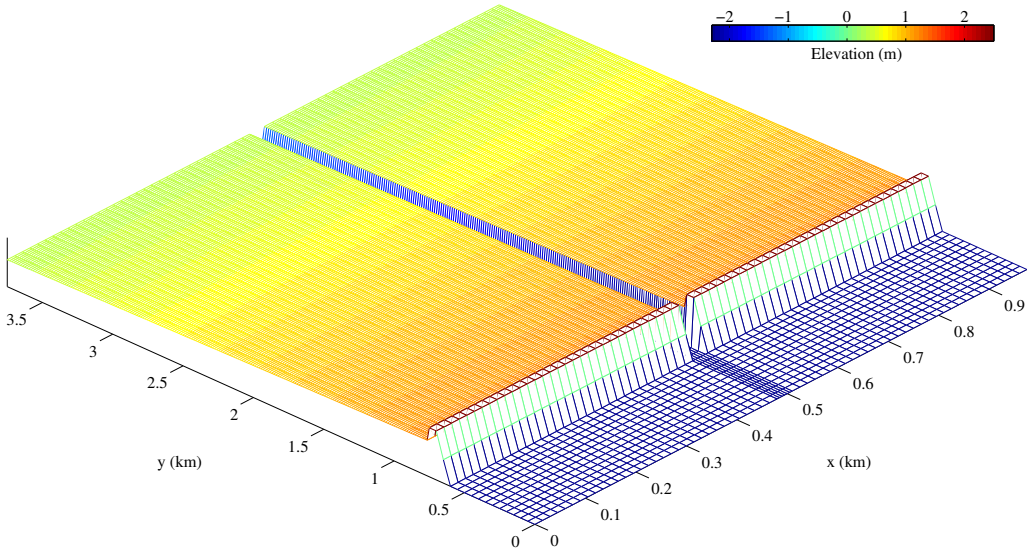

Figure 5.7: Grid for model run D-SiteA (Type D). Inside the channel, Δx is 5 m, and Δy is 15 m. On the flats, Δx increases to also be 15 m, equaling Δy. In the bay, Δx is 15 m and Δy is 50 m. Not to scale.

Figures 5.3 - 5.7 depict the five different grids that were used in the simulations. Further explanations of the grids, including magnitudes of marsh platform slopes and channel slopes, as well as boundary conditions and model parameters, are described in Table 5.2.

Several parameters are held constant in every case and are omitted from Table 5.2, for compactness and instead, are mentioned here. First, the width of the channel, w, is 20 m in every simulation. The length of the channel, L, is also constant across all simulations, at 3 km. These values are held constant in order to isolate the effects of other parameters like marsh platform slope and friction. Finally, all model domains are padded with 750 meters of open water having a depth of 3 meters at MWL, extending seaward from the dunes.

For all simulations, with the exception of run D-SiteA, the open boundary conditions were applied as a simple sinusoidal wave, with amplitude a and period T

$$\eta(t) = asin(\omega t) \tag{5.7}$$

where $\omega = \frac{2\pi}{T}$ is the angular frequency of the wave. For all runs except number D-SiteA, the period of the M_2 tidal constituent was used, which is 12.42 hrs, and the amplitude was set to 1 meter. For model run D-SiteA, the boundary condition was specified by imposing the water level measured by the ADCP from Site A during the field experiment.

In every case, the boundary conditions are applied to every grid point for $y = 0$, as well as the ends of the domains, where $x = 0$ and $x = x_{max}$, at all boundary points seaward of the sand dunes. Additionally, the initial water level in all simulations is 0 m everywhere.

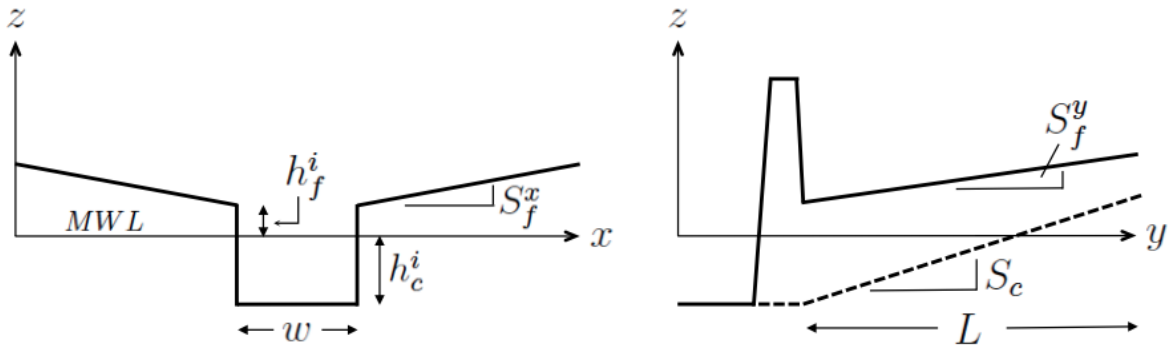

Figure 5.8: Schematic setup of an idealized marsh with dunes separating the marsh platforms from open water. The variables which are defined are given for each case in Table 5.2.

In every simulation, the minimum depth for wetting/drying is defined as 0.01 meters, and Fr_{cap} is defined to be 0.8. Friction is varied throughout the cases in order to investigate its role in distorting the tide's propagation. In all but one case, a Manning number is defined so that the magnitude of the drag coefficient is inversely dependent on $H^{1/3}$ as shown in Figure 3.1. This is important when large, sudden variations in elevation exist in the domain, causing the water depth in neighboring cells to differ substantially during flooding and draining over the channel banks. The effect this has on the residual stress and circulation is also of interest.

Table 5.3 provides a list of the $||k_0||L$ values corresponding to each run. The implications of $||k_0||L$ on the analytical solution are given in section 5.3. The actual values

Table 5.2: Comprehensive description of simulation parameters for idealized marsh domains. The first letter in the Run ID denotes the marsh platform configuration type, as defined in Table 5.1. Variable definitions can be found in Figure 5.8.

	B.C.s		Domain Parameters					Friction	
Run ID	a (m)	T (hrs)	S_f^x	S_f^y	S_c	h_f^i (m)	h_c^i (m)	n [(1)] $(m^{-1/3}s)$	C_d
A1	1	12.42	-	-	2/3000	1.5	-3	0.02	-
A2	1	12.42	-	-	2/3000	1.5	-3	0.1	-
A3	1	12.42	-	-	2/3000	1.5	-3	0.2	-
B1	1	12.42	1/1000	0	1/1000	0.5	-3	0.01	-
B2	1	12.42	1/1000	0	1/1000	0.5	-3	0.02	-
B3	1	12.42	1/1000	0	1/1000	0.5	-3	-	0.02
C1	1	12.42	0	1/3000	2/3000	0	-3	0.02	-
C2	1	12.42	0	1/3000	2/3000	0	-3	0.1	-
D1	1	12.42	0	-1/3000	2/3000	1	-3	0.02	-
D2	1	12.42	0	-1/3000	2/3000	1	-3	0.1	-
D-SiteA	η (Site A)		0	-1/3500	2/3000	1.2	-2.5	0.02	-

(1) *Manning's coefficient as used in Equation 3.16*

for $||k_0||L$ are computed using the parameters given in Table 5.2 for each simulation.

Table 5.3: Summary of $||k_0||L$ values for select runs.

Run ID	$||k_0||L$
A1	0.180
A2	0.403
A3	0.570
B1	0.758
B2	1.072
B3	2.056
C1	1.562
C2	3.492
D1	1.562
D2	3.492

5.5 Results and Discussion

In this section, it will be demonstrated that not only does the presence of tidal flats in channelized marshes play a role in distorting the tide, but that slope direction is just as important of a factor in determining the asymmetries present in tidal marshes.

As was done in Chapters 2 and 4, stage-discharge curves will again be utilized to investigate the nature of each system. Volumetric flux through the mouth, $Q(t)$, can be computed by summing over the entire channel inlet as follows,

$$Q(t) = \Sigma_{n=1}^{N} v(x_n, t) \left[h(x_n, t) + \eta(x_n, t) \right] \Delta x \tag{5.8}$$

where x_n is the x-value at the nth grid cell along the channel mouth containing a total of N grid points, $v(x_n, t)$ is the velocity in the y-direction, $h(x_n, t)$ is the depth, $\eta(x_n, t)$ is the surface elevation, and Δx is the grid spacing between adjacent cells. Positive values of $Q(t)$ indicate flooding, and negative values represent ebb flow.

5.5.1 Type A Marshes

As would be expected for such a small $||k_0||L$ value, the curves in Figure 5.9 do not exhibit any phase lags with distance increasing landward. This is characteristic of

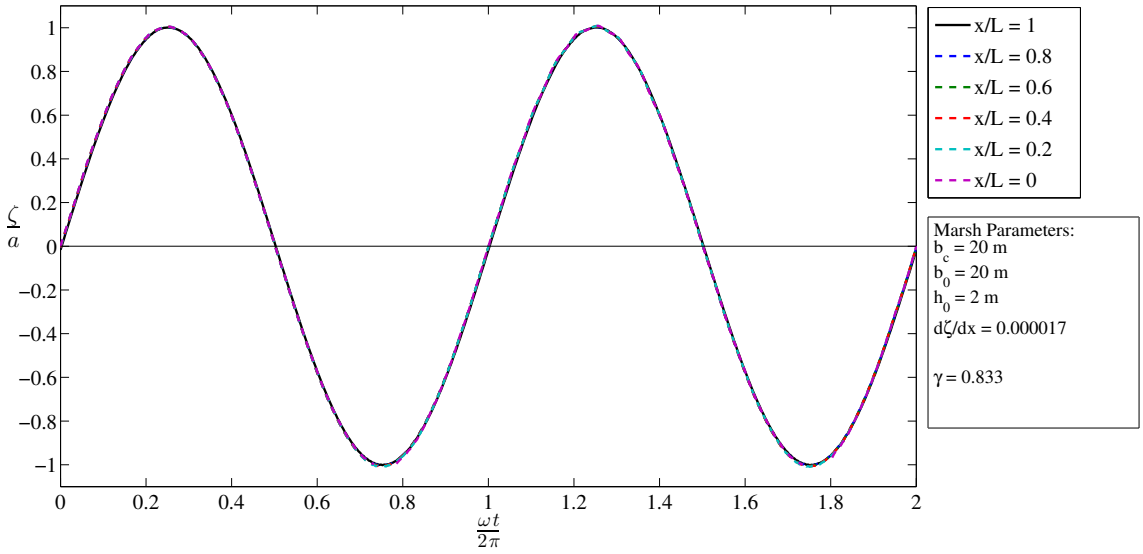

Figure 5.9: Surface elevations for simulation A1, with $n = 0.02$ and $||k_0||L = 0.180$. The channel mouth is defined to be located at $x = L$, based on the notation used by Friedrichs and Madsen (1992). The landward end is defined at $x = 0$.

small values for $||k_0||L$, which have solutions like a standing wave with long wavelength. For cases A2 and A3, Manning's friction factor is 0.1 and 0.2, respectively. However,

we note that such a large Manning number is unreasonable, especially for open channel flow with no obstructions. Nevertheless, in order to demonstrate the relation between friction and tidal distortion in short estuaries (3 km in the cases considered here) with no tidal flats, such large friction factors are necessary.

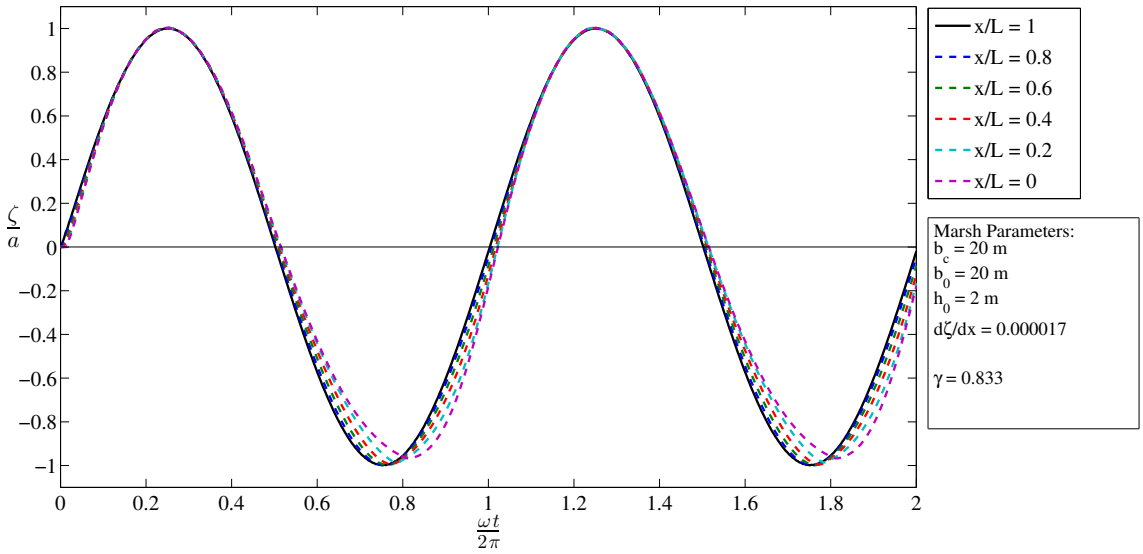

Figure 5.10: Surface elevations for simulation A2, with $n = 0.1$ and $||k_0||L = 0.403$. The channel mouth is defined to be located at $x = L$, based on the notation used by Friedrichs and Madsen (1992). The landward end is defined at $x = 0$.

With a Manning number of 0.02, case A1 shows no asymmetries in tidal propagation (Figure 5.9). As the magnitude of friction is increased with runs A2 and A3, a slight phase shift emerges (Figures 5.10 and 5.11). The phase shift becomes much more pronounced as the water depth decreases and appears to be symmetric for both falling and rising tides. In all three cases, $\gamma = 0.833$, which would suggest that changes in water depth dominate changes in estuary width, resulting in a flood dominant signature in the tidal signal. The limitation in the ability for γ to predict flood/ebb dominance becomes evident here, since it does not account for the role of friction. While cases A2 and A3 exhibit asymmetries characteristic of flood dominance, marked by a longer falling tide, A1 does not show any asymmetries. These differences are solely due to the magnitude of the friction factor. Furthermore, the influence of the depth dependent

drag coefficient is likely the reason for the lack in phase shift during high waters for all three cases. Even with a Manning number of 0.2 for case A3, there is no surface gradient during high waters. The amplitude of the crests at each location for run A3 are also unaffected by any damping as they all reach the same maximum, whereas there are clear differences in the levels that are reached by low waters in the higher friction cases, A2 and A3 (Figures 5.10 and 5.11).

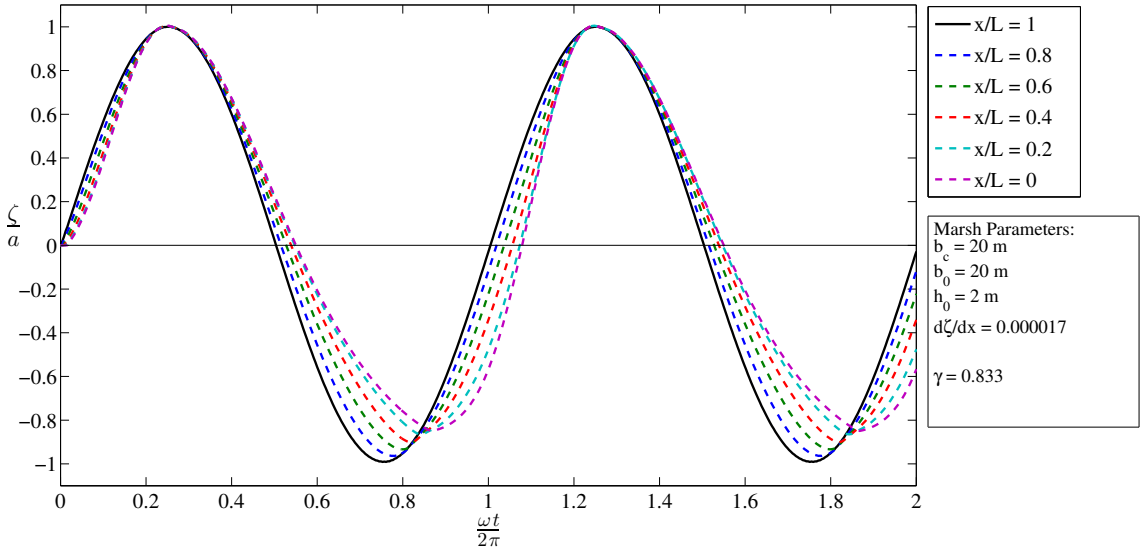

Figure 5.11: Surface elevations for simulation A3, with $n = 0.2$ and $||k_0||L = 0.570$. The channel mouth is defined to be located at $x = L$, based on the notation used by Friedrichs and Madsen (1992). The landward end is defined at $x = 0$.

From Figure 5.12, it appears that friction has a considerable effect in distorting the overall discharge. There is a slight phase shift between $\eta(t)$ and velocity for case A2, becoming even more pronounced for run A3, when Manning's friction coefficient is increased to 0.2. But the magnitude of total flux, as well as the maximum and minimum discharge values, do not show much difference between runs.

Aside from the slight bulges in a few areas of the curves in Figure 5.12, all three runs of Type A primarily exhibit the behavior of a standing wave in a channel, where peak velocities are nearly 90° out of phase with maximum and minimum water levels. This is important because the domain in these simulations does not have tidal flats.

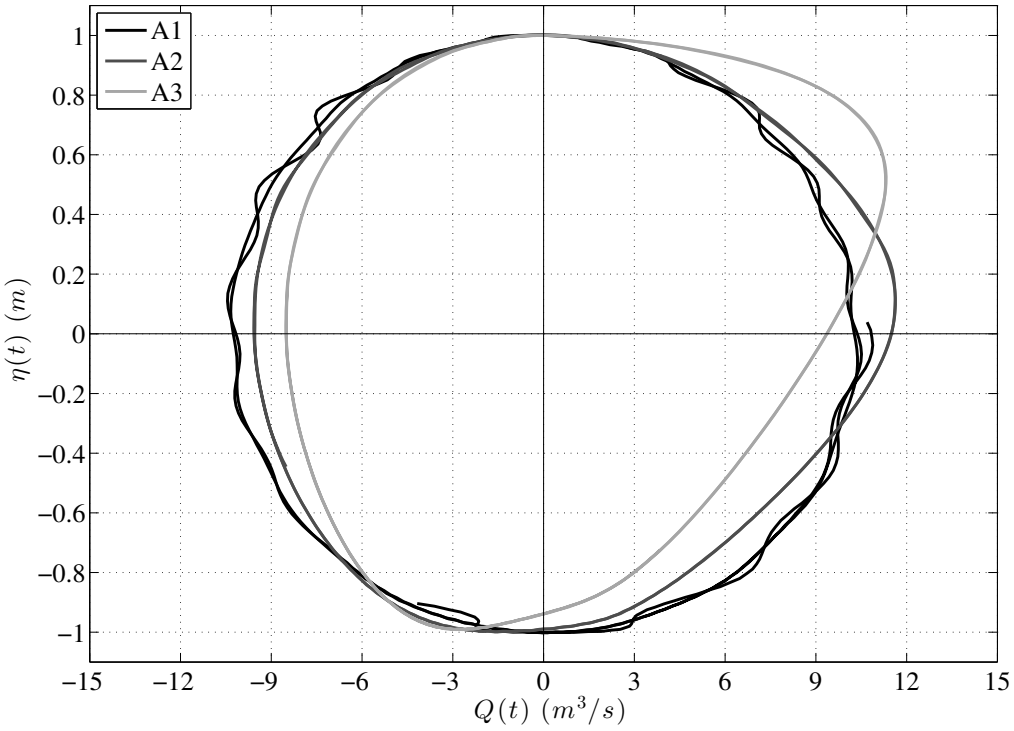

Figure 5.12: Stage-discharge curves for simulations A1, A2 and A3.

Therefore, it has been demonstrated that the lack of presence of any marsh platforms leads to friction being the the dominant mechanism for generating tidal asymmetries leading to distortion in tidal discharge.

5.5.2 Type B Marshes

These simulations all represent marshes with Type B platforms (Figure 5.4), using different friction factors (Table 5.2). The elevation of the banks of the flats at the edges of the channel is 0.5 m.

Figures 5.13 - 5.15 show that as the tide rises from low tide, in all three cases, friction in the channel does not play a role in damping the propagation of the tide. In fact, even though we see separation of the three curves during falling water levels, in all three cases the ensuing rising tide catches up with the previous falling tide, seemingly no matter the friction. The reason for the breaks in the curves for low values of x/L is due to the channel going dry. This is a consequence of the channel slope and marsh configuration. At the end of the domain, $x/L = 0$, the elevation of the channel is 0.5 m (see Figure 5.4).

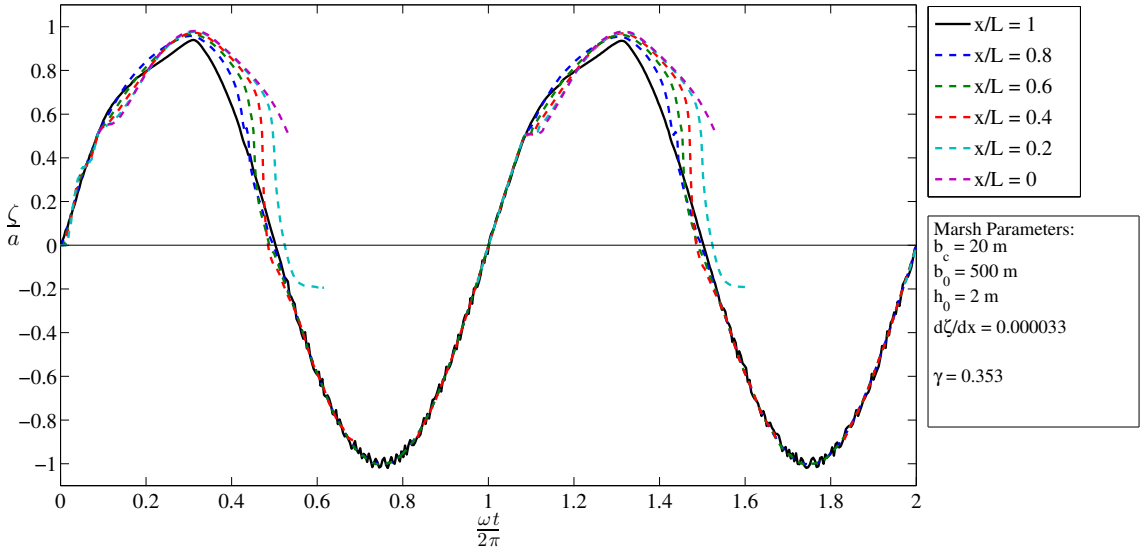

Figure 5.13: Surface elevations for simulation B1, with $n = 0.01$ and $||k_0||L = 0.758$. The channel mouth is defined to be located at $x = L$, based on the notation used by Friedrichs and Madsen (1992). The landward end is defined at $x = 0$.

All three cases also demonstrate the role in which tidal flats play in distorting the tidal signals. As the water levels reach to 0.5 m, the rate at which the tide rises decreases. This decreasing trend also becomes slightly more pronounced further into the domain. As the water levels drop below the banks, the surface in the landward areas of the channel adjust to be equal to the water level at the mouth. Regardless of the magnitude of friction in cases B1 - B3, the rising tide seems to catch up with the previous falling tide.

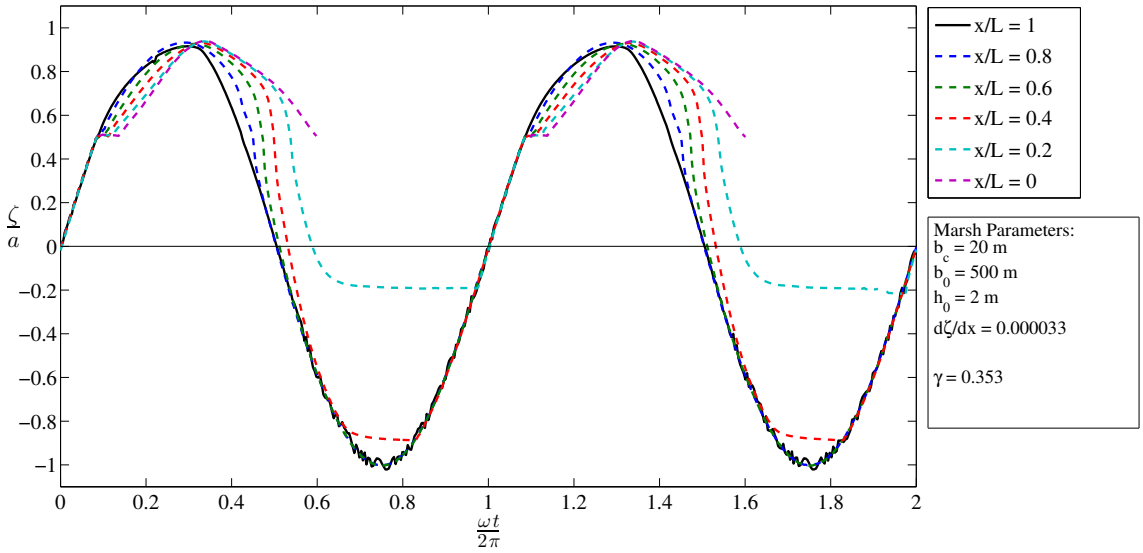

Figure 5.14: Surface elevations for simulation B2, with $n = 0.02$ and $||k_0||L = 1.072$. The channel mouth is defined to be located at $x = L$, based on the notation used by Friedrichs and Madsen (1992). The landward end is defined at $x = 0$.

Figure 5.16 presents the stage-discharge curves for simulations B1 - B3. The portions of the curves that emanate from the origin are the model runs "spinning up" from their initial condition of a flat water surface everywhere.

As the water levels rise and begin inundating the flats, at +0.5 m, the curve in Figure 5.16 undergoes a large distortion. At this elevation, for just small changes in water level, volumetric flux into the marsh experiences a sharp increase. This is due to the increase in surface area, leading to an increase in storable volume for small adjustments in water depth. The magnitude of distortion, however, becomes markedly

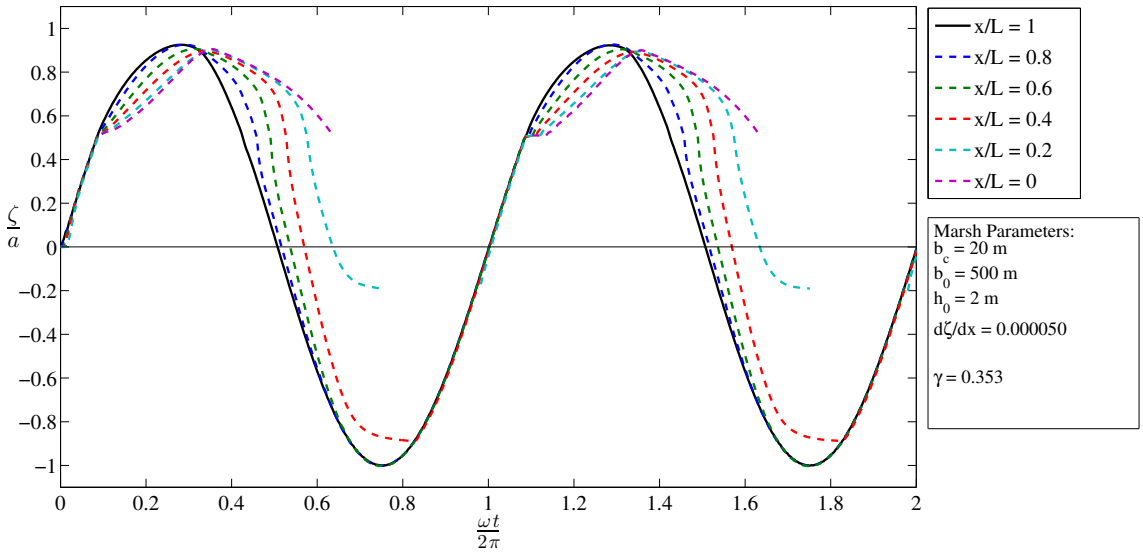

Figure 5.15: Surface elevations for simulation B3, with $C_d = 0.02$ and $||k_0||L = 2.056$. The channel mouth is defined to be located at $x = L$, based on the notation used by Friedrichs and Madsen (1992). The landward end is defined at $x = 0$.

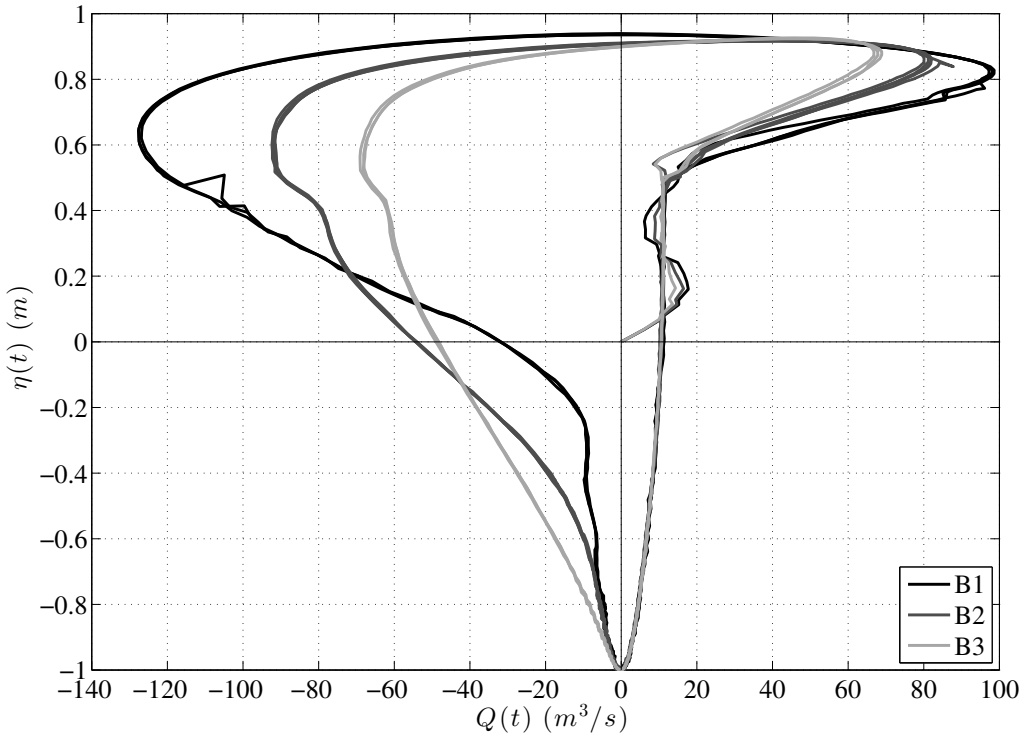

Figure 5.16: Stage-discharge curves for simulations B1, B2 and B3.

smaller for increasing friction. The total inflow becomes smaller for increasing friction, leading to a smaller total outflow during falling tide. Though generally, in each case, the peak flood fluxes all occur slightly before the maximum water level.

In Figure 5.16, as the flux direction switches from flood to ebb, the rate at which the water level drops increases with increasing friction. In general, the magnitude of the discharge continues to increase until water levels reach the elevation of the banks where the flats meet the channel. At this point, the discharge begins to decrease along with decreasing water levels. This decreasing trend continues in all three cases, but at an increased rate for smaller friction, until low tide, where the flux reaches its minimum value.

The simulations in runs B1 - B3 all exhibit behavior that is expected of a marsh that is dominated by changes in width over the course of a tidal cycle. This is the most commonly studied tidal flat configuration (Friedrichs, 2010). So while the results of B1 - B3 are certainly conclusive and align with observations from previous studies (Pethick, 1980; Boon and Byrne, 1981; Aubrey and Speer, 1985), they merely serve as a benchmark in identifying the shortcomings of this idealized case when it comes to explaining the dynamics of real-world marshes that don't follow the Type B flat arrangement.

5.5.3 Type C Marshes

Cases C1 and C2 have Type C tidal flats, starting from 0 m elevation at the mouth and increasing to 1 m at the landward end (Figure 5.5). The height of the channel sidewalls at the inlet is 3 meters. This configuration is also a common assumption, where the flat slope is positive away from the open water at the entrance of the domain.

For run C1 (Figure 5.17), the surface elevations throughout the channel don't experience a separation as water spills onto the flats, as was the case with simulations B1-B3. This is a consequence of the change in slope of the platform being in the same

direction as the change in slope of the channel. As a result, the platforms in Type C marshes are flooded from the same side as the channel, both from the mouth.

Figure 5.18 shows a similar trend as case C1, just shifted slightly more out of phase due to enhanced friction. Run C2 also shows how increased friction causes the propagation of the tide to be much more flood dominant, with the duration of falling tides lasting longer than rising tides.

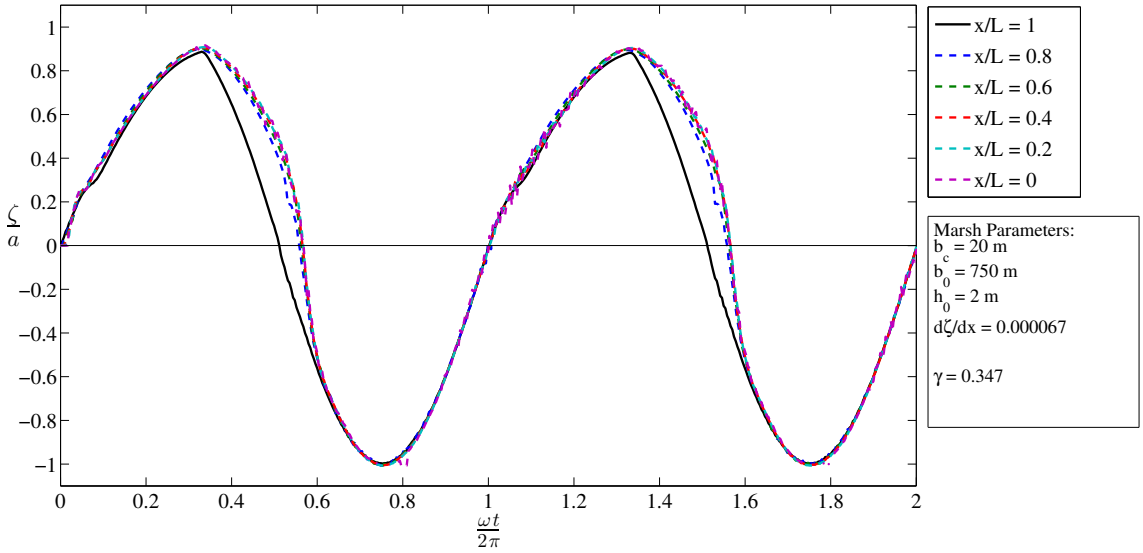

Figure 5.17: Surface elevations for simulation C1, with $n = 0.02$ and $||k_0||L = 1.562$. The channel mouth is defined to be located at $x = L$, based on the notation used by Friedrichs and Madsen (1992). The landward end is defined at $x = 0$.

As shown in Figure 5.19, case C1 undergoes an immediate increase in flood flux when water levels rise above 0 m. The shape of the discharge curve for C1 is similar to those of Type B flats. However, increasing friction by an order of magnitude appears to severely decrease the overall discharge, as well as the peak maximum and minimum values.

Unlike the results shown in Figure 5.16 and in the C1 curve in Figure 5.19, where the slope of the discharge curve experiences a sharp flattening when the tide reaches levels of the surrounding flats, the curve for C2 in Figure 5.19 continuously

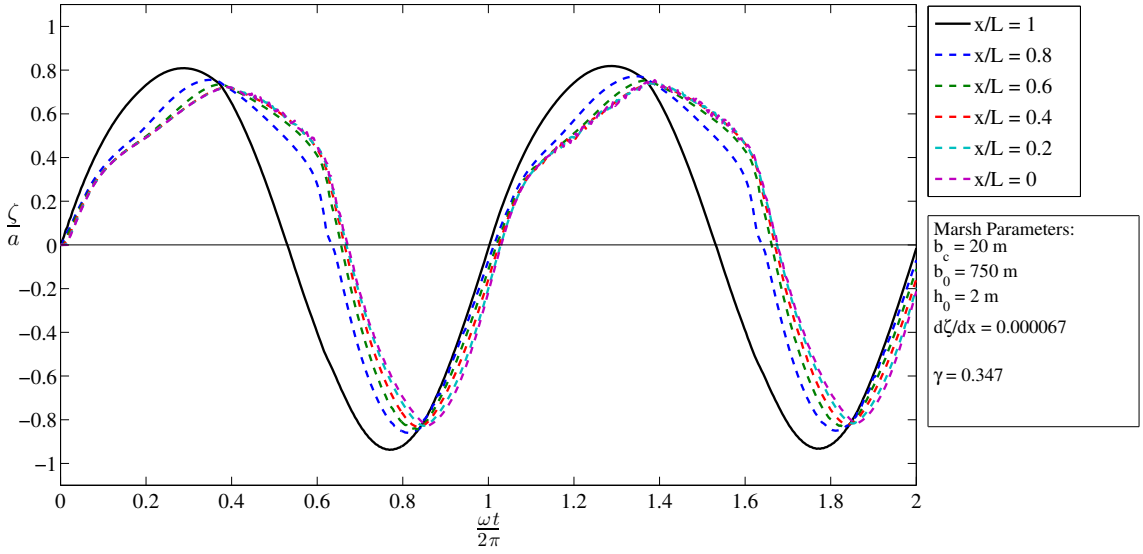

Figure 5.18: Surface elevations for simulation C2, with $n = 0.1$ and $||k_0||L = 3.492$. The channel mouth is defined to be located at $x = L$, based on the notation used by Friedrichs and Madsen (1992). The landward end is defined at $x = 0$.

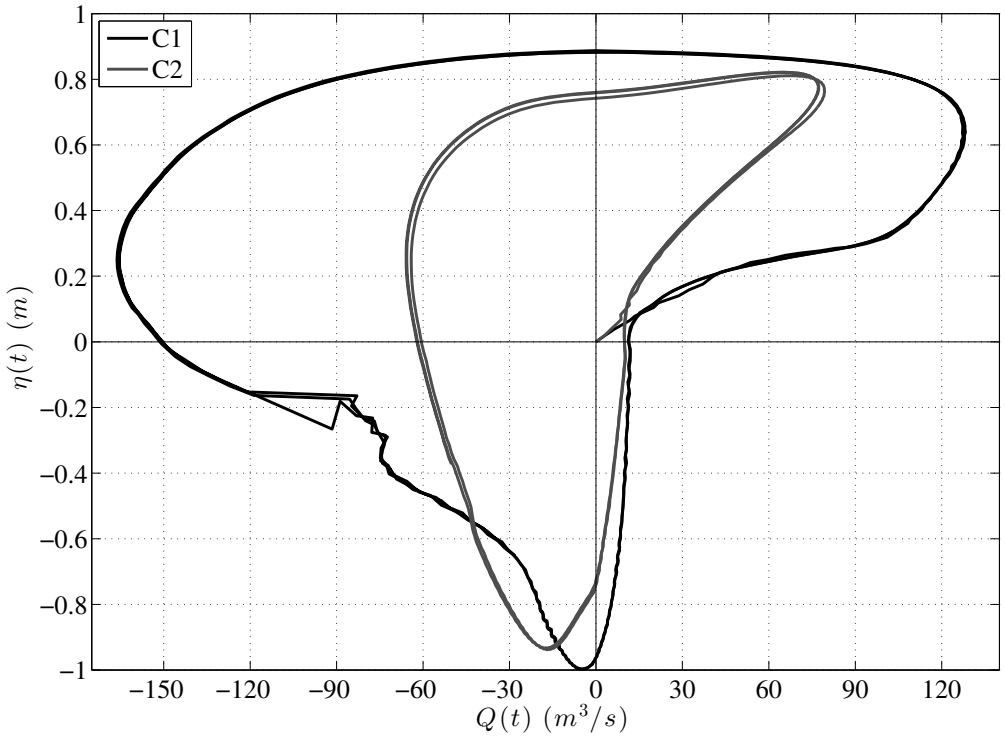

Figure 5.19: Stage-discharge curves for simulations C1 and C2.

increases when water levels reach the height of the flats. As will be shown in the next section, this behavior is more similar to that of a lower friction Type D marsh.

5.5.4 Type D Marshes

Brockonbridge Marsh exhibits marsh platforms which are best described by a Type D configuration. The idealized grid in Figure 5.6 was used in two simulations, D1 and D2, where the Manning coefficient in D2 was an order of magnitude larger than in D1.

For runs D1 and D2, the rate at which the tide rises drastically decreases when the water levels reach the elevation of the flat at the specific location of the gauge (Figures 5.20 and 5.21). This occurs in reverse order of the tidal propagation in the channel, spilling over first at the most landward gauge, which is the opposite of runs C1 and C2, which floods first at the mouth. The same trend is observed during the storm condition of Brockonbridge Gut (Figure 2.12b). There is strong flood dominance in both cases; although, as expected, run D2 shows a more pronounced flood dominance (Figure 5.21).

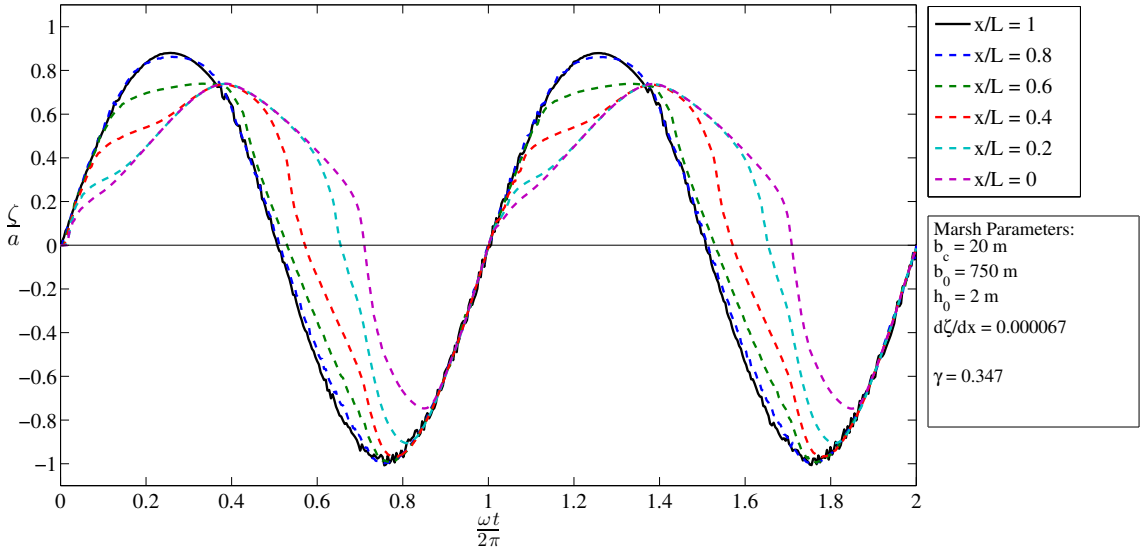

Figure 5.20: Surface elevations for simulation D1, with $n = 0.02$ and $||k_0||L = 1.562$. The channel mouth is defined to be located at $x = L$, based on the notation used by Friedrichs and Madsen (1992). The landward end is defined at $x = 0$.

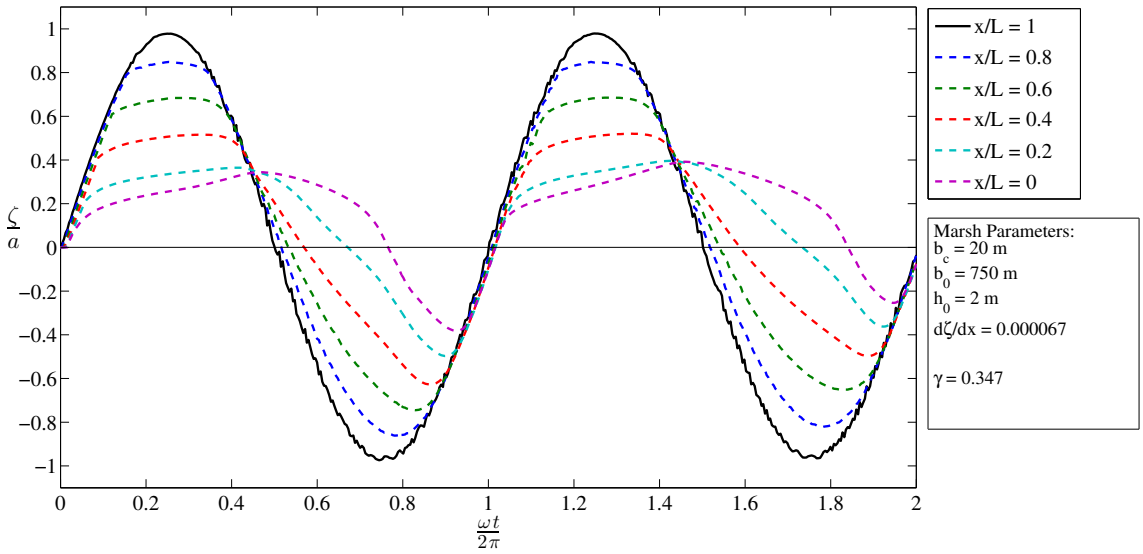

Figure 5.21: Surface elevations for simulation D2, with $n = 0.1$ and $||k_0||L = 3.492$. The channel mouth is defined to be located at $x = L$, based on the notation used by Friedrichs and Madsen (1992). The landward end is defined at $x = 0$.

The curve in Figure 5.22 for case D1 shows that the flats begin to flood right away. The elevation of the flat at the landward end is 0 m, so this makes sense, since the water levels begin at 0 m everywhere, and increase as specified by the boundary condition. In a much different way than the simulations shown in Figure 5.16 for Type B marshes, there is a more steady, constant increase in the flooding flux with rise in water levels. This is because, unlike Type B flats, which get inundated at nearly the same time everywhere, flats in Type D marshes are continuously flooded. In the case of D1 and D2, the flooding commences from the back of the domain and propagates forward. Then, during flow reversal, water in the channel begins to fall more quickly, which causes an ebbward pressure gradient, resulting in an enhanced ebb volume flux.

For run D2, Figure 5.22 shows the peak discharge and high/low tides are roughly 45° out of phase. So while the diffusive solution of Friedrichs and Madsen (1992) may not do well in explaining the propagation of tides through estuaries of Type D, it is successful is providing an explanation for the influence of friction in shifting the stage-discharge curve, as we expected based on the large $||k_0||L$ value for case D2.

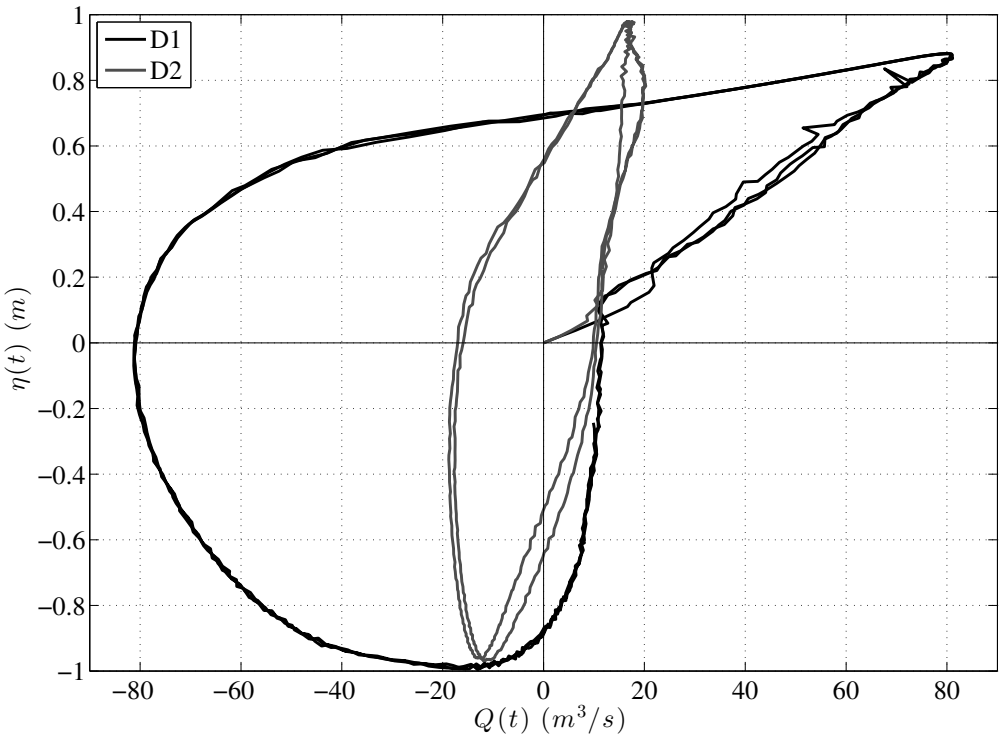

Figure 5.22: Stage-discharge curves for simulations D1 and D2.

5.5.5 Type D Marsh with Field Data as Boundary Condition

In an effort to see how well an idealized marsh with representative geometric values of Brockonbridge Marsh could explain the stage-discharge curve from Figure 2.17, a simulation was conducted using the measurements at the mouth of the Brockonbridge Gut (Site A in Figure 2.6) as a boundary condition. The results of run D-SiteA are presented in Figure 5.23, with colors corresponding to the same time spans in Figure 2.13.

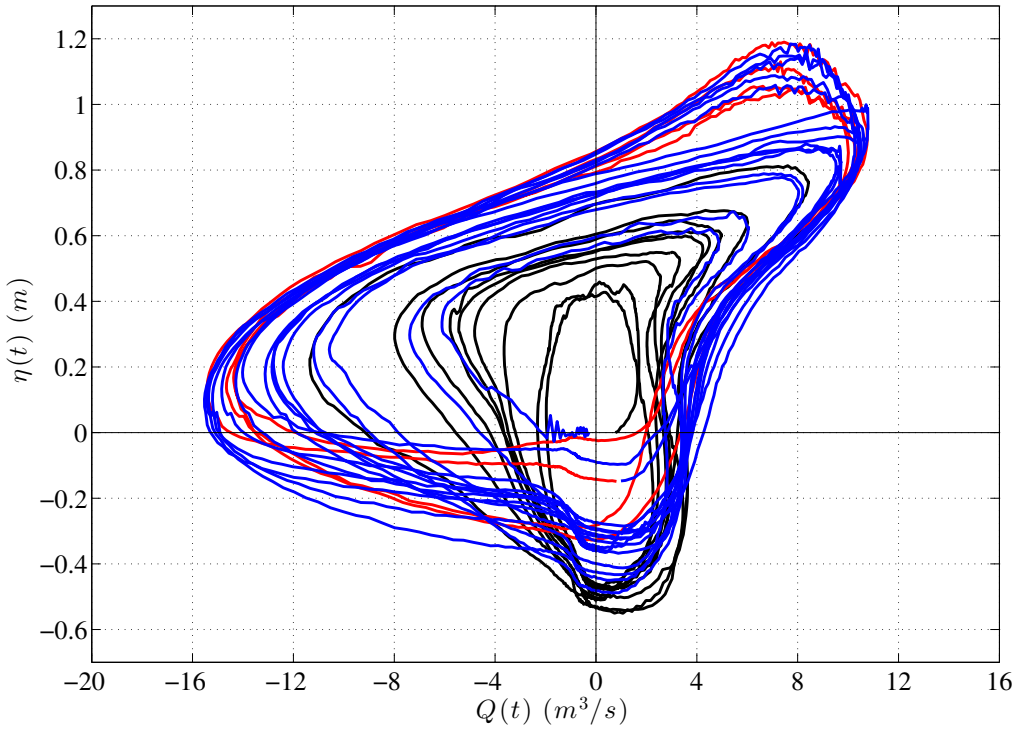

Figure 5.23: Stage-discharge curve for simulation D-SiteA, where $\eta(t)$ is the surface elevation recorded at Site A. The line colors correspond to the time spans shown in Figure 2.13: (black) before storm event, (red) during storm event, (blue) after storm event.

In a similar fashion to Figure 2.17, before the storm's arrival, the black line generally behaves like a standing wave in a channel. This is similar to the results just discussed and shown in Figure 5.12. As the storm starts to push water into the idealized marsh, a bulge develops in the upper right quadrant, which is also seen in the

field data. This bulge begins at around 0.4 meters, which is just above the elevation of the landward end of the flats, thus indicating the bulge is caused by water spilling onto the flats. Analogy can be drawn to case D1 (Figure 5.22) which demonstrates this same characteristic.

Furthermore, a similar slope to the field data is seen during the falling tide in Figure 2.17. The minimum water levels also correspond to the flow reversal from ebb to flood. The flood dominance is also present in the idealized case, which shows a sharp rise in water level without much distortion, until reaching the platform elevation.

The decrease in volumetric flux present after the water level rises above 1 m is likely caused by a drawback of this simplified marsh. While representative values for the platform elevations were taken directly from the Brockonbridge Marsh DEM, there is one feature that was not included in the idealized setup: the channel levees. It's probably that the explanation for the spike present at the top of the curve in Figure 5.23 is caused when the water levels on the platform rise high enough, and close enough to the mouth, to create a strong enough pressure gradient that can no longer be balanced by friction. Without levees to separate these regions, the incoming flux is damped by this gradient, even though the water level continues to rise for a bit longer.

5.6 Concluding Remarks

We can see by the lack of any major surges of flux in Figure 5.12, that for short estuaries, the presence of tidal flats serves as one of the major mechanisms in distorting the tidal discharge.

One parameter defined by Friedrichs and Madsen (1992) seems to do well in predicting flood dominance in the cases with marsh platforms whose slope is in the same direction as the channel, C1, C2, D1 and D2. In all of these cases, the asymmetry parameter, γ, is positive, indicating that the falling tide is longer in duration than rising tide, becoming more pronounced further into the domain.

With Type C and D marshes, we notice that the diffusive solution doesn't do well in explaining tidal propagation in marshes with flats whose slope varies in the

y-direction (compare the time series curves from Type C and D marshes with their diffusive solution analog, Figures 5.1 and 5.2, based on $||k_0||L$ values). Further evidence of this comes from showing that the separation of the curves is actually due almost entirely to the specific geometry of the marsh. This was shown by demonstrating that without the flats, there is virtually no separation in the curves during higher tides for Type A marshes, whereas the cases with tidal flats (Type B, C and D) all showed either pronounced separation in the tidal signals during high waters, or significant changes in the rate of water level increase.

When comparing the surface elevations throughout the main channel between cases C1 and D1 (Figures 5.17 and 5.20), we see that the overall average water depth is larger for C1. Water depth can be inferred from the surface elevation curves because the channel depths in cases C and D are the same throughout. Since celerity of shallow water waves is proportional to the square root of mean water depth, the max flux values for case C1 are consequently higher. The large ebb jet is potentially also caused partly by the presence of the sand dunes, serving as a constriction through which all of the outflowing water must flow, thus enhancing the velocities, similar to the venturi effect.

In either case, the maximum ebb discharge generally occurs when the water level drops below the lowest elevation of the marsh platforms, which is 0 m. This is also observed with the Type B flats in Figure 5.16.

Although cases C2 and D1 have completely opposite sloping flats, they appear to behave in a similar way (Figure 5.24). The only difference between the parameters in the two simulations is the magnitude of friction. In run C2, Manning's friction coefficient is nearly an order of magnitude higher than in case D1. Interestingly, when friction is increased this much for a Type C marsh, the stage-discharge relationship takes on the shape of the relationship found in Type D marshes with a more normal friction factor. The sole major difference is that the magnitude of the maximum ebb flow is slightly less and occurs slightly sooner for the case of C2. The smaller value of the magnitude can probably be explained simply by the fact that friction is an order of magnitude larger in case C2.

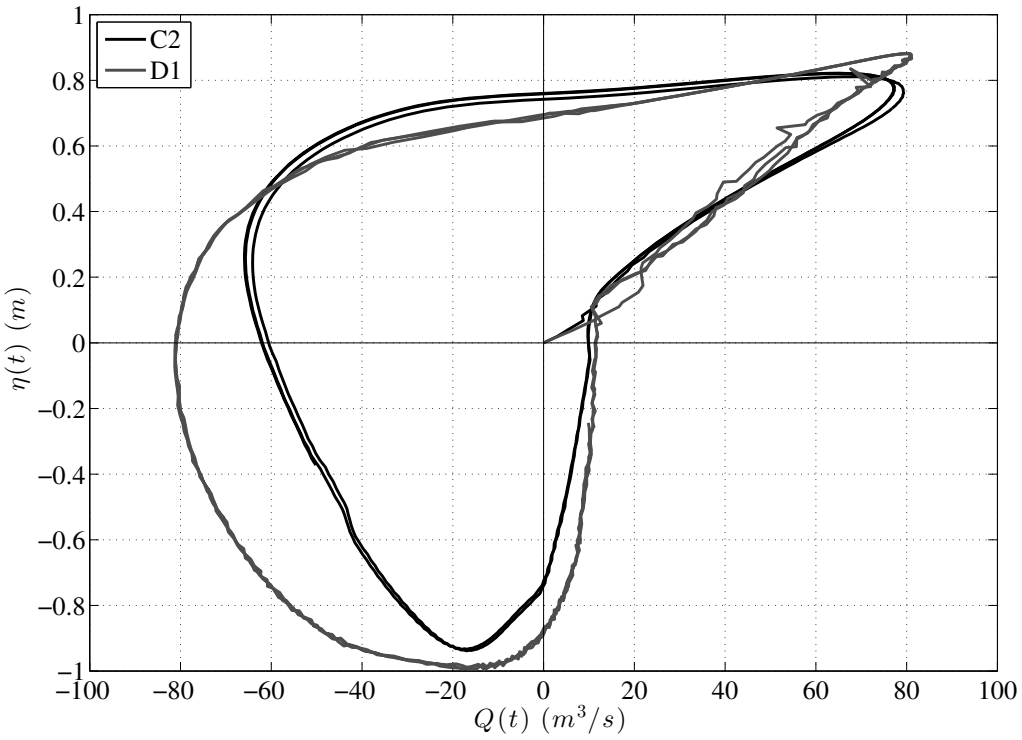

Figure 5.24: Stage-discharge curves for simulations C2 and D1.

Chapter 6

CONCLUSIONS AND FUTURE WORK

The coast of Delaware along Delaware Bay is comprised primarily of channelized tidal marshes, serving as both a refuge for wildlife and as protective barriers to inland areas during storms and imminent sea level rise.

The geometry of Brockonbridge Marsh is shown to be different than what is typically used to describe an idealized salt marsh. The marsh platform exhibits a slight, but noteworthy decrease in elevation with distance increasing from the inlet. The differences in elevation lead to differences in marsh grass species. *Spartina alterniflora* is found in the more landward areas of the marsh while *Spartina patens* tends to grow in the higher marsh near the bay. Furthermore, instead of being separated from open water by a steep scarp, Brockonbridge Marsh is separated from the bay by a sandy beach and sand dunes on either side of the inlet. Consequently, the inlet serves as the main conduit for flux into and out of the system.

Working in muddy salt marsh environments is often very difficult. However, due to the availability of access and relatively small area, extensive surveys of the main and several secondary channels were conducted. This led to a full topo-bathy, high-resolution DEM being generated, which was used in a numerical model of the marsh. The bathymetry of the Brockonbridge Gut exhibited a unique signature. The channel is relatively shallow near the mouth, before suddenly deepening to its deepest level at the first meander. The bed elevation then continually rises from this point, in the landward direction.

Pressure and velocity profiles were recorded over a 14-day period, spanning approximately 2.5 km of the Brockonbridge Gut. The field data show that during neap

phase, the tidal flats surrounding the channel are seldom inundated. Consequently, tidal distortion is very minimal, with durations of rising and falling tides almost equal. However, during deployment, towards the end of neap phase, a low-pressure system with strong winds directed onshore caused a multi-day surge event to occur across the marsh. The behavior of tidal propagation in the days following the storm becomes very distorted. The sudden surge of water causes the vegetated marsh platform to be inundated for a prolonged period. This results in the duration of falling tide to be considerably longer than for rising tide. After the storm, during spring phase, the marsh platform was regularly flooded during high tides. Although, the higher of the two daily high tides inundated a larger area of the tidal flats, resulting in a longer duration asymmetry between falling and rising tides.

Analysis of the pressure data show there is a maximum water level that can be reached, within reason (i.e. barring a surge event on the order of > 1 m above typical water levels), based on the elevation of the marsh platform in the immediate vicinity of a particular point in the main channel. The maximum attainable water level does not appear to be influenced by the surface elevation at the inlet; rather, the maximum is governed by the local geometry of the marsh. This is a direct consequence of the negatively sloping marsh platform.

It is typical in ocean and coastal modeling to create domains so that open boundary conditions may be applied far from the region of interest. However, this was not done in the modeling study presented in this manuscript for several reasons. First, due to the nature of this type of channelized marsh system, using a high-resolution grid is very important for modeling the hydrodynamics. The expanded domain used in Chapter 4.3 contained almost 3.5 million cells. With the open boundary far offshore and including Delaware Bay, as is done in many coastal studies of the region, maintaining the high-resolution grid spacing would require on the order of 1-2 billion grid cells. With the available computational resources, using a grid of that magnitude in size was not possible. Furthermore, expanding the domain beyond what was used in Chapter 4 would not have been sensible since the known boundary conditions were recorded

at the inlet of the marsh. Due to its proximity to the open boundary, this served to be a good forcing condition for the two domains used, as there was no lag time in propagation from the boundaries to the channel mouth.

The modeling work completed in this manuscript serves as a solid foundation for the continuation of numerical investigations of Brockonbridge Marsh in the future.

Several steps still remain in order to gain a better understanding into why the model results of NearCoM are under predicting the magnitudes of velocity during and after the storm. Further investigation into the residual currents and bottom stresses across the domain will likely provide more insight. This analysis will highlight circulation patterns which could lead to the answer for why the model computes the water to remain in the system for an extended period of time.

Additionally, momentum balances should be conducted across several transects of the domain to better understand the relative magnitudes between each term before, during and right after inundation of the tidal flats.

The larger DEM that was created from merging three different datasets together needs to be examined more closely. Specifically, a more detailed analysis needs to be done on the connectivity of the smaller "mosquito ditches."

Through idealized studies, the friction factor appears to play a key role in governing the distortion of the tide as it propagates into the marsh domain. Therefore, the effects of variable friction factors assigned to different areas of the domain should be explored.

Finally, the amount of water that remains ponded on the surface of the marsh platform as the tide recedes needs a closer look. This does not occur in the field, based on observations made during the two week stay at the marsh. Some of the issues are likely in the explicit wet/dry scheme. Better wet/dry schemes are available, but they are much more computationally intensive.

Once the model is adequately validated, more comprehensive studies on the domain can be done. For example, the sensitivity of water levels in landward areas of the marsh to the forcing condition at the mouth can be further explored. Also, the

influence of the magnitude, direction and duration of wind events can be modeled.

REFERENCES

Barbour, M. G. (1978), The effect of competition and salinity on the growth of a salt marsh plant species. *Oecologia*, **37**, 93-99.

Boon, J. D. (1975), Tidal discharge asymmetry in a salt marsh drainage system. *Limnology and Oceanography*, **20(1)**, 71-80.

Boon, J. D., Boule M. E., and Silberhorn, G. M. (1977), "Delineation of tidal wetlands boundaries in lower Chesapeake Bay and its tributaries." Special Rep. No. 140, Applied Marine Science and Ocean Engineering, Virginia Institute of Marine Science, Gloucester Point, Virginia, 127 p.

Boon, J. D. and Byrne, R. J. (1981), On basin hypsometry and the morphodynamic response of coastal inlet systems. *Mar. Geol.*, **40**, 27-48.

Blanton, J. O., Lin, G., and Elston, S. A. (2002), Tidal current asymmetry in shallow estuaries and tidal creeks. *Cont. Shelf Res.*, **22**, 1731-1743.

Cahoon, D. R., and Reed, D. J. (1995), Relationships among marsh surface topography, hydroperiod, and soil accretion in a deteriorating Louisiana salt marsh, *J. Coastal Res.*, **11**, 357-369.

Chen, J., Shi, F., Hsu, T. and Kirby, J. T. (2014), NEARCOM-TVD - A quasi-3D nearshore circulation and sediment transport model. *Coastal Engineering*, in review.

Church, J. A., Gregory, M., Huybrechts, P., Kuhn, M., Lambeck, K., Nhuan, M. T., Qin, D., and Woodworth, P. L. (2001), Changes in sea level, in *Climate Change 2001: The Scientific Basis. Contribution of Working Group I to the Third Assessment Report of the Intergovernmental Panel on Climate Change*, edited by J. T. Houghton, Y. Ding, D. J. Griggs, M. Noguer, P. J. van der Linden, X. Dai, K. Maskell, and C. A. Johnston, pp. 639-693, Cambridge University Press, Cambridge, UK.

Church, J. A. and White, N. J. (2006), A 20th century acceleration in global sea-level rise. *Geophys. Res. Lett.*, **33**, L01602.

Church, J. C. and Thornton, E. B. (1993), Effects of breaking wave induced turbulence within a longshore current model. *Coastal Eng.*, **20**, 1-28.

Craft, C., Clough, J., Ehman, S., Joye, S., Park, D., Pennings, S., Guo, H. and Machmuller, M. (2009), Forecasting the effects of accelerated sea level rise on tidal marsh ecosystem services. *Frontiers Ecol. Environ.*, **7**, 73-78.

D'Alpaos, A., Lanzoni, S., Rinaldo, A., and Marani, M. (2009), Intertidal eco-geomorphological dynamics and hydrodynamic circulation, in *Coastal Wetlands: An Integrated Ecosystem Approach*, edited by G. M. E. Perillo et al., pp. 159-179, Elsevier, Amsterdam.

Dronkers, J. (1986), Tidal asymmetry and estuarine morphology. *Netherlands Journal of Sea Research*, **20**, 117-131.

Fagherazzi, S., Kirwan, M. L., Mudd, S. M., Guntenspergen, G. R., Temmerman, S., D'Alpaos, A., van de Koppel, J., Rybczyk, J. M., Reyes, E., Craft, C. and Clough, J. (2012), Numerical models of salt marsh evolution: Ecological, geomorphic and climatic factors. *Rev. Geophys.*, **50**, RG1002.

Friedrichs, C. T. (2010), Barotropic Tides in Channelized Estuaries. In: A. Valle-Levinson (ed.), *Contemporary Issues in Estuarine Physics.* Cambridge University Press, Cambridge, UK, pp. 27-61.

Friedrichs, C. T. and Madsen, O. S. (1992), Nonlinear diffusion of the tidal signal in frictionally dominated embayments. *J. Geophys. Res.*, **97**, 5637-5650.

Greene, R. W. and Miller, R. W. (1994), *Summary and assessment of Polychlorinated Biphenyls and selected pesticides in Striped Bass from the Delaware Estuary.* Delaware Department of Natural Resources & Environmental Control, Dover, Delaware.

Haas, K. A., Svendsen, I. A., Haller, M. C. and Zhao, Q. (2003), Quasi-three-dimensional modeling of rip current systems. *J. Geophys. Res.*, **108**, C7, 3216.

Jonsson, I. G. (1966), Wave boundary layers and friction factors. *Proc. 10th Int. Conf. Coastal Engrg.*, ASCE, 127-148.

Kirwan, M. L. and Guntenspergen, G. R. (2010), The influence of tidal range on the stability of coastal marshland. *J. Geophys. Res.*, **115**, F02009.

Kirwan, M. L. and Temmerman, S. (2009), Coastal marsh response to historical and future sea-level acceleration. *Quat. Sci. Rev.*, **28**, 1801-1808.

Kjerfve, B., Miranda, L. B., and Wolanski, E. (1991), Modelling water circulation in an estuary and intertidal salt marsh system. *Netherlands Journal of Sea Res.*, **28(3)**, 141-147.

LeBlond, P. H. (1978), On tidal propagation in shallow rivers. *J. Geophys. Res.*, **83**, (C9), 4717-4721.

Longuet-Higgins, M. S. and Stewart, R. W. (1962), Radiation stress and mass transport in gravity waves, with application to surf beats. *J. of Fluid Mech.*, **8**, 565-583.

Longuet-Higgins, M. S. and Stewart, R. W. (1964), Radiation stresses in water waves, a physical discussion, with applications. *Deep Sea Research*, **11**, 529-563.

Manning R. (1891), On the flow of water in open channels and pipes. *Transactions of the Institution of Civil Engineers of Ireland*, **20**, 161-207.

Marani, M., D'Alpaos, A., Lanzoni, S. and Santalucia, M. (2011), Understanding and predicting wave erosion of marsh edges. *Geophys. Res. Lett.*, **38**, L21401.

March, R. C. and Smith, E. H. (2012), Modeling potential coastal vegetation response to sea level rise and storm surge on estuarine peninsulas. *J. of Coastal Res.*, **28(5)**, 993-1007.

Mariotti, G. and Fagherazzi, S. (2012), Channels-tidal flat sediment exchange: The channel spillover mechanism. *J. of Geophys. Res.*, **117**, C03032.

Mariotti, G. and Fagherazzi, S. (2010), A numerical model for the coupled long-term evolution of salt marshes and tidal flats. *J. Geophys. Res.*, **115**, F01004.

McKee, K. L and Patrick, W. H. Jr (1988), The relationship of smooth cordgrass (*Spartina alterniflora*) to tidal datums: A review. *Estuaries*, **11(3)**, 143-151.

McKenna, T. E. (2013), Characterization of tidal wetland inundation in the Murderkill River Estuary, report submitted to Kent County Levy Court, 61 p.

Mieras, R. and Kirby, J. T. (2014), "Discharge, pressure and bathymetry measurements in Brockonbridge Gut, Kent County, Delaware: Data report." Research Report CACR-14-05. Center for Applied Coastal Research, University of Delaware.

Mieras, R., Kirby, J. T. and Shi, F. (2014), "A high-resolution numerical model investigation into the response of a channelized salt marsh to a storm surge event" Research Report CACR-14-07. Center for Applied Coastal Research, University of Delaware.

Morris, J. T., Sundareshwar, P. V., Nietch, C. T., Kjerfve, B., and Cahoon, D. R. (2002), Responses of coastal wetlands to rising sea level, *Ecology*, **83(10)**, 2869-2877.

Mudd, S. M. Howell, S. M, and Morris, J. T. (2009), Impact of dynamic feedbacks between sedimentation, sea-level rise, and biomass production on near surface marsh stratigraphy and carbon accumulation, *Estuarine Coastal Shelf Sci.*, **82(2)**, 377-389.

Nardi, M. (2009), *Digital Elevation Model for the Murderkill River Estuary based on LiDAR survey in January and February 2008*, contract deliverable to Delaware Geological Survey.

Pethick, J. S. (1980), Velocity surges and asymmetry in tidal channels. *Est. Coast. Mar. Sci.*, **11**, 331-345.

Pingree, R. D. and Maddock, L. (1978), The M_4 tide in the English Channel derived from a non-linear numerical model of the M_2 tide. *Deep Sea Res.*, **25**, 53-68.

Putrevu, U. and Svendsen, I. A. (1999), Three-dimensional dispersion of momentum in wave-induced nearshore currents. *Eur. J. Mech. B/Fluids*, 83-101.

Rinaldo, A., Fagherazzi, S., Lanzoni, S., Marani, M. and Dietrich, W. E. (1999), Tidal networks: 2. Watershed delineation and comparative network morphology, *Water Resour. Res.*, **35(12)**, 3905-3917.

Sanborn (2008), *State of Delaware LiDAR Campaign Final Report For New Castle & Kent Counties February 2008*, 1935 Jamboree Dr., Suite 100, Colorado Springs, CO.

Shi, F., Kirby, J. T., Hsu, T. J., Chen, J. and Mieras, R. (2013), "A Hybrid TVD Sover for Nearshore Community Model Documentation and User's Manual," Center for Applied Coastal Research Report, CACR 2013-06, University of Delaware.

Shi, F., Hanes, D. M., Kirby, J. T., Erikson, L., Barnard, P. and Eshleman, J. (2011), Pressure gradient driven nearshore circulation on a beach influenced by a large inlet-tidal shoal system. *J. Geophys. Res.*, **116**, C04020.

Shi, F., Kirby, J. T. and Hanes, D. (2007), An efficient mode-splitting method for a curvilinear nearshore circulation model. *Coastal Engineering*, **54**, 811-824.

Shi, F., Svendsen, I. A., Kirby, J. T. and Smith, J. M. (2003), A curvilinear version of a quasi-3D nearshore circulation model. *Coastal Engineering*, **49**, 99-124.

Shi, F. and Sun, W. (1995), A variable boundary model of storm surge flooding in generalized curvilinear grids. *International Journal for Numerical Methods in Fluids*, 21 (8), 642-651.

Soulsby, R. L., Hamm, L., Klopman, G., Myrhaug, D., Simons, R. R. and Thomas, G. P. (1993), Wave-current interaction within and outside the bottom boundary layer. *Coastal Eng.*, **21**, 41-69.

Soulsby, R. L. (1997), *Dynamics of Marine Sands*. Thomas Telford, London.

Svendsen, I. A., Haas, K. A. and Zhao, Q. (2004), "Quasi-3D Nearshore Circulation Model SHORE-CIRC: Version 2.0." Research Report, Center for Applied Coastal Research, University of Delaware.

Svendsen, I. A. and Putrevu, U. (1990), Nearshore circulation with 3-D profiles. *Proc 22nd Int. Conf. Coastal Engrg.*, ASCE, 241-254.

Speer, P. E. and Aubrey, D. G. (1985), A study of non-linear tidal propagation in shallow inlet/estuarine systems part II: Theory. *Estuarine, Coastal and Shelf Science*, **21**, 207-224.

Stoddart, D. R., Reed, D. J., and French, J. R. (1989),Understanding salt marsh acretion, Scolt Head Island, Norfolk, England. *Estuaries*, **12(4)**, 228-236.

Temmerman, S., Bouma, T. J., Govers, G., Wang, Z. B., De Vries, M. B., and Herman, P. M. J. (2005), Impact of vegetation on flow routing and sedimentation patterns: Three-dimensional modeling for a tidal marsh. *J. Geophys. Res.*, **110**, F04019.

Temmerman, S., Govers, G., Meire, Px, and Wartel, S. (2003), Modelling long-term tidal marsh growth under changing tidal conditions and suspended sediment concentrations, Scheldt Estuary, Belgium. *Mar. Geol.*, **193**, 151-169.

Titus, J. G., Jones, R. and Streeter, R. (2008), *Maps that depict site-specific scenarios for wetland accretion as sea level rises along the Mid-Atlantic coast. Section 2.2 in: Background Documents Supporting Climate Change Science Program Synthesis and Assessment Product 4.1.* J.G. Titus and E.M. Strange (eds.), EPA 430R07004. U.S. EPA, Washington, DC.

Thacker, W. C. (1981), Some exact solutions to the nonlinear shallow-water wave equations. *J. Fluid Mech.*, **107**, 499-508.

Thompson, J. F., Warsi, Z. U. and Mastin, C. W. (1985), *Numerical grid generation: foundations and applications.* Elsevier North-Holland, Inc., New York, NY, USA.

Toro, E. F. (2009), *Riemann Solvers and Numerical Methods for Fluid Dynamics: a Practical Introduction.* Third edition, Springer, New York.

van der Wegen, M. (2010), *Modeling Morphodynamic Evolution in Alluvial Estuaries.* CRC Press/Balkema, Leiden, the Netherlands, 187 pp.

Velinsky, D., Charles, D., Sommerfield, C., Greene, R., and Fikslin, T. (2011), *Tidal marshes in the Delaware Estuary: Historical reconstruction of chemical loadings.* Delaware Estuary Science & Environmental Summit, Cape May, New Jersey.

Volp, N. D., van Prooijen, B. C. and Stelling, G. S. (2013), A finite volume approach for shallow water flow accounting for high-resolution bathymetry and roughness data. *Water Resour. Res.*, **49**, 4126-4135.

WAMDI Group (1988), The WAM model: A third generation ocean wave prediction model. *J. of Physical Oceanography*, **18**, 1775-1810.

Wilmott, C. J. (1981), On the validation of models. *Phys. Geogr.*, **2**, 184-194.

Appendix

MODEL COMPARISONS WITH EXACT SOLUTIONS TO THE NONLINEAR SHALLOW WATER WAVE EQUATIONS

Prior to this report, the numerical schemes used in SHORECIRC had not yet been fully tested in regimes containing sharp gradients in topography at such a high resolution. The following discusses the process and results of comparing analytically obtained exact solutions to the nonlinear shallow water (NLSW) equations for elliptical basins (Thacker, 1981) with modeled results from NearCoM, using a finely spaced grid. Good agreement is found between the numerical and analytical solutions.

The particular case from Thacker (1981) that was used for comparisons is for oscillations in which the surface remains planar as it sloshes around an enclosed basin. The solution assumes the domain is described by an elliptical paraboloid,

$$D = D_0 \left(1 - \frac{x^2}{L_1^2} - \frac{y^2}{L_2^2}\right) \tag{A.1}$$

where L_1 and L_2 define the lengths of the major and minor axes, respectively, D_0 is the vertical length scale and D is the elevation of the grid surface, where positive values are *below* equilibrium level.

The test case that was considered assumed that $L_2 >> L_1$ such that the bed is essentially an elliptically shaped canal. With this assumption, and neglecting the Coriolis effect, Thacker (1981) shows the solution for surface elevation reduces to

$$\eta = \frac{2aD_0}{L_1} cos(\omega t) \left(\frac{x}{L_1} - \frac{a}{2L_1} cos(\omega t)\right) \tag{A.2}$$

$$\omega = \left(\frac{2gD_0}{L_1^2}\right)^{\frac{1}{2}} \tag{A.3}$$

where a is a constant, and g is the gravitational constant of acceleration. For the simulations, D_0 was taken to be 1 m.

To create the grid for the test case, values for L_1 and L_2 were taken to be 1 km and 1,000 km, respectively. By utilizing the relationship of $L_2 >> L_1$, the simulation can be reduced to a 2-D problem, as the variations in the y-direction become negligible. The value of 1 km for L_1 was chosen to represent the similar length scale of oscillation in Brockonbridge Marsh. Furthermore, the grid spacing in the x-direction was taken to be 2 meters, again, in order to represent the DEM grid spacing of Brockonbridge Marsh used in the modeling study.

Finally, the value for a was chosen to be 40 m. Note that the value of a is not the scale for the amplitude of oscillation. Rather, from (A.2), it can be seen that the scale for the amplitude of oscillation is also a function of the horizontal length scale of the oscillatory flow and the vertical length scale, from $\frac{2aD_0}{L_1}$. Therefore, the value of 40 m for a forces the variation in surface slope in the exact solution to scale well with the surface gradient observed in the Brockonbridge Gut.

The initial condition was simply set to be $\eta(t = 0)$ in (A.2), with all initial velocities set to zero (Figure A.1a). Since the governing equations used to derive the analytical solution for η in Thacker (1981) neglected any friction terms, the friction was turned off in the NearCoM simulations as well.

In order to quantify the accuracy of the model computations in comparison with the exact solution, a skill value was computed following the formulation of Wilmott (1981),

$$Skill = 1 - \frac{\Sigma_{n=1}^{N} |\eta_{mod} - \eta_{exact}|^2}{\Sigma_{n=1}^{N} \left[|\eta_{mod} - \overline{\eta}_{exact}| + |\eta_{exact} - \overline{\eta}_{exact}| \right]^2} \tag{A.4}$$

where η_{exact} is defined in (A.2), η_{mod} is the surface elevation computed by the model, and the overbar, $\overline{()}$, represents the sample mean. A skill value of 1 denotes perfect agreement between the model and exact solution. In this case, a single skill value was obtained by the summation over the entire spatial and temporal domains. In doing so, a skill value of 0.9999 was computed over two periods of oscillation.

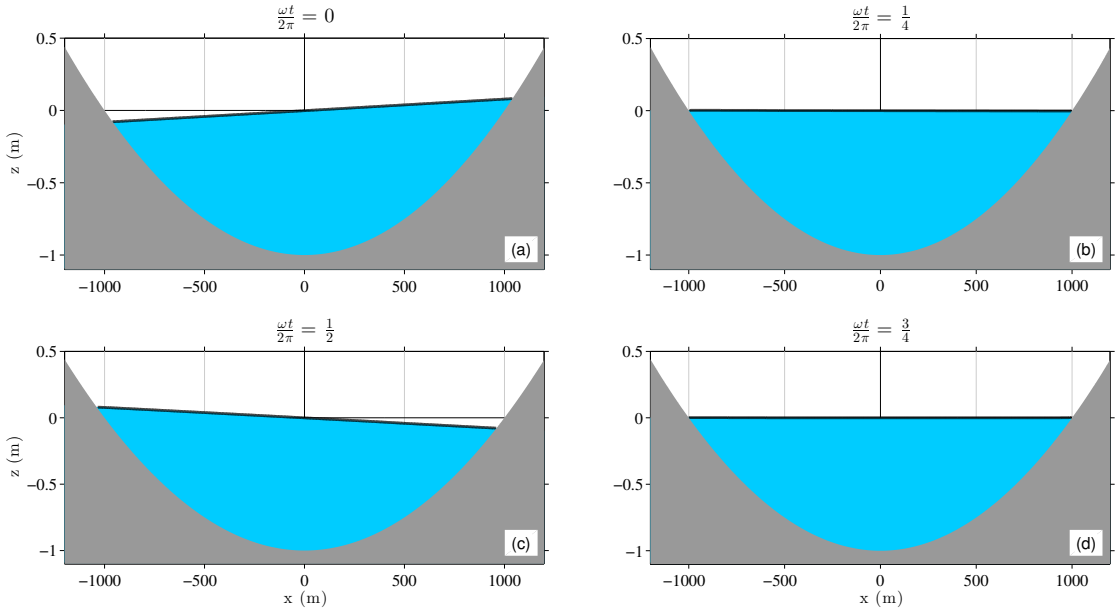

Figure A.1: Comparison between model results from NearCoM and the exact solution from Thacker (1981). The bathymetry is shown in grey, the analytical solution for time, t, is shown in blue, and the numerical model computation is represented by the thick black line. (a) gives the initial configuration; (b) - (d) show the system at $\frac{1}{4}$, $\frac{1}{2}$, and $\frac{3}{4}$ the period of oscillation, respectively. Note that each plot is not to scale. The ratio of the vertical to horizontal length scale, $\frac{D_0}{L_1}$, is $O(10^{-3})$.

The good agreement between the model results and the exact solution seen in Figure (A.1), and quantitatively from a skill value of 0.9999, demonstrates NearCoM's capability in handling slowly-varying, oscillatory flows in shallow water regimes with small grid spacing relative to the length scale of oscillation, namely $\frac{\Delta x}{L_1} << 1$. More specifically, it has been demonstrated that the numerics of NearCoM can handle length and time scales representative of Brockonbridge Marsh.